Open-source hardware platform for Earth's field NMR

van der Veeken, Teun S.W.

Award date:
2017

Technische Universiteit Eindhoven University of Technology
Department of Applied Physics
Transport in Porous Media Research Group

Open-source Hardware Platform for Earth's Field NMR

Master Thesis

Teun van der Veeken BSc.

Supervisor:
Dr.Ir. Leo Pel

Committee members:
Dr.Ir. Leo Pel
Dr.Ir. Henk Huinink
Prof.Dr.Ir. Klaas Kopinga
Dr.Ir. Peter Mutsaers
Prof.Dr.Ir. Willem van de Water

Final Version

Eindhoven, November 2017

Abstract

Nuclear Magnetic resonance (NMR) is often used in research and a well-known medical application is Magnetic Resonant Imaging (MRI). Signal-to-Noise Ratio (SNR) of an NMR signal is proportional to $B^{7/4}$, where B is the magnetic field strength. As a result of the demand for ever increasing SNR in NMR experiments, this has led to an increase in cost and technical complexity of NMR setups, making them unavailable for educational purposes. This gap can be filled by designing a low cost, open-source platform capable of measuring the same quantities as a more expensive typical application setup using earths magnetic field.

In Earth's Field Nuclear Magnetic Resonance (EFNMR), earth's magnetic field is used as static magnetic field required to perform NMR. This drops the requirement of producing a static magnetic field and greatly reduces setup cost and complexity. The SNR can be greatly increased by making use of a pre-polarization field and hence standard NMR experiments can be performed using earth's magnetic field. By applying various additional noise reduction techniques a setup can be designed which can be used indoors in electrically noisy environments.

An EFNMR setup has been designed and constructed which has been shown to be capable of measuring several NMR material properties, accurate within measurement tolerances to literature values. It is shown that the present setup can be used in both adiabatic and non-adiabatic NMR, hence greatly increasing the possibilities of the setup. Total cost of the setup achieved is below €500, affordable for teaching institutions.

Introduction

Nuclear Magnetic resonance (NMR) is a quantum mechanical phenomenon that originates from the spin of nuclear particles, present in all atoms. The most NMR sensitive element, is ^1H, hydrogen. Since hydrogen is one of the two main atoms inside water, NMR can be used to measure moisture distributions in materials. In hospitals, NMR is commonly used to measure position dependent moisture content in the human body using Magnetic Resonant Imaging (MRI). Due to slight differences in chemical environment of hydrogen atoms in different chemicals, NMR can be used as spectroscopic method to identify chemicals. Together with MRI, NMR is a commonly used tool both in medical and research applications, where many varieties exist.

NMR experiments require a static magnetic field to function and typical field strengths range from $0.5T$ to $23.5T$ [18]. Since Signal-to-Noise Ratio (SNR) of an NMR experiment scales with the power $7/4$ to the magnetic field strength used [23], higher field strength gives better SNR. However, obtaining a magnetic field of ample homogeneity across a sufficient measurement volume requires expensive and complex equipment. Besides technical complexity and high initial purchasing cost of such a setup, also operating cost make them available only in research facilities and medical institutions.

These two observations are in contradiction with each other. There is a big demand for this research tool, but their increasing complexity and cost make them unavailable for the wide public, especially students. As an alternative to setups using high strength magnetic fields, also earth's magnetic field can be used. Using this magnetic field which is present everywhere, means that technical complexity and purchasing cost of a setup can be greatly reduced. This makes it possible to construct low cost setups that can be used by students, such that they can become familiar with the concepts of NMR.

Unfortunately, earth's magnetic field strength is low, on the order of magnitude of $40\mu T$ [17]. Therefore, SNR of an Earth's Field Nuclear Magnetic Resonance (EFNMR) measurement is significantly lower compared to high field strength NMR. To be able to perform an EFNMR experiment with sufficient SNR, several challenges have to be overcome. Fortunately, these same challenges also provide the unique opportunity to use off the shelf electronics and hardware. This hardware can be produced for a fraction of the price of a high field NMR setup, making EFNMR attractive for a much wider user base.

Applications of an EFNMR setup are various, and several applications exist which are not possible with traditional NMR. Since EFNMR uses the earth's magnetic field, it can be used to precisely monitor absolute field strength. Solar activity for instance influences earth's magnetic field strength and we can thus monitor this using EFNMR. Moreover, since ferromagnetic materials bend magnetic field lines, EFNMR can also be used for geomagnetic surveying. More typical NMR experiments such as measuring moisture distributions can also be performed using EFNMR albeit with lower resolution due to higher sample volumes required to obtain adequate SNR. In the work that this report represents, an open-source

hardware platform capable of performing such a multitude of EFNMR experiments has been developed, tested and verified.

This report is built up in several sections. First, a project goal is given which includes criteria the setup should meet. The body of this report is set up to describe an EFNMR setup from the sample where NMR starts, towards the final signal and data processing. Schematically, a setup of an EFNMR setup is shown in figure 1. Chapter 1 is dedicated

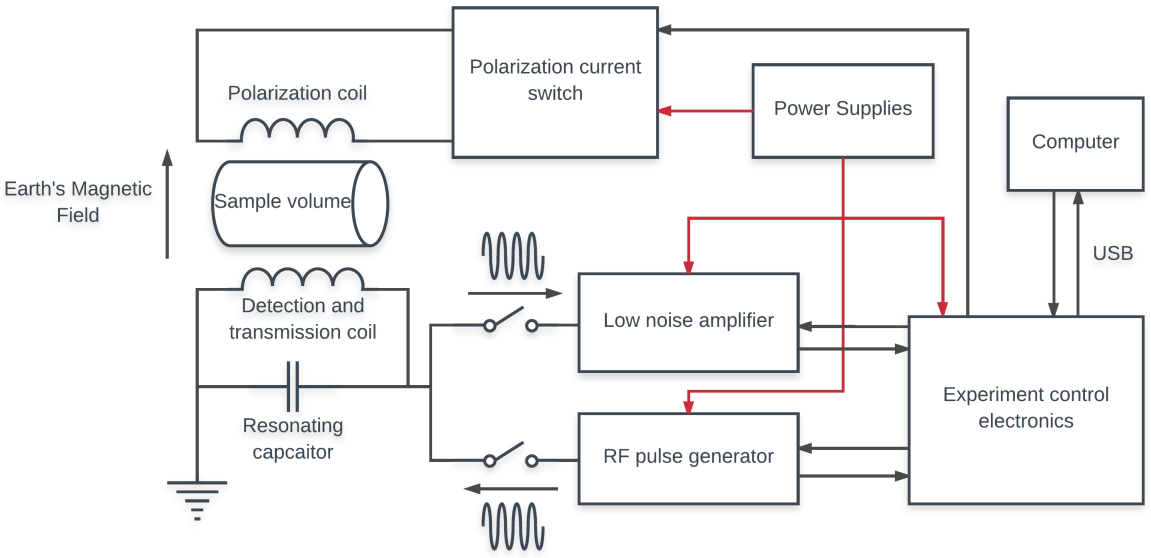

Figure 1: Schematic overview of a general EFNMR setup.

to the theory of NMR. This chapter describes what happens in the sample, which is the first part of our setup. Up unto this point, no separation between NMR and EFNMR is made. In chapter 2 however the differences between NMR and EFNMR will be highlighted. In this chapter, we will also show the requirement of adding a polarization coil around the sample and analyze the properties of this coil. In addition, the polarization current switch will be designed. In chapter 3 we will take the description of the setup one step further by analyzing the detection coil. In this chapter, we will look at SNR and inspect methods of increasing it by making the detection coil resonant and by using a secondary coil to reduce noise. In the fourth chapter, all final specifications of the polarization and detection coils will be given. At the start of chapter 5, the sample, polarization and detection coils have been specified. We now have to amplify, filter and digitize the measurement signal coming from the sample. In this chapter, these topics are covered again starting at the first amplification stage and finishing at the Analog-to-Digital Converter (ADC). Also, we explain how pulses are generated and how the entire experiment is controlled using a Teensy, the heart of the experiment control electronics.

After all hardware has been described, we explain how a Graphical User Interface (GUI) is used to interface the experiment to the user in chapter 6. In chapter 7, multiple measurement results of experiments performed using the setup are included to illustrate the capabilities of the setup. Finally, a conclusion and evaluation of the design goals is given as well as a detailed discussion and outlook of possible further improvements.

In the appendices, development of the hardware as well as some of the essential parts of the programming used are documented.

Goal

The goal of this project is to develop an open-source hardware platform capable of performing all types of EFNMR experiments a user would typically require to make meaningful measurements of desired quantities, at a cost price of maximum €500.

The device should exploit all the benefits a low field NMR measurement provides over a traditional high intensity field NMR. The hardware required in the setup should be based mainly upon a fixed but flexible hardware platform with user configurable measurement setups. To allow expansion of the platform for future developments, the platform should offer options concerning interfacing, to expand the currently developed hardware.

Implementation of the controls of the device should be open-source for anybody to modify and improve. Therefore, the design should be easily upgradeable with minimum understanding of electronics or programming. This should be done in a common user friendly way and preferably in a well-documented fashion.

Moreover, the hardware platform should be easy to use for anybody who is not familiar with EFNMR or even normal NMR for that matter. With minimum effort, it should be possible to get meaningful data from the device for any use case. Fundamental understanding of quantum physical phenomena as well as electronics and signal processing should be made insightful by varying process parameters during the experiments as well as exploring the design documents this work describes.

More specific, the device should be capable of performing the following measurements.

- Measure Free Induction Decay (FID) to monitor the earth's magnetic field strength as function of place and time.
- Perform spin echo and Carl Purcell Meyboom Gill (CPMG) measurements to measure material properties such as $T1$ and $T2$.

Within these experiments, the device should automatically suggest the optimal settings to the user such that results can be obtained quickly and reliably. Data analysis should also be performed automatically within limits of each of the experiments performed. The data should be exportable in standard formats and easy to visualize.

Abbreviations

Abbreviation	Meaning	First use on page
AC	Alternating Current	32
ADC	Analog-to-Digital Converter	12
CPMG	Carl Purcell Meyboom Gill	10
CSA	Cross Sectional Area	7
DAC	Digital-to-Analog Converter	51
DC	Direct Current	21
DDS	Direct Digital Synthesis	51
DFT	Discrete Fourier Transform	78
DMA	Direct Memory Access	52
EFNMR	Earth's Field Nuclear Magnetic Resonance	1
EMF	Electro Motive Force	6
FFT	Fast Fourier Transform	45
FID	Free Induction Decay	9
FWHM	Full Width at Half Maximum	59
GUI	Graphical User Interface	54
HEXFET	Hexagonal Field Effect Transistor	40
HWHM	Half Width at Half Maximum	81
IC	Integrated Circuit	50
IDE	Integrated Development Environment	47
LSB	Least Significant Bit	85
MCU	Micro Controller Unit	51
MOSFET	Metal Oxide Semiconductor Field Effect Transistor	16
MRI	Magnetic Resonant Imaging	14
NMR	Nuclear Magnetic resonance	1
PC	Personal Computer	85

Abbreviation	Meaning	First use on page
PCB	Printed Circuit Board	40
PGA	Programmable Gain Amplifier	50
PPM	Proton Precession Magnetometer	15
RAM	Random Access Memory	51
RF	Radio Frequency	4
RLC	Resistive inductive (L) Capacitive circuit	24
RMS	Root Mean Square	44
SNR	Signal-to-Noise Ratio	7
SPI	Serial Peripheral Interface	49
USB	Universal Serial Bus	48

List of Symbols

Symbol	Name	Units	First use on page
$\vec{B}_0$	The static magnetic field	T	2
$\vec{B}_e$	The Earth's magnetic field	T	13
β	Geometric sensitivity		6
$\vec{B}_p$	Polarizing magnetic field	T	13
$\vec{B}_1$	RF magnetic field	T	4
C	Capacitance	F	30
I	Current	A	19
D_c	Diameter of a coil	m	19
d_w	Wire diameter	m	19
E	Energy	J	2
ω_0	Larmor Frequency	$rad \cdot s^{-1}$	3
ϕ	Magnetic flux density	Wb	6
F_s	The frequency of sampling	Hz	56
γ	Gyromagnetic ratio	$Hz \cdot T^{-1}$	1
H_c	Height of a coil	m	19
L	Inductance	H	20
$\vec{L}$	Angular momentum	$N \cdot m \cdot s$	3
$\vec{\mu}$	Magnetic moment	$A \cdot m^2$	1
$\vec{M}$	Magnetization	$A \cdot m^{-1}$	6
N_{Echo}	Number of echoes in a sequence		10
N_{FFT}	Number of points used to perform an FFT		79
N_l	Number of layers on a coil		6
N_p	Number of protons		25
N_c	Number of turns per layer on a coil		6
ω	Angular frequency	$rad \cdot s^{-1}$	4
Q	Quality Factor		30

Symbol	Name	Units	First use on page
$R_{DS,on}$	On state resistance of a MOSFET	Ω	16
R	Resistance	Ω	7
ρ_e	Partial resistivity	$\Omega \cdot m$	7
ρ_m	Mass density	$kg \cdot m^{-3}$	25
R_{out}	Voltage source output impedance	Ω	40
δ	Skin depth	m	32
$\vec{S}$	Spin angular momentum vector of the nucleus	$N \cdot m \cdot s$	1
$\vec{s}$	Spin angular momentum vector per nucleon	$N \cdot m \cdot s$	1
T_1	Longitudinal relaxation time constant	s	8
T_2	Transversal relaxation time constant	s	8
T_2^*	Transversal relaxation time constant including homogeneities	s	8
T_{90}	Time between polarization cycle and 90°pulse	s	61
T	Temperature	K	7
θ	Rotation angle	rad	5
$T_{MeasWait}$	Time between 90°pulse and sampling start	s	56
$\vec{\tau}$	Torque	$N \cdot m$	3
T_{pol}	Polarization time	s	13
T_{pulse}	Pulse time	s	5
T_R	Repetition time	s	11
V_0	EFNMR signal amplitude, also equal to the magnitude of EMF	V	28
V_{DS}	Voltage between drain and source of a MOSFET	V	23
$V_{n_{amp}}$	Amplifier voltage noise amplitude	V	27
V_{env}	Environmental noise voltage amplitude	V	27
V_n	Johnson-Nyquist voltage noise amplitude	V	7

List of Figures

List of Tables

Table of Contents

Chapter 1

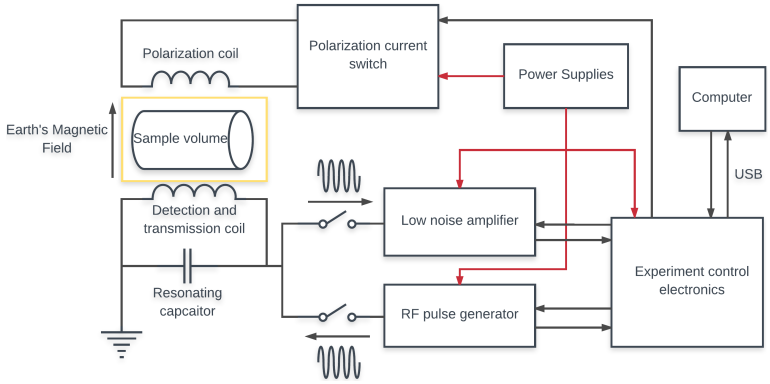

NMR Theory

To design an Earth's Field Nuclear Magnetic Resonance (EFNMR) setup, fundamental understanding of Nuclear Magnetic resonance (NMR) is required. Therefore, this chapter starts by explaining how NMR works in sections sections 1.1 to 1.6. This will be done using a classical mechanical description as much as possible. However, for completeness, 1.1 will exclusively use a quantum mechanical description, which will be linked to the classical mechanical description in 1.2.

1.1 Spins in an External Magnetic Field

Spin is a fundamental property of an elementary particle that arises from a rotating motion of the particle around its center of mass. It is quantized by the spin angular momentum vector, $\vec{s}$, and has both discretized magnitude, s, and orientation. Together with the neutron, the proton makes up one of two nucleons, which are present in all atoms. Both the proton and neutron have spin of magnitude $\frac{1}{2}$. The composition of neutrons and protons that form the atomic nucleus, determine the total nuclear spin, $\vec{S}$, equal to

$$\vec{S} = \sum_i \vec{s}_i, \tag{1.1}$$

where i is an individual nucleon. If S is zero, the atom is NMR inactive. Nuclei with half integer total spin $S = \left|\vec{S}\right|$, are NMR active and have a magnetic dipole moment. Nuclei with full integer values of S are also NMR active but have a magnetic quadrupole moment.

Magnetic moment of the atomic nucleus, $\vec{\mu}$, is related to the spin number S through the gyromagnetic ratio, γ, which is a constant property of the atom.

$$\vec{\mu} = \gamma \vec{S} \tag{1.2}$$

In table 1.1, an overview of several NMR active elements with a magnetic dipole moment is given. From these, hydrogen is the most commonly studied NMR active element. This is due to hydrogen's high NMR sensitivity and presence in many chemical compounds, most notably in water. In this report, the focus of EFNMR will also be on water. For a hydrogen atom, which consists only of a proton, the nucleus can have two different spin states commonly referred to as spin-up $\uparrow$, and spin-down $\downarrow$. Depending on the state, the $z-$component of magnetic moment is equal to

$$\mu_z = \pm \frac{\gamma \hbar}{2}, \tag{1.3}$$

where $\hbar$ is the reduced Planck's constant. These different states of μ_z have equal energy and thus the chance to find a particle in each of these states is equal. However, when the particle

Table 1.1: Overview of elements with a magnetic dipole or quadrupole moment, their gyromagnetic ratio and NMR sensitivity [44]

Element	Symbol	Spin number S	Gyromagnetic ratio $[MHz/T]$	Sensitivity relative to ^1H
Hydrogen	^1H	1/2	42.58	1
Carbon	^{13}C	1/2	10.71	0.0159
Oxygen	^{17}O	5/2	5.77	0.0291
Fluorine	^{19}F	1/2	40.08	0.8326
Sodium	^{23}Na	3/2	11.27	0.0925
Magnesium	^{25}Mg	5/2	2.61	0.0027
Phosphorus	^{31}P	1/2	17.25	0.0663
Sulfur	^{33}S	3/2	3.27	0.0023

is placed in a magnetic field, the energy levels split. This effect is known as the Zeeman effect [19] and is illustrated in figure 1.1. The energy difference between the two states, E, is

$$E = \vec{\mu} \cdot \vec{B}_0 \ , \tag{1.4}$$

where $\vec{B}_0$ is the magnetic field. Defining the magnetic field $\vec{B}_0$ to be aligned with the $z-$axis reduces the inner product to a multiplication

$$E = -\mu_z B_0 = \mp \frac{\gamma \hbar B_0}{2}. \tag{1.5}$$

Due to the minimization of energy that occurs, the lower energy level becomes favorable

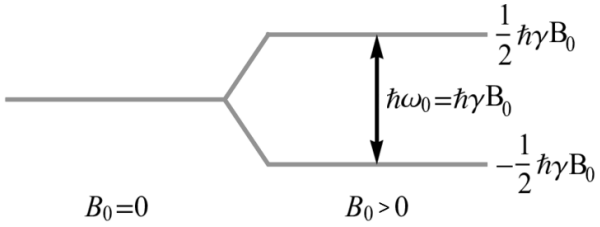

Figure 1.1: Zeeman splitting showing the different energy levels for a two-state spin system when energy splitting is small compared to thermal energy.

and the population of states shifts from thermal equilibrium. In a 2-state spin system, this is represented by a parallel or anti parallel alignment of magnetic moments to the magnetic field $\vec{B}_0$. Due to lower energy, parallel alignment is favorable.

1.2 Magnetic Moments and Torque

A hydrogen nucleus, which has half integer spin number, $S = \left|\vec{S}\right|$, has two possible spin states. Each of these two states has a different value for the z-component of magnetic moment, μ_z. Quantum mechanically, a single spin can thus have only two possible configurations. However, if an ensemble of spins is placed in the magnetic field, average magnetic moment per nucleus can take on values anywhere between $+\frac{\gamma\hbar}{2}$ and - $\frac{\gamma\hbar}{2}$. Therefore, to convert from quantum mechanical to a classical mechanical description, consider a magnetic moment to be capable of attaining any orientation and value.

In thermal equilibrium, magnetic moments are aligned either parallel or anti parallel to the field. If a magnetic moment is misaligned to the magnetic field, it experiences a torque, $\vec{\tau}$, equal to

$$\vec{\tau} = \vec{\mu} \times \vec{B}_0 \ . \tag{1.6}$$

Since the magnetic moment of nuclei is composed of spins rotating around their center of mass, nuclei have angular momentum, $\vec{L}$. According Newton's second law of motion, torque is equal to the time derivative of angular momentum,

$$\vec{\tau} = \frac{d\vec{L}}{dt} \ . \tag{1.7}$$

Combining equation 1.6 and 1.7, we obtain the law of motion

$$\frac{d\vec{\mu}}{dt} = \gamma \frac{d\vec{L}}{dt} = \gamma \left(\vec{\mu} \times \vec{B}_0\right) \ . \tag{1.8}$$

From the equation of motion, it can be seen that torque pulls misaligned magnetic moments back into alignment with the magnetic field. In $2D$, this can be compared to a compass needle misaligned with earth's magnetic field. Torque pulls the needle back into alignment of the magnetic field as governed by the equation of motion, 1.8. While doing so it will build up momentum and overshoot the external field direction, causing the torque's sign to flip and pull the needle back into alignment with the external magnetic field. Without damping, this process will continue and thus cause an oscillation of the needle.

In $3D$, this motion is not a simple oscillation but a precession around the axis of the magnetic field $\vec{B}_0$, from here on defined to always be in positive $z-$axis. The precession frequency, ω_0, is called Larmor frequency and depends only on magnetic field strength and gyromagnetic ratio of the nucleus.

$$\omega_0 = \gamma B_0 \tag{1.9}$$

For known magnetic field strength $B_0 = \left|\vec{B}_0\right|$, Larmor frequency of a nucleus can be directly related to its gyromagnetic ratio γ, which we already saw, was specific to the nucleus.

1.3 RF-Pulses and Rotating Reference Frame

In NMR, a misalignment of magnetic moments to the external magnetic field is stimulated using electromagnetic radiation with matching Larmor frequency, ω_0. More specifically, an alternating current is applied to an excitation coil, generating a magnetic field, $\vec{B}_1$, across the material, oscillating at Larmor frequency.

To understand how an oscillating magnetic field influences magnetic moments, a change of coordinates from the reference frame to a rotating frame is made. The reference frame is stationary to the observer and has coordinates $(\hat{x}, \hat{y}, \hat{z})$. The rotating frame rotates at angular frequency ω, around positive $\hat{z}-$axis, is stationary to the nucleus and has coordinates $(\hat{x}', \hat{y}', \hat{z})$. From this point forward, magnetic moments are in equilibrium oriented along the $\hat{z}-$ axis in both frames.

In the rotating frame, the spatial time derivative $\frac{\partial \vec{r}}{\partial t}$ becomes

$$\frac{\partial \vec{r}'}{\partial t} = \frac{d\vec{r}}{dt} - (\vec{\omega} \times \vec{r}) \ . \tag{1.10}$$

The temporal derivative for magnetic moment in rotating frame is

$$\frac{\partial \vec{\mu}'}{\partial t} = \frac{d\vec{\mu}}{dt} - (\vec{\omega} \times \vec{\mu}) \ . \tag{1.11}$$

Substituting equation 1.8 for $\frac{d\vec{\mu}}{dt}$ gives

$$\frac{\partial \vec{\mu}'}{\partial t} = \gamma \left(\vec{\mu} \times \vec{B}_0' \right) - (\vec{\omega} \times \vec{\mu}) \ . \tag{1.12}$$

Rearranging terms and using $\vec{a} \times \vec{b} = -\left(\vec{b} \times \vec{a}\right)$, we find

$$\frac{\partial \vec{\mu}}{\partial t} = \gamma \vec{\mu} \times \left(\vec{B}_0' + \frac{\vec{\omega}}{\gamma} \right) \ . \tag{1.13}$$

If an Radio Frequency (RF) magnetic field, $\vec{B}_1$, is applied in $x-y$ plane of the reference frame, oscillating at Larmor frequency, ω_0, equation 1.13 can be expanded to include both $\vec{B}_0$ and $\vec{B}_1$ as

$$\frac{\partial \vec{\mu}'}{\partial t} = \gamma \vec{\mu} \times \left(\vec{B}_0' + \vec{B}_1' + \frac{\vec{\omega}}{\gamma} \right) \ , \tag{1.14}$$

where $\vec{B}_0'$ and $\vec{B}_1'$ are respectively the fields $\vec{B}_0$ and $\vec{B}_1$, as observed in the rotating frame. Assume the resonant case where angular velocity of the rotating frame equals Larmor frequency, $\omega = \omega_0$. An observer within this frame will not observe precession such that $\vec{B}_0$ appears absent. Thus, the first and last term of equation 1.14 must cancel. If $\omega < \omega_0$, magnetic moments appear to precess at frequency $\omega_0 - \omega$ while if $\omega_0 > \omega$, precession appears at $\omega - \omega_0$. We conclude that in the rotating frame also $\vec{B}_0'$ should be adjusted to the effective $\vec{B}_{eff}' = \vec{B}_0' - \frac{\vec{\omega}}{\gamma}$, reducing equation 1.14 to

$$\frac{\partial \vec{\mu}'}{\partial t} = \gamma \vec{\mu} \times \vec{B}_1' \ . \tag{1.15}$$

This equation is similar to that of the torque on a magnetic moment in stationary frame. If the supplied electromagnetic radiation oscillates at Larmor frequency ω_0, the RF field will appear stationary in $x' - y'$ plane. In rotating frame, magnetic moments thus experience a torque and perform a pure rotational motion around $\vec{B}_1'$. However, one over-simplification

is made; we do not get the full amplitude of the $\vec{B}_1$ field in $x' - y'$ plane as we do in $x - y$ plane.

The RF field is linearly polarized and generated by a solenoidal coil centered on the $\hat{x}-$axes. In the stationary frame we have

$$\vec{B}_1 = B_1(t)\, cos(\omega t)\, \hat{x} \ . \tag{1.16}$$

The cosine can be expanded to a sum of two complex exponentials.

$$B_1 = B_1(t)\left(e^{i\omega t} + e^{-i\omega t}\right) \ . \tag{1.17}$$

Only right turning circular polarization interacts such that effectively half the amplitude of the $\vec{B}_1$ field is used. In the rotating frame we thus get

$$\vec{B}_1' = \frac{1}{2}|\vec{B}_1(t)|e^{-i(\omega-\omega_0)t}\hat{x}' \ . \tag{1.18}$$

Integrating equation 1.15 from $t = 0$ to $t = T_{pulse}$ during which $\vec{B}_1$ is present, assuming that the RF excitation field has constant amplitude in time, we find

$$\theta = 2\pi\gamma T_{pulse}\frac{1}{2}B_1 = \pi\gamma T_{pulse}B_1 \ . \tag{1.19}$$

By varying $\vec{B}_1$ and T_{pulse}, the rotation angle, θ, can be controlled. If θ is set perfectly to 90°, all magnetic moments are rotated from the $\hat{z}-$axis into the $x - y$ plane. A rotation of 90°along either the $\hat{x}-$ or $\hat{y}-$axis by use of electromagnetic radiation is called a 90°pulse. A rotation of 180°is referred to as a 180°pulse and can be applied around any axis. The use of these pulses is twofold. Firstly, it can rotate magnetic moments from positive $\hat{z}-$axis to negative $\hat{z}-$axis. Secondly, a 180°pulse can flip magnetization in $x' - y'$ plane.

1.4 Total Magnetization and NMR Signal

NMR is an inherently insensitive measurement technique. Since NMR works by rotating magnetic moments, it can only produce a nonzero signal is there is an average shift in the distribution of spin states. Considering the energy splitting due to the Zeeman effect, the shift from thermal equilibrium scales with the magnetic field strength, $\vec{B}_0$, relative to thermal energy.

A sample containing n nuclei placed in a homogeneous magnetic field, $\vec{B}_0$, has magnetization, $\vec{M}$, with magnitude, M_0, given by Curie's law,

$$M_0 = \frac{n\gamma^2\hbar^2 J\left(J+1\right)}{3k_B T} B_0 \ , \tag{1.20}$$

where J is the total angular momentum quantum number [27], k_B is Boltzmann's constant and $\hbar$ is the reduced Planck's constant. In the specific case of a proton in hydrogen, equation 1.20 reduces to

$$M_0 = \frac{n\gamma^2\hbar^2}{4k_B T} B_0. \tag{1.21}$$

From this equation, it can be seen that magnetization scales linearly with magnetic field strength, $\vec{B}_0$, and sample volume but inverse proportional with temperature, T. A sample of pure water placed at room temperature placed in an external field with strength $B_0 = 1T$, has average magnetization per nucleus of only $4.9 \times 10^{-32}\ A/m$.

Assume that all magnetic moments in a sample are forced away from their equilibrium alignment to the $\hat{z}-$axis, by a 90°RF pulse and are rotated into the $x-y$ plane. Once the RF magnetic field is removed, only the static field, $\vec{B}_0$, remains. In this static field, magnetic moments experience a torque and precess around the $\hat{z}-$axis. The total coherent precession of all individual magnetic moments makes the total net magnetization, $(\vec{r}, t)$, oscillate at Larmor frequency. Due to the change in magnetization, magnetic flux through an open surface will also oscillate. Following Faraday-Lenz law of induction, a time varying magnetic flux generates an Electro Motive Force (EMF) in an open conductor on its border equal to:

$$emf = -\frac{d\phi}{dt}. \tag{1.22}$$

EMF can be measured as function of time, which defines the NMR signal detection method. The total magnetic flux, ϕ, through an open surface is defined by the surface integral

$$\phi = \mu_0 \iint M\left(r, t\right) dA, \tag{1.23}$$

where μ_0 is the magnetic permeability of vacuum. When the conductor is a coil with N_c turns per layer and N_l layers, the total EMF generated equals

$$emf = -N_c N_l \frac{d\phi}{dt}. \tag{1.24}$$

Transforming equation 1.23 for magnetic flux, ϕ, to a volume integral and entering the $x-y$ component of magnetization, we find

$$\phi = \mu_0 \iiint M_{xy} \beta dV, \tag{1.25}$$

where β is the geometric sensitivity of the coil. Assume a perfect distribution of magnetization across the inner volume of the solenoid such that M_{xy} can be taken out of the integral.

Furthermore, M_{xy} is generalized to $M_{xy}cos\,(\omega_0 t)$, since it is known that magnetization oscillates in $x-y$ plane at Larmor frequency. Magnetic flux, ϕ, is now equal to

$$\phi = \mu_0 M_{xy}\ cos\,(\omega_0 t) \iiint \beta dV. \tag{1.26}$$

and EMF is equal to

$$emf = -\mu_0\omega_0\ N_c N_l\ M_{xy} sin\,(\omega_0 t) \iiint \beta dV. \tag{1.27}$$

Assume that all magnetization which in equilibrium is aligned along the $\hat{z}-$axis, is rotated into the $x-y$ plane. Then, M_{xy} is equal to the total net magnetization, M_0. Entering this in equation 1.27 and substituting equation 1.21 we find:

$$emf = -\mu_0\omega_0 N_c N_l sin\,(\omega_0 t)\, M_0 = -N_c N_l \mu_0\omega_0 \frac{n\gamma^2\hbar^2}{4k_B T} B_0 sin\,(\omega_0 t)\ . \tag{1.28}$$

As can be seen, EMF scales linearly with both Larmor frequency, ω_0, magnetic field strength, $\vec{B}_0$ and total number of turns on the solenoid. To summarize, EMF thus scales with the square of field strength.

The best achievable Signal-to-Noise Ratio (SNR) of an NMR experiment is determined by the ratio of induced EMF and minimal noise. The least amount of noise that can be achieved in an NMR experiment is that of the Johnson-Nyquist voltage noise of the coil. Johnson-Nyquist noise originates from thermal fluctuations in the motion of electrons passing through a conductor. These fluctuations are promoted by resistance and temperature of the material. Johnson noise is a voltage noise and has amplitude, V_n, equal to

$$V_n = \sqrt{4k_B T R \Delta f}, \tag{1.29}$$

where k_B is Boltzmann's constant, T temperature, R the coil's resistance and Δf the spectral bandwidth. For a solenoidal coil with N turns, in general resistance is a function of the length, l, Cross Sectional Area (CSA) and material resistivity, ρ_e. When frequencies above several MHz are to be conducted in the coil, skin effect [19] makes current flow mainly on the skin of the conductor, thereby effectively increasing the conductor's resistance. The resistance of a coil, including the skin effect can be given in equation form as [23]

$$R = \frac{l}{p}\sqrt{\frac{\mu_r\omega_0\rho_e\,(T)}{2}}\ , \tag{1.30}$$

where p is the circumference of the conductor. If we use the definition of SNR and seperate physical constants from coil and sample parameters we get an expression for SNR equal to

$$\frac{\mu_0\hbar^2}{\left(\frac{\mu_r\rho_e(T)}{2}\right)^{1/4}\sqrt{(4k_B T)^3}} \frac{N_c N_l p n \gamma^2 B_0 \omega_0^{3/4}}{\Delta f l}\ . \tag{1.31}$$

Since $\omega_0 = \gamma B_0$, SNR thus scales to the power $\frac{7}{4}$ with magnetic field strength, $\vec{B}_0$.

1.5 Relaxation

Relaxation describes how magnetic moments become realigned with the static field, $\vec{B}_0$. Processes involved in NMR relaxation are characteristic to a nucleus and its environment. Therefore, meaningful properties of the material can be determined from relaxation characteristics. Multiple processes lead to relaxation, which can be divided into two categories, transversal and longitudinal relaxation.

Longitudinal relaxation is relaxation of the longitudinal component of magnetization, M_z, aligned along the $\hat{z}-$axis in both the stationary and rotating frame. The time scale on which longitudinal relaxation occurs is characterized by T_1 and a commonly used name is therefore T_1 relaxation. A material has initial longitudinal magnetization $M_z\,(0)$ after an RF pulse has been applied. As function of time, t, M_z relaxes back to its equilibrium value, M_0, as

$$M_z\,(t) = M_0 + [M_z\,(0) - M_0]\,exp\left(-\frac{t}{T_1}\right). \tag{1.32}$$

Typical values of T_1 for hydrogen in water are of the order of hundreds milliseconds to a few seconds.

The second relaxation mechanism in NMR is transversal relaxation of magnetization in the transversal plane i.e. the $x-y$ plane or $x^{'}-y'$ plane. Transversal relaxation is characterized by time constant T_2. Imagine an ensemble of magnetic moments, rotated from positive $\hat{z}$-axis into the transversal plane by a 90°RF pulse. As magnetic moments relax back to the longitudinal axis, they precess around the $\hat{z}$-axis due to the torque induced. If different moments in the sample experiences a slightly different local magnetic field, they will precess at different rates, some slightly faster or slower than the bulk. Net coherent magnetization in the transversal plane reduces as various spins obtain different phases. This is referred to as dephasing. The equation governing transversal magnetization M_{xy} over time is given by

$$M_{xy}\,(t) = M_t\,(0)\,exp\left(-\frac{t}{T_2}\right) \tag{1.33}$$

Typically, but not per se, T_2 has to be smaller than $2T_1$ [54]. If macro- or microscopic inhomogeneities, $\Delta\vec{B}_0$, are present in the static magnetic field, $\vec{B}_0$, or additional effects are present which reduce phase coherence, T_2 is decreased to T_2^*. In equation form:

$$\frac{1}{T_2^*} = \frac{1}{T_{2,B}} + \frac{1}{T_{2_{inh}}} + Other = \frac{1}{T_{2,B}} + \gamma\Delta B_0 + Other \tag{1.34}$$

where $T_{2,B}$ is the bulk relaxation time of the material and $T_{2_{inh}}$ is a timescale for static magnetic gradients, $\Delta\vec{B}_0$ the magnetic field gradient in T/m and $Other$ are additional effects such as time varying Larmor frequency, leading to a decreased T_2^* time. Like T_1, T_2 can be used to characterize a material and environment. Typical values of T_2^* range from several milliseconds to T_1. As an example of variation in T_2^* values depending on environment, consider water present in a porous material. Close to the wall, magnetic moments interact with the wall different from the material in the bulk. This difference, and the ratio of bulk to wall area, influences T_2 values. The value of T_2 in a porous material can thus be used to determine mean pore size. [14, 28, 29].

To generalize the magnetization as function of time, the Bloch equations are used [6].

$$\frac{dM}{dt} = \gamma M \times B_0 + \left(-\frac{1}{T_2}M_x x,\ -\frac{1}{T_2}M_y y, \frac{1}{T_1}\left(M_0 - M_z\right) z\right) \tag{1.35}$$

The first term is the pure precession at Larmor frequency, the second term in $\hat{x}$- and $\hat{y}$-direction are due to transversal relaxation and the z-component due to longitudinal relaxation.

1.6 Pulse Sequences

Prior to this section, the origin of NMR signals, how they can be stimulated using RF fields as well as detection and relaxation mechanisms have been analyzed. Pulse sequences are standardized orders of excitation and detection. Sequences used in this work are given here. For each sequence, the ability of measuring either net magnetization or decay times T_1 and/or T_2, will be given.

Free induction decay

Free Induction Decay (FID) requires only a single pulse to work. Therefore, it is the simplest NMR experiment. To obtain an FID, a 90°RF-pulse along either $\hat{x}-$ or $\hat{y}-$axis is applied to the sample causing net magnetization to be rotated into the transversal plane creating transverse magnetization. Dephasing starts at the end of the pulse and the net magnetization in the transversal plane produces an FID that decays with time constant T_2^*. Time $t = 0$ is defined as the end of the pulse, and the beginning of the FID.

Spin echo sequence

An FID is the simplest NMR experiment. However, it is difficult to use it for determining material properties. This is because after RF power has been applied to the material, transient decay in the coils and material influence net magnetization such that the resulting signal cannot be uniquely related to the sample. To avoid these issues, a spin echo sequence can be used.

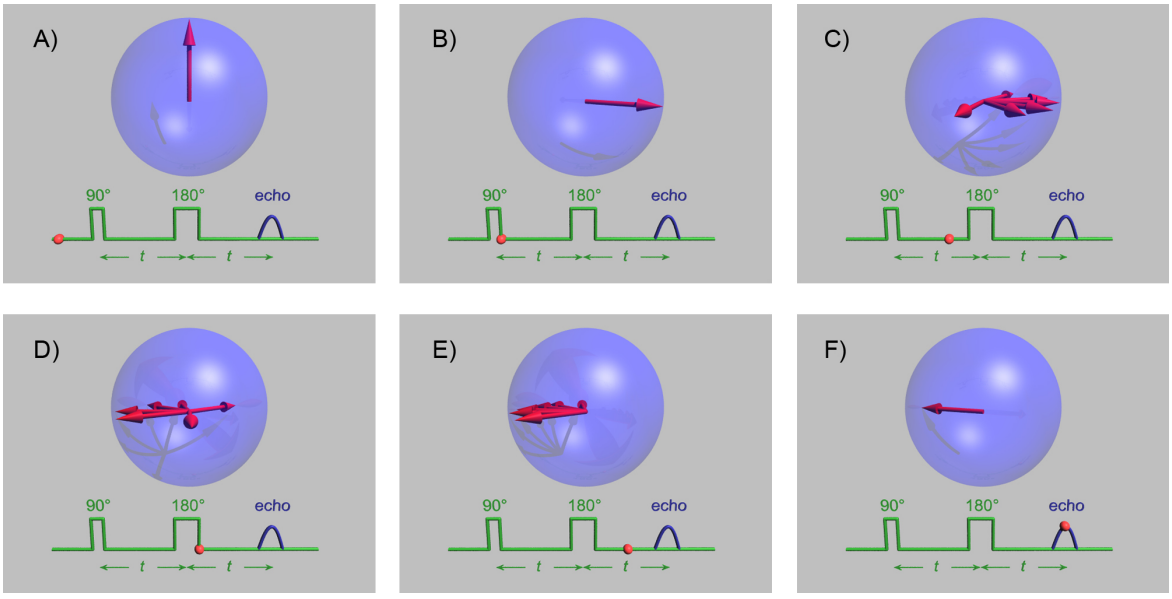

Figure 1.2: Graphic representation of the phases of different magnetic moments in a spin echo sequence as function of time [55]. $\hat{z}$ axis aligned vertical

In a spin echo sequence [20], a 90°pulse is applied along the $\hat{x}-$axis. This is graphically depicted in the transition from image (a) to (b) in figure 1.2. As dephasing begins, net transversal magnetization induces an FID in the detection coil $(b) \rightarrow (c)$. After $\frac{T_{Echo}}{2}$, where T_{Echo} is the echo time, a 180°RF-pulse along the $\hat{y}-$axis is applied $(c) \rightarrow (d)$ effectively flipping the orientation and also reversing the rotation direction of the spins. As magnetic moments rotate backwards to their original position (e), all at the same rate with which they initially were rotating before the RF-pulse, moments re-phase in the transversal plane

producing a coherent secondary signal (f), increasing in amplitude. After maximum phase coherence, de-phasing again begins causing a decaying amplitude of yet another FID. These two signals together, centered on time T_{Echo} together form an echo. Without influences from diffusion, peak amplitude of the echo decreased as function of T_{Echo} as

$$M_t(t) = M_t(0)\, exp\left(-\frac{T_{Echo}}{T_2}\right) \tag{1.36}$$

Since the echo occurs $T_{Echo}/2$ after the RF pulse, results are not influenced by transient decays. Moreover, small local inhomogeneities in the magnetic field that cause additional T_2 relaxation are compensated for since each spin is simply flipped as it re-phases at its own local Larmor frequency.

If all inhomogeneities are compensated by the 180°pulse, then multiple spin echo measurements can be made that vary T_{Echo}. The resulting peak amplitudes for varying T_{Echo} could be fitted to an exponential that determines both relaxation time T_2 as well as initial magnetization, $\vec{M}$. However, effects of magnetic moments moving in the sample due to diffusion or fluid flow are not compensated when T_{Echo} is larger than the timescale of those processes. Therefore, an echo amplitude decay curve will not be an exponential.

CPMG sequence

The Carl Purcell Meyboom Gill (CPMG) sequence is an extended version of the spin echo sequence [13]. Unlike the spin echo which only uses a single 180°pulse, the CPMG sequence uses N_{Echo} 180°pulses centered on $\left(\frac{2n-1}{2}\right)T_{Echo}$, to form a train of echoes. Using only a single CPMG sequence, T_2 can determined whereas the spin echo sequence requires multiple measurements. Moreover, for closely spaced echoes, the CPMG sequence also reduces diffusion effects. More specifically, the added timescale due to diffusion, $T_{2,D}$, can be expressed as

$$\frac{1}{T_{2,D}} = D\frac{(\gamma G T_{Echo}/2)^2}{3} \tag{1.37}$$

where G is the magnetic field gradient in T/m and D is the diffusion constant in m^2/s [28]. For arbitrarily small values of T_{Echo}, $T_{2,D}$ can be made negligibly small such that unlike a spin echo sequence, T_2 can be measured.

An apparent issue with the CPMG sequence is that the flip angle of each pulse must be exactly 90°for the initial pulse, and exactly 180°for all subsequent pulses. If for instance the 180°pulses are offset only be a few degrees, phase errors will accumulate over time leading to a degradation in the signal coherence, thus underestimating T_2. To overcome this issue, the initial 90°pulse is applied 90°out of phase with respect to the subsequent 180°pulses. That means that if the initial 90°is an $\hat{x}$-pulse, all subsequent 180°pulses must be $\hat{y}$-pulses. This process is called phase modulation and both $\hat{x}, \hat{y}, \hat{y}, \hat{y}, \hat{y},$ and $\hat{y}, \hat{x}, \hat{x}, \hat{x}, \hat{x}, \hat{x},$ CPMG sequences can be used. If phase modulation is used, flip angle errors do not accumulate over time [50] and thus do not influence the measured T_2 time.

Inversion recovery sequence

Using spin echo and CPMG sequences, only T_2 can be determined. However, T_1 is also a desirable quantity. To determine T_1, the inversion recovery can be used. This sequence starts with a 180°pulse along either $\hat{x}-$ or $\hat{y}-$axis and rotates net magnetization from positive to negative $\hat{z}-$axis. After inversion time T_1, a 90°pulse is applied rotating the magnetization from negative $\hat{z}-$axis into the $x-y$ plane, creating transversal magnetization and an FID. A 180°pulse is applied $\frac{T_{Echo}}{2}$ after T_I, creating a coherent echo centered at $t = T_I + T_{Echo}$. The inversion recovery is thus a spin echo sequence with an additional 180°pulse added in front of it.

The signal amplitude of the FID and echo following the 90°pulse decay with T_2 just as in the spin echo sequence. The inversion time, T_I, makes the longitudinal magnetization decay with T_1. Using multiple measurements that vary T_1, T_1 can be determined from a fit of the signal amplitudes of the FID and echo if the echo time, T_{Echo}, is kept constant.

Repeating experiments

Repetition time, T_R, between two consecutive experiments can influence the total longitudinal magnetization of a sample. If T_R is chosen too small, longitudinal relaxation will not have been fully restored by T_1 relaxation causing a decay in total signal amplitude, S, as

$$S = S_0 \; e^{-T_{Echo}/T_2} \left(1 - e^{-T_R/T_1}\right) \; , \tag{1.38}$$

where S_0 is the signal intensity at the beginning of the first experiment. Typically, T_R is chosen to be $3T_1$ such that $1 - e^{-T_R/T_1} \sim 0.95$.

Chapter 2

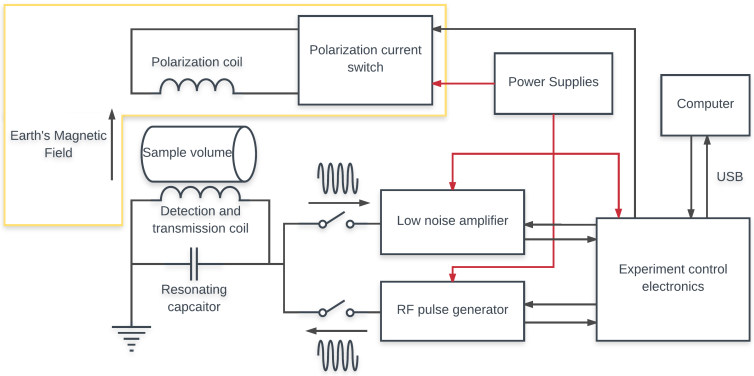

Earth's Field NMR

In chapter 1, we found that when a nucleus with nonzero spin is placed in a magnetic field, multiple states with different energy levels are possible. We also found that this quantum mechanical description can be linked to a classical description using magnetic moments. When magnetic moments are manipulated using RF electromagnetic radiation, Larmor precession can occur, changing the total magnetization of a sample. Subsequently, this induces an EMF in a detection coil. By measuring this EMF, the NMR detection method is defined. To conclude chapter 1, relaxation processes which dampen Larmor precession after RF pulses are applied to a sample were described and some standardized pulse sequences used in this work were given.

Summarizing previous chapter, we have focused mainly on the first stage of NMR, the sample. In this chapter, we will shift our focus to the next step in an NMR experiment. To do so, we will first discuss a traditional NMR experiment and the issue of achieving the goals set within the goal of this work. After that, we will discuss using the Earth's magnetic field to perform Earth's Field Nuclear Magnetic Resonance (EFNMR) experiments. Finally, limitations and challenges of EFNMR will be discussed after which hardware required specifically for EFNMR will be explained.

2.1 Working Principle of Traditional NMR

In section 1.4, we saw that SNR of an NMR experiment scales with the power 7/4 to the magnetic field strength used [23]. Therefore, in a traditional NMR experiment, the static magnetic field, $\vec{B}_0$, is typically made as strong and homogeneous as possible to maximize signal intensity. This allows measurements of small samples or even individual regions in a larger sample with an SNR and T_2 as high as possible. Both stimulation and measuring of NMR signals is performed using a single or multiple tuned coils aligned perpendicular to the static field, $\vec{B}_0$. The EMF induced across a detection coil is amplified and sampled by an Analog-to-Digital Converter (ADC) after which it is analyzed by a computer.

A commonly used field strength in clinical applications is 1.5 $Tesla$. Following equation 1.9, Larmor frequency, ω_0, of hydrogen at this field strength is roughly $64MHz$. Sampling a signal at such high frequencies is far from trivial and requires complex, expensive electronics. Moreover, generating a high strength static $\vec{B}_0$ field requires high power consuming electromagnets or superconducting liquid-nitrogen or -helium cooled magnets. This makes it impossible to reach the goal of producing a setup for under €500.

Finally, to obtain good SNR, $\vec{B}_0$ needs to be sufficiently homogeneous to effectively control field strength and thus Larmor frequency across the sample. $\vec{B}_0$ Inhomogeneity results in differing resonance frequencies depending on the position limiting maximum sample size. An alternative to these technically challenged traditional NMR setups is provided in EFNMR.

2.2 Working Principle of Earth's Field NMR

In EFNMR, the permanently available earth's magnetic field, $\vec{B}_e$, is used as $\vec{B}_0$. Hereby, the requirement of producing a static magnetic field is removed. This greatly reduces both complexity and cost of a setup. Moreover, due to its inherent spatial homogeneity, it allows the usage of large samples.

Unfortunately, earth's magnetic field is also very weak, around $50\mu T$ [17]. Consequently, Larmor frequency is much lower than obtained in traditional NMR. This lowering of frequency decreases signal intensity as can be seen from equation 1.28. More specifically, signal intensity at $50\mu T$ is almost 900 million times lower than at $1.5T$. However, SNR of an EFNMR measurement is relatively higher than for a traditional NMR measurement since skin effect does not play a role and SNR thus scales with B_0^2. Compared tp $1.5T$, EFNMR SNR is over 800 million times lower for constant sample volume. Despite the homogeneity of earth's magnetic field being an advantage, it is also a necessity due to the low signal intensity per sample volume. Fortunately, the lower Larmor frequency allows much simpler and cheaper signal acquisition and pulse generating hardware to be used, as compared to traditional NMR.

To boost low EFNMR signal amplitude, the Varian Packard method (1954) is used [43]. This method relies on a polarizing magnetic field, $\vec{B}_p$, several times larger than earth's magnetic field, $\vec{B}_e$. This allows more magnetic moments to contribute to the signal, following Curie's law. During a polarization cycle, the static magnetic field, $\vec{B}_0$, in equation 1.21 is effectively replaced by the sum of $\vec{B}_e$ and $\vec{B}_p$, $\vec{B}_{eff}$. The angle α between $\vec{B}_e$ and $\vec{B}_p$ is the angle under which the magnetization vector, $\vec{M}$, is aligned.

The polarizing field is generated by passing a current, I, through a solenoidal coil aligned perpendicular to earth's magnetic field, but coaxial with the detection and excitation coil. This coil does not necessarily need to produce a homogeneous field. [1] Graphically, the EFNMR setup is depicted in figure 2.1. When the polarizing current is switched on, similar

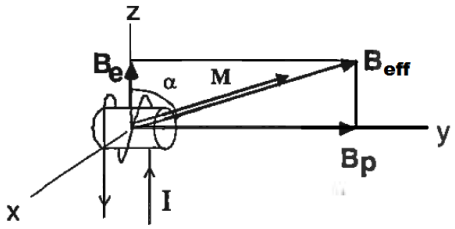

Figure 2.1: Graphic representation showing the various magnetic fields in an EFNMR setup.

to the decaying case, net longitudinal magnetization, M_z, develops in the sample with time constant T_1 as

$$M_z(t) = M_0\left(1 - e^{-\frac{t}{T_1}}\right). \tag{2.1}$$

After polarization time T_{pol}, $\vec{B}_p$ is removed by switching off the current in the coil. From this point forward, a separation can be made in the way that this is achieved, either slow and adiabatic, or fast and non-adiabatic. These two methods result in different behavior in the alignment of net magnetization, depending on the rate at which current in the coil turns to zero. Both methods will be analyzed in section 2.4.

[1] The polarizing coil used in the Varian Packard method only needs to produce a strong magnetic field which makes the production of such a coil simple by nature. Only when the setup is used for imaging, the inhomogeneous polarizing field spatially distorts signal intensity. This can be overcome by, for example, winding additional turns at the ends of the coil, increasing homogeneity. [15, 33]

2.3 History of EFNMR

Based on the original work of Varian and Packard (1954) [43] several research groups have employed EFNMR in their work. In 1957, Powles and Cutler [46] studied influences of ferromagnetic disturbances on T_2 and T_2^* relaxation times to which they found even brick walls to be of unacceptable magnetic disturbances when measuring EFNMR in fluids with long relaxation times of several seconds. In the seventies, the French group of Rocard and Bené were one of the most active groups to actively build and research EFNMR [4, 35] focusing on various aspect of the topic, including reducing dead-time and also influences of ferromagnetic disturbances. Moreover, Bené used EFNMR to study decay times of human tissues and liquids in hospital areas [4, 5] and was the first to use non-adiabatic spin-echo sequences in EFNMR. These setups typically used only a single solenoidal coil with a switching circuit to operated both polarization as well as detection cycle. Optimizing damping time after switching transients provided topic of many research papers [5, 7] and soon also setups began to emerge employing multiple coils [53] to both separate the polarization and detection coils.

Sir Paul Callaghan -who was president of the International Society of Magnetic Resonance- and his group have also contributed greatly to EFNMR. Most importantly, with their on non-adiabatic transitions in 1982 [35]. Moreover, their work on EFNMR in Antarctica [8,10,39] is world famous. The arctic is an environment where virtually no environmental noise exists and relaxation times are very long due to extremely high $\vec{B}_0$ inhomogeneity up to $0.0024 ppm/m$ [39]. As comparison, typical Magnetic Resonant Imaging (MRI) scanners obtain $10 ppm/m$ whereas spectroscopy requires at least $1 ppm/m$ or better [33]. Later, Callaghan helped found and develop what is today the commercially available EFNMR apparatus, the Magritek Terranova [1].

Imaging in the earth's magnetic field was first performed by Stepsinik's group in Ljubljana, starting in 1993 with their paper on self-diffusion measurements in strong gradients [51]. Callaghan launched an expedition to the arctic using their technique of pulsed gradient spin echo to measure diffusion in sea ice. Several years later, Stepisnik and Callaghan combined their effort on studying fluid motion and diffusion in NMR experiments [12]. Moreover, Stepisnik published more general work on imaging in the earth's magnetic field [41]. Results from his work on magnetic gradients in EFNMR would later be incorporated into the Magritek Terranova [21].

Besides conventional applications of EFNMR such as geomagnetic surveying and material identification, work is also done on more exotic applications such as detection of liquid explosives [16].

2.4 Adiabatic and Non-adiabatic Current Switching

When current and thus polarizing field are quickly and non-adiabatically removed, the only remaining magnetic field is earth's magnetic field [36,38]. Due to alignment of net magnetization perpendicular to this field, magnetic moments in the sample experience a torque and an FID follows. Using this non-adiabatic method, removal of $\vec{B}_p$ is followed by an FID. The non-adiabatic Varian-Packard method allows measurement of only T_2^* but not T_1 or T_2. The non-adiabatic method appears commonly in Proton Precession Magnetometer (PPM) where the sole purpose of a device is measuring earth's magnetic field strength as derived from the Larmor frequency. An illustration of the non-adiabatic Varian-Packard method with FID is shown in figure 2.2.

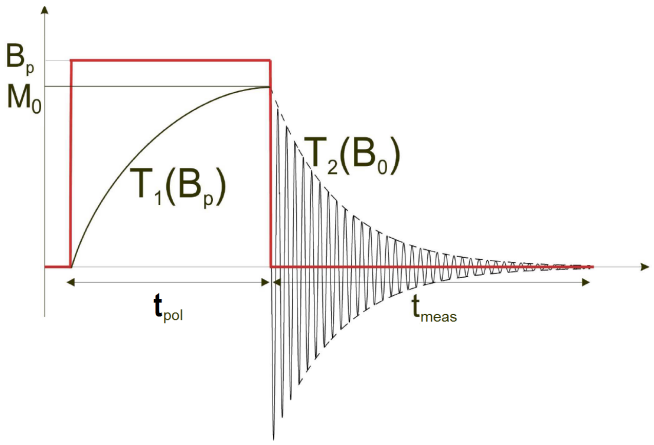

Figure 2.2: Graphic representation of the non-adiabatic Varian Packard method [33]

A second possibility of EFNMR, whilst still using the Varian Packard method to create additional magnetization is to turn off the polarizing field adiabatically. This method, first used by Callaghan [11], follows Ehrenfest's theorem. According to Ehrenfest's adiabatic theorem, a transition between states can be considered adiabatic if the change of external conditions occurs on a timescale T_{Echo} much larger than the internal rate of change t_i i.e. $T_{Echo} \gg t_i$ [24]. For EFNMR this means that the removal of the polarizing field needs to occur over several phase cycles at Larmor frequency ω_0

$$2\pi t_{removal} \gg \frac{1}{\omega_0}. \tag{2.2}$$

When this is done, net magnetization follows the direction of the effective magnetic field $\vec{B}_{eff}$, as it is effectively rotated from the initial angle α towards the earth's magnetic field direction. After this process finishes, all magnetization is realigned with the earth's magnetic field and no FID is produced. During this rotation of magnetization from the $x-y$ plane towards positive $\hat{z}-$axis, T_1 decay will already begin, decreasing maximum signal amplitude compared to a non-adiabatic experiment. However, conditions for an adiabatic transition are met much easier compared to a non-adiabatic transition [24, 37]. Graphically, the adiabatic EFNMR experiment is depicted in figure 2.3.

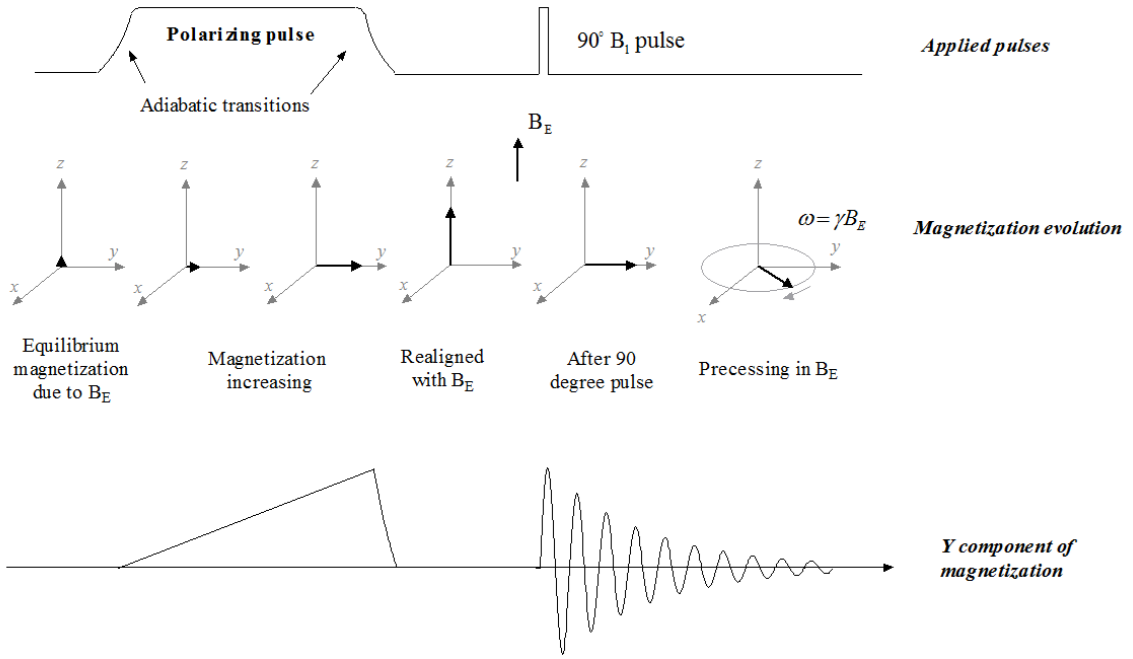

Figure 2.3: Graphic representation of the adiabatic EFNMR FID. [1]

Switching methods

So far we have only considered switching current with different speeds without describing how this can be achieved. Several methods can be used to switch current. These are mechanical switches, which come in all sorts of relays, or semi-conductor switches. A mechanical switch can be designed to switch almost any current required in a reliable device which is easy to implement, whereas a solid state device requires more design attention. A mechanical relay is thus a good option since it is easy to use and reliable, a good fit to the goals in this research. However, switching action of a mechanical relay is always time delayed relative to sending the control signal to switch it. Moreover, this delay varies per execution. Since current switching in EFNMR must be performed with high temporal resolution, using a relay will result in low repeatability. Therefore, we must use a semi-conductor switch.

Multiple sorts of semi-conductor switches exist, such as solid state relays (SSR), IGBT or Metal Oxide Semiconductor Field Effect Transistor (MOSFET) devices. Out of these, a MOSFET best suits our needs since it has low resistance while on, $R_{DS,on}$, can switch ample current needed for our experiment and can be easily controlled. Using a mechanical relay, polarization current can be switched both before as well as after the coil. Using a MOSFET switch however, two configurations can be used, high-side or low-side switch. These are illustrated in figure 2.4.

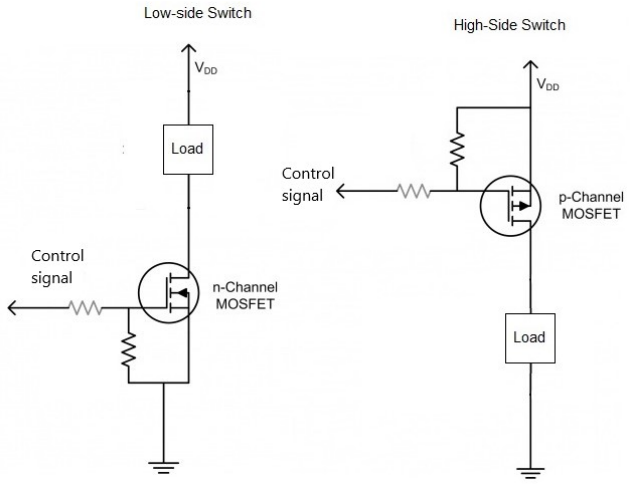

Figure 2.4: Low-side and high-side MOSFET switch. The load represents the polarization coil and V_{DD} the power supply.

For the high-side switch, commonly a P-type MOSFET is used whereas for the low-side switch an N-type MOSFET is used. [1] The main consideration for choosing a low-side or high-side switch can be found in the way a load is connected. If a low-side switch is used, the load floats and is thus not connected to ground, which can be a hazardous condition if the circuit is not perfectly isolated. Contrary, the low-side switch can switch more current than a high-side switch due to the construction of N-type MOSFETs which has lower on state resistance, $R_{DS,on}$. Considering applications of the EFNMR setup, safety concerns outweigh the current switching capability and a high-side switch is chosen.

Using the high-side MOSFET switch, a non-adiabatic experiment can be performed by simply switching the current off as fast as possible. For an adiabatic experiment, current needs to be switched much slower. This can be achieved by connecting a capacitor in parallel to the polarization coil. When the MOSFET is switched off, the capacitor releases its charge through the polarization coil. The speed at which this occurs is described more thoroughly in section 2.7 and the exact implementation of the current switch is given in section 4.2.

[1] A high-side and low-side switch can also be constructed using N-type and P-type MOSFETs, respectively. However, control of these switches is much more difficult and therefore typically not used.

2.5 Generalized EFNMR Sequences

In section 1.6, spin echo, CPMG and inversion recovery sequences are described assuming traditional NMR. In the Varian Packard method, the polarizing field, $\vec{B}_p$, is enabled before a pulse sequence is performed. In EFNMR experiments, all generalized NMR sequences are thus preceded by a polarization cycle of duration T_{pol}. Time $t = 0$ is defined as the time at which the current in the coil is switched off. A graphic depiction of the adiabatic spin-echo following an adiabatic pre-polarization cycle is shown in figure 2.5. In NMR, the

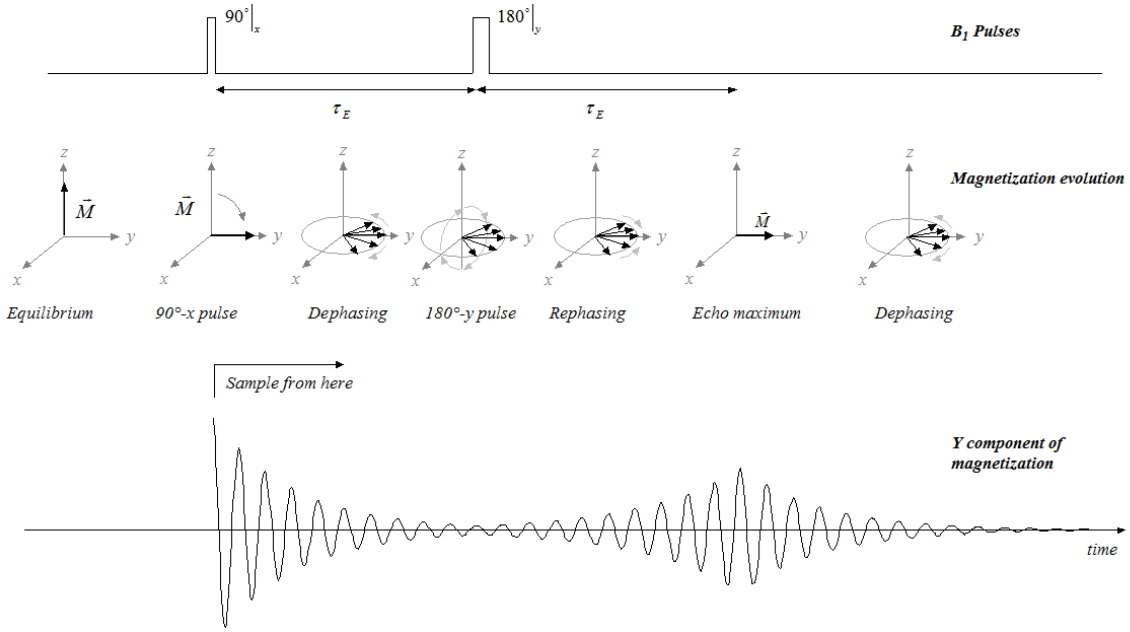

Figure 2.5: Graphic representation of the adiabatic spin echo following an adiabatic pre-polairzation cycle. [1]

inversion recovery sequence can be used to measure T_1. Using EFNMR, a second method exists. During a polarization cycle, magnetization also grows over time with time constant T_1. Therefore, if multiple EFNMR spin echo or CPMG sequences are performed, keeping echo time T_{Echo} constant but varying the polarization time T_{pol}, T_1 as well as initial of the sample can be measured by fitting the FID and/or echo amplitudes to $T_{pol} + T_{Echo}$. Since creation of additional magnetization during the polarization cycle follows the same T_{pol} increase in amplitude, this adds several times T_{pol} to the repetition time between subsequent sequences.

2.6 Solenoidal Coils

The polarization coil will be produced as a solenoidal coil. This is because a solenoidal coil is easy and cheap to produce and has high magnetic field homogeneity. In this section several general properties of solenoidal coils are derived. These properties include the coil's resistance, magnetic field strength and magnetic field homogeneity on axis, as well as the coil's inductance.

The resistance, R, of a piece of circular wire is

$$R = \frac{\rho_e l_w}{A_w} = \frac{4\rho_e l_w}{\pi d_w^2}, \tag{2.3}$$

where ρ_e is the resistivity of the wire material, l_w is the length of the wire, d_w the diameter of the wire and A_w its cross sectional area (CSA). For a solenoidal coil with diameter D_c, height H_c, number of turns per layer N_c and number of stacked layers N_l, the total wire length l_w will in first order approximation be equal to $l_w = \pi D_c N_c N_l$. To help understand the various parameters used in quantifying a solenoidal coil, a technical drawing of a general solenoidal coil is shown in figure 2.6.

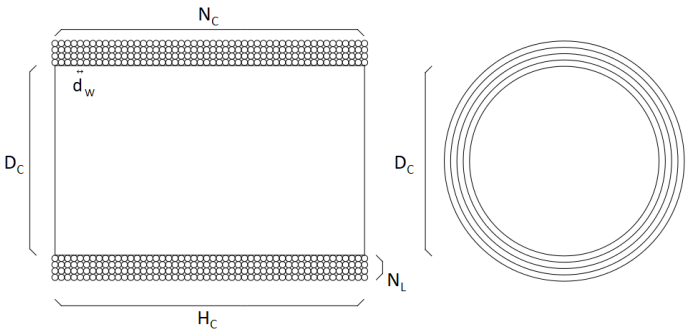

Figure 2.6: Technical drawing of the sample coil, indicating wire diameter, d_w, height of the coil, H_c, diameter of the coil, D_c, number of windings per layer, N_c, and number of layers, N_L.

As we will see, magnetic field strength is a function of the number of turns, N_c. Therefore, it makes sense to also rewrite the resistance to be a function of N_c, instead of wire diameter, d_w. Wire diameter, d_w, is equal to $d_w = H_c/N_c$. This gives for the resistance of the total length of wire on the coil

$$R = \frac{4\rho_e D_c N_c^3 N_l}{H_c^2} \ . \tag{2.4}$$

For an infinitely long solenoidal coil, with its axis aligned coaxially to the $\hat{x}$-axis, the magnetic field, B, generated in it has only an x-component, B_x, equal to

$$B_x = \frac{\mu_0 N_l N_c}{H_c} I \ , \tag{2.5}$$

where μ_0 is the magnetic permeability of vacuum and I the current passing through the coil. The infinitely long coil is a simplification only valid for coils with high aspect ratio of height to diameter. For more general solenoidal coils, the coaxial component of on-axis magnetic field strength, can be found using the Biot-Savart law. [19]

Assume a solenoid of radius R aligned with the x-axis centered at $x = 0$, stretching from $x_1 = -\frac{H_c}{2}$ to $x_2 = \frac{H_c}{2}$. Per unit length dx', a current of $\frac{N_c N_l}{H_c} I dx'$ circulates. Using the

Biot-Savart law evaluated at distance x from the center of a ring of width dx' centered at $x = x'$, a magnetic field dB_x is present equal to

$$dB_x(x) = \frac{\mu_0}{2}\frac{N_c N_l I}{H_c}\frac{R^2}{\left[(x-x')^2 + R^2\right]^{3/2}}dx' \ . \tag{2.6}$$

By integrating, we find for the x-component of the magnetic field $B_x(x)$:

$$B_x(x) = \int_{x_1}^{x_2} dB_x(x) = \frac{\mu_0 N_c N_l I}{2H_c}\left(\frac{x-x_1}{\sqrt{(x-x_1)^2+R^2}} - \frac{x-x_2}{\sqrt{(x-x_2)^2+R^2}}\right) \ . \tag{2.7}$$

Inspecting equation 2.7, it can be seen that the limit case $\frac{H_c}{R} \gg 1$ is equal to equation 2.5 for the magnetic field of an infinitely long coil.

Homogeneity of the magnetic field at constant current and number of layers, depends only on the aspect ratio of the coil H_c/R. In figure 2.7, normalized magnetic field strength is shown as function of the aspect ratio for a solenoidal coil with a single layer and a height of $10cm$.

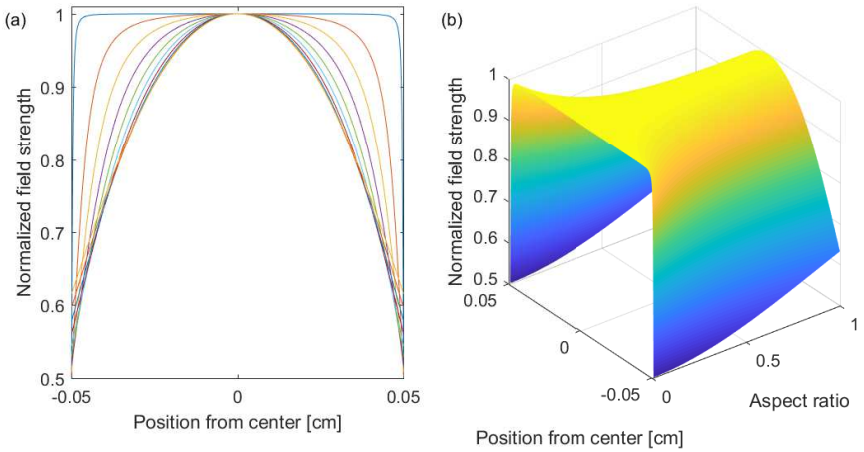

Figure 2.7: Normalized magnetic field strength as function of position from the center of the coil for various coil aspect ratios. a): Cross sections of the magnetic field strength. The dark blue contour represents an aspect ratio of 2.01 *and in increments of* -0.1 *down to an aspect ratio of* 0.01. *b): Surface plot of magnetic field strength.*

The infinitely long coil has inductance, L, equal to

$$L = \frac{\mu_0 N_c^2 N_l^2 A_c}{H_c}, \tag{2.8}$$

where A_c is the CSA of coil equal to $\pi D_c^2/4$. Inductance of the infinitely long solenoid is overestimated when a multi layered finite length coil is used. Wheeler [56] introduced empirical formulas for multi-layered coils that accounts for the finite length of the coil up to second order terms and is equal to:

$$L = 31.6 \times 10^{-6}\frac{\left(\frac{D_c + N_c d_w}{2}\right)^2 N_c^2 N_l^2}{3D_c + 9H_c + 10N_c d_w}. \tag{2.9}$$

2.7 Polarization Coil

In an EFNMR experiment, signal level and SNR are increased by a polarization coil, increasing magnetization of the sample. Besides physical sample size, we can thus increase induced EMF, by maximizing polarizing field strength, B_p.

To fit the maximum sample volume inside the polarization and sample coil, the sample will be cylindrical. As we have seen in section 2.6, diameter and height of the polarization coil both influence absolute magnetic field strength as well as homogeneity of the magnetic field, depending on aspect ratio. Since at this point we do not yet know what the required sample size will be, this section will optimize the polarization coil while assuming that the diameter and height of the coil are fixed. This implies, we will study the influence of other parameters such as wire thickness and number of layers on the coil, on the coil's properties. However, actual specifications of the coil will not be given.[1]

Inspecting equation 2.5, we observe that magnetic field strength, $\vec{B}_p$, can be optimized by choosing a maximum ratio of N_c/H_c, while keeping current constant. This would mean that to do this, we should minimize wire thickness. However, it is much easier, efficient and cheaper to power the polarization coil from a constant Direct Current (DC) voltage source than from a constant current source. Therefore, we would like to express magnetic field strength in terms of voltage, U, instead of in current, I.

Ohm's law relates current, I, to the resistance of the solenoidal coil, R, and the voltage across it, U. Converting current to voltage and substituting into equation 2.7, we find for the axial component of polarizing magnetic field, B_p, on axis of the solenoid:

$$B_p(x) = \frac{\mu_0}{8\rho_e}\frac{H_c}{D_c N_c^2}\, U \left(\frac{x - x_1}{\sqrt{(x-x_1)^2 + R^2}} - \frac{x - x_2}{\sqrt{(x-x_2)^2 + R^2}} \right) . \tag{2.10}$$

Minimizing wire thickness reduces current at constant voltage, due to increasing resistance. We now see that magnetic field strength scales with $\frac{H_c}{N_c^2}$ and instead of selecting thin wire, we should maximize wire thickness. However, there is a practical upper limit to the maximum wire thickness.

Both the DC voltage source, consisting of a power supply and P-channel MOSFET, and connecting cable, have a non-zero resistance. Together, their resistance, R_{out} forms a voltage divider with the coil's resistance and thus a voltage drop is present across them. The potential across the coil, V_{coil}, equals

$$V_{coil} = V_{DD}\frac{R}{R + R_{out}} , \tag{2.11}$$

where V_{DD} is the voltage across both the source and coil. At large wire thicknesses where the coil's resistance becomes low, V_{coil} drops. This decreases overall conversion efficiency of current to magnetic field. Moreover, increasing wire diameter leads to increased current and power, which also heat up both the source and coil causing the current to decrease over time.[2] This is contradiction with the requirements since we want magnetic field strength and thus polarization current, to be as stable as possible.[3]. Finally, increasing wire diameter increases absorbed power faster than magnetic field strength. Therefore, conversion efficiency

[1] Specifying polarization coil properties without considering the sample coil is not very useful. This is because both the sample and sample coil must fit inside the polarization coil, and signal level and SNR have not yet been analyzed.

is always higher for thin wire than for thicker wire.

For a coil with an inner diameter of $12cm$ and height of $14cm$, various coil properties as function of the wire CSA for a coil with one, two and three layers are calculated. Both the number of turns, coil resistance in Ω, current in I, as well as the mean coaxial magnetic field strength on the axis coil's axis in mT and conversion efficiency in mT/W are shown in figure 2.8. Output impedance of the voltage source and cable is assumed to be 0.2Ω at $12V$.[4]

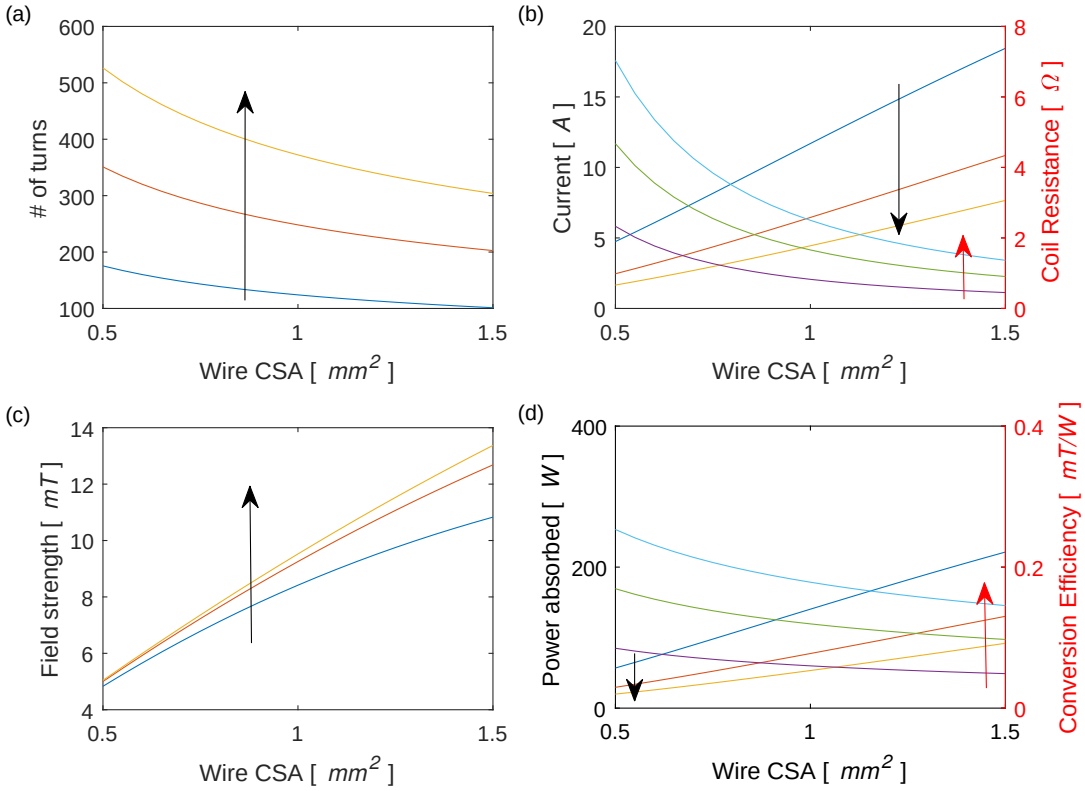

Figure 2.8: Several properties of a coil with height of $12cm$ *as function of CSA in* mm^2*. (a): number of turns* N_c *(b): Current,* I*, in Ampere and coil resistance in* Ω*. (c): Mean coaxial component of magnetic field strength on axis of the coil. (d): Power absorbed in* W *and conversion efficiency in* mT *per* W*.*
Along the direction of the arrows in all graphs, the number of layers on the coil, N_l *increases from one to 3.*

When CSA is increased for constant coil geometry, the number of turns decreases. With decreasing number of turns, coil resistance decreases which increases polarization current. The magnetic field strength also increases, but shows a negative second derivative due to the decrease in effective voltage across the coil for higher CSA and thus lower resistance. With

[2]Since the solenoid is a resistor while polarization current is enabled, it generates heat. When the coil heats up, its resistance will increase, decreasing current through it if voltage across it is constant. Since polarization current directly influences magnetization and thereby NMR signal amplitude, temperature changes must be minimized or corrected for. Corrections can be made by measuring the coil current and scaling the NMR signal accordingly.

[3]Minimization of temperature influences can be done actively or passively by design. Active corrections include all forms of cooling the coil to keep the temperature stable. They increase setup complexity as well as size and cost. Passive correction is only feasible by minimizing the power dissipation in the coil and optimizing thermal behavior.

[4]Typical $R_{DS,on}$ of a p-channel MOSFET is between 0.05 and 1Ω. Multiple devices can be placed in parallel, decreasing effective $R_{DS,on}$ of the entire switch to an arbitrary small value, however an average value of 0.2Ω is realistic.

increasing wire CSA the power absorbed is increased while the conversion efficiency drops due to the effective voltage divider.

Besides inspecting the polarization coil properties for a given number of layers, we can also look at the influence of the number of layers on the properties, whilst still keeping coil dimensions equal. As can be seen, magnetic field strength (figure 2.8(c)) does not depend strongly on the number of layers. This is what we expect since the number of layers is not present in equation 2.7. The only effect it has on the total magnetic field, is that more layers result in a more linear relationship between magnetic field and CSA. This is due to the coil being a more efficient voltage divider with the voltage source and cable at high CSA when multiple layers are used.

Inspecting conversion efficiency (figure 2.8(d)) shows that the power needed to obtain maximum magnetic field strength for constant CSA, is lowered for increasing number of layers. Of course, increasing the number of layers on the coil also increases weight and cost of the coil.

Another aspect to consider is switching off of current in the coil after a polarization cycle. This will be done using p-channel MOSFETs in a high side switch configuration. The MOSFET's maximum drain-source voltage rating, V_{DS}, must not be exceeded to avoid failure. Typically, this value is around $100V$. For a non-adiabatic experiment, the maximum time in which current must be reduced to zero should be less than half a period at Larmor frequency.

An inductive coil generates a back EMF when the magnetic field inside it suddenly changes, in an attempt to keep the magnetic field constant. Back EMF is equal to $emf = -L\frac{dI}{dt}$ where L is the coil's inductance according equation 2.9 and I the polarization current. Both inductance and back EMF are shown in figure 2.9, for a coil with same geometry as before, as function of wire CSA. As can be seen for increasing CSA, inductance (figure 2.9(a))

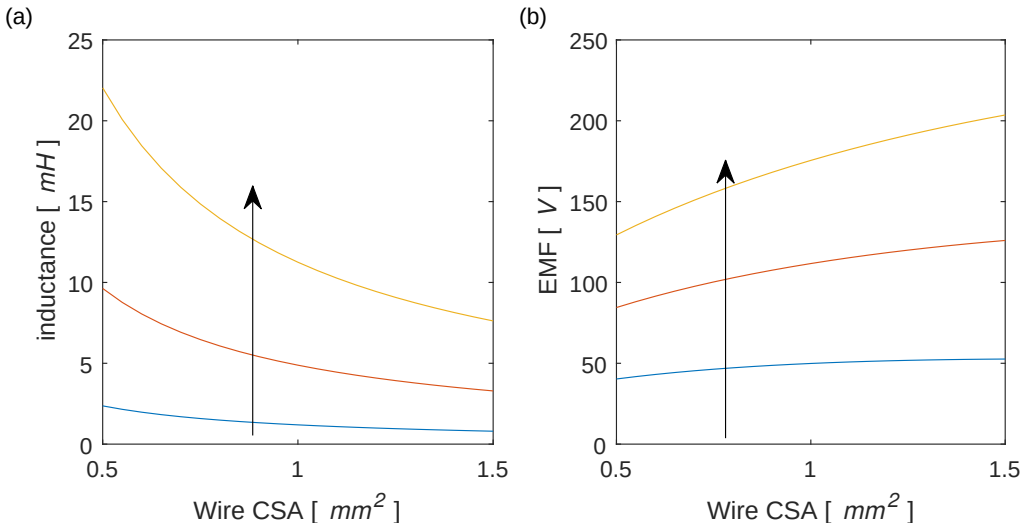

Figure 2.9: (a): Polarization coil inductance in mH as function of wire CSA in mm^2. (b): EMF induced upon switching current in the coil on or off, as function of wire CSA in mm^2.
Along the direction of the arrow in both graphs, the number of layers on the coil, N_l, increases from one to 3.

decreases. However, wire diameter decreases and the current increases for constant voltage. Therefore, back-EMF upon switching increases for increasing CSA as can be seen in figure 2.9(b). Switching time used to produce this plot is $0.2mS$.[5]

[5] In section 3.1 we will look at the amplitude of earth's magnetic field. However, for now, assume that the maximum Larmor frequency will be roughly $2500Hz$.

If current is to be switched off adiabatically, it must be switched off on an order of magnitude bigger than the time of a single-phase cycle at the Larmor frequency (see section 2.2). This can be achieved by switching a capacitor in parallel with the coil during switching off, of the current. In the series Resistive inductive (L) Capacitive circuit (RLC) circuit, current decays as a transient governed by

$$I(t) = A_1 e^{s_1 t} + A_2 e^{s_2 t} \ , \tag{2.12}$$

where s_1 and s_2 are the roots of the characteristic equation $s^2 + 2\alpha s + w_0^2$ and A_1 and A_2 are parameters set by the boundary conditions of the system during transients. Solutions of s_1 and s_2 to the characteristic equation are

$$s_1 = -\alpha + \sqrt{\alpha^2 - \omega_0^2}, \quad s_2 = -\alpha - \sqrt{\alpha^2 - \omega_0^2} \ . \tag{2.13}$$

Parameters α and ω_0 are given by

$$\alpha = \frac{R}{2L}, \quad \omega_0 = \frac{1}{\sqrt{LC}} \ . \tag{2.14}$$

In a critically damped system, the roots s_1 and s_2 are real-valued, resulting in the fastest possible decay time without oscillating. This is the case when the damping factor $\zeta = \frac{\alpha}{\omega_0}$ equals 1. This is when

$$\frac{R}{2}\sqrt{\frac{L}{C}} = 1 \ . \tag{2.15}$$

Inductance of the polarization coil, L, is fixed. Its resistance, R, can however be increased by placing an additional resistor in series with the parallel capacitor to increase damping of the circuit. Tuning of the resistance and capacitance used in the final design of the polarizer was done using electric simulator LTspice. This is because although our model includes the primary elements to be taken into account, it does not model parasitic properties of components such as parasitic capacitances, resistances and inductances. Moreover, using an electrical simulator allows inspection of all circuit properties simultaneously both in a stationary as well as time dependent study.

Chapter 3

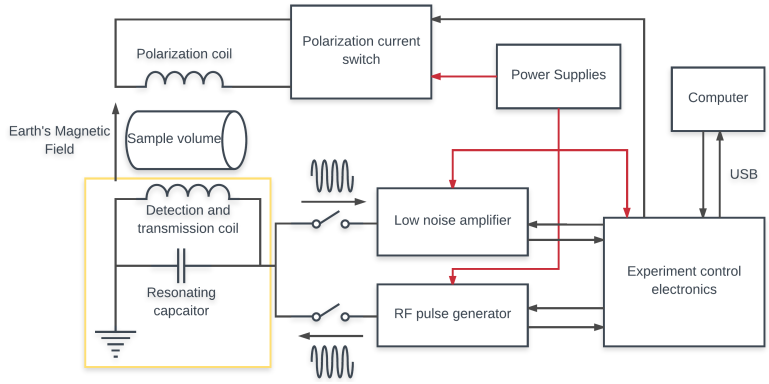

EFNMR Signal and SNR

In chapter 1 we have taken a look at how NMR works. In the previous chapter, chapter 2, we have seen how EFNMR differs from NMR and what that means for SNR. To boost SNR, we have employed the Varian Packard method and have given two different methods of switching current in the polarization coil, adiabatic and non-adiabatic. The remaining parts of an EFNMR setup to discuss are the detection coil, EFNMR signal amplifier and data processing. In this chapter, we will be concerned with the detection coil.

Design of the detection coil is crucial to obtain good SNR. To do so, we will first review earth's magnetic field strength since this directly gives us an estimation of signal level per unit volume. After this has been done, various noise sources in the EFNMR experiment will be analyzed after which the detection coil will be analyzed.

3.1 Earth's Magnetic Field Strength and Signal Amplitude

Larmor frequency, ω_0, of the EFNMR signal as calculated by equation 1.9 requires magnetic field strength as input parameter. Earth's magnetic field strength is conventionally expressed in intensity, B_0, declination, ϕ, and inclination, θ, which are spherical coordinates. The appropriate conversion from spherical to Cartesian coordinates are given in equation 3.1.

$$B\left(x,y,z\right) = B_0\left(cos\left(\theta\right)cos\left(\phi\right), cos\left(\theta\right)sin\left(\phi\right), sin\left(\theta\right)\right) \tag{3.1}$$

In Eindhoven where this work was done, declination and inclination are 1.281° and 66.656°, respectively [17]. A yearly variation exists mainly in declination due to tilt of the geographic rotation axis with respect to the sun. In Eindhoven, main field intensity, B_0, is $48.923\mu T$ resulting in Larmor frequency in pure water of $f = 2083Hz$ when the sample is aligned along the earth's magnetic field vector. However, since earth's magnetic field strength, inclination and declination vary around the globe, the intended frequency range of the setup is $1000 - 2500Hz$ and thus the intended bandwidth $1.5kHz$. A map of earth's magnetic field intensity is shown in figure 3.1

Equation 1.28 provides a theoretical amplitude of EFNMR signal induced in a detection coil. To make the amplitude qualitative, some order of magnitude estimations of the expected voltage level are performed. We assume a sample of water with a volume, V, of $100mL$. Per molecule, water has two NMR active protons. The number of protons, N_p, in this volume is

$$N_p = \frac{2N_A\rho_m V}{M_{mol}} = \frac{26.022140 \times 10^{23} 998.5 \times 10^{-4}}{18.01528 \times 10^{-3}} = 6.676 \times 10^{24} \tag{3.2}$$

where N_A is Avogrado's constant, ρ_m is water's mass density and M_{mol} its molar mass, both in kg/m^3.

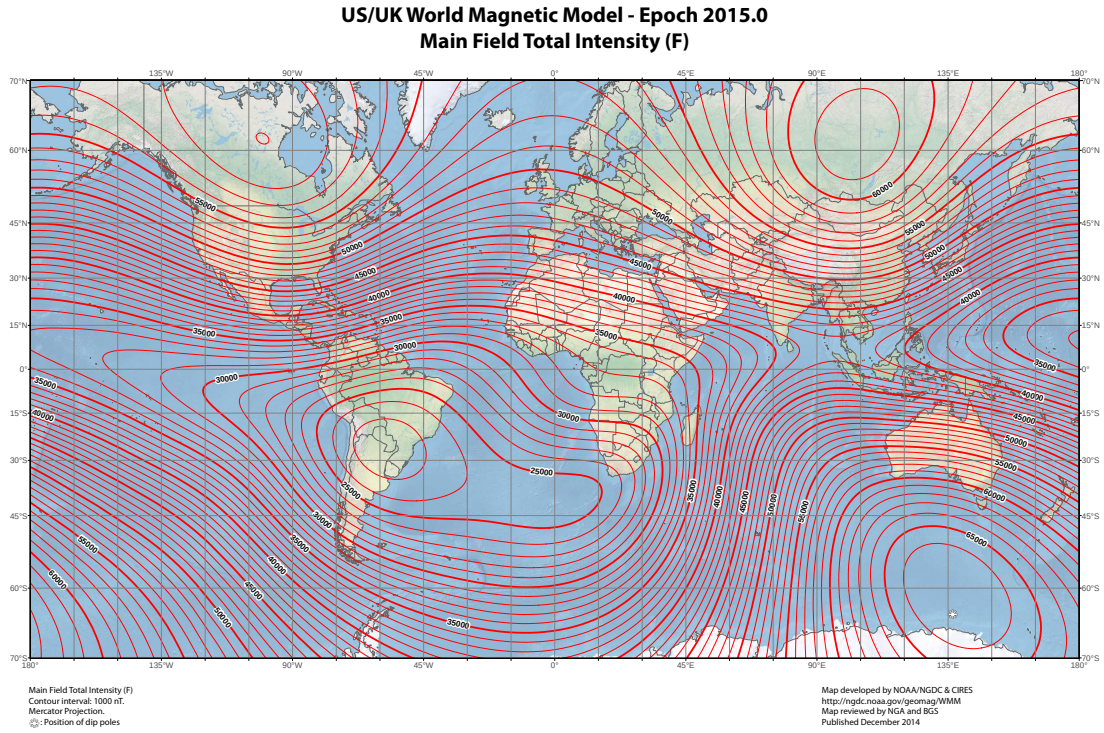

Figure 3.1: Main field intensity isobars of the earth's magnetic field in nanoTesla (nT). [17]

The polarizing field strength, $\vec{B}_p$, is assumed to be of the order of $10mT$. Using Curie's law (equation 1.21) magnetization of $100mL$ of water at room temperature, M_0, equals

$$M_0 = \frac{N_p \gamma^2 \hbar^2}{4 k_b T} B_p \sim \ 8 \times 10^{-11} \left[\frac{A}{m}\right] \tag{3.3}$$

Assuming a sample coil with an order of $N_c = 1000$ windings and Larmor frequency of $2kHz$, amplitude of the EFNMR signal, V_0, equals

$$V_0 = N_c \mu_0 \omega_0 M_0 = 1000 \ \mu_0 \ 2\pi \cdot 2000 \cdot 8 \times 10^{-11} \sim 1 \times 10^{-9} \, [V] \tag{3.4}$$

To maximize the digitization capabilities of the ADC, the measurement signal should be amplified up to full scale digitization level. Typically, this level has a magnitude of $1V$. This means that there are 9 orders of magnitude between the input and desired output signal level. This difference is compensated by an amplifier specifically designed for the EFNMR setup. The amplifier should amplify EFNMR signal in the desired bandwidth to the desired amplitude, with playroom to allow various sample volumes and materials to be measured.

3.2 EFNMR Noise Sources and SNR

In section 1.4 we have derived the SNR for a traditional NMR measurement based on the assumption that noise originates only from Johson noise. From section 3.1 it is known that the EMF induced in a measurement coil with 1000 windings, is of the order of magnitude $10^{-9}V$. At these voltage levels, there are more noise sources than just Johnson-Nyquist noise. These are amplifier current noise, amplifier voltage noise and environmental noise. Although this chapter concerns itself primarily with design of the detection coil, and not with design of the amplifier, using noise contributions from the amplifier while designing the detection coil is crucial for overall setup performance. Therefore, in this section all noise sources will be described and an expression for SNR in EFNMR measurements will be given.

Environmental noise, V_{env}, is EMF induced in the detection coil due to electromagnetic radiation other than that originating from the sample. This noise originates in the frequency range of EFNMR from various sources. A few examples are electromagnetic radiation from power lines harmonics, subharmonics of switched mode power supplies or electromagnetic fields from operating pumps and motors. The amplitude of environmental noise from these sources varies greatly and often these sources also show directional behavior in their radiated noise. Therefore, small changes to the position of the setup in a noisy environment can greatly influence overall noise levels if directional noise sources are present. [1]

Unfortunately, environmental noise cannot be quantized in an equation since it is environment dependent and thus its amplitude is unknown a-priori. Therefore, it will not be included in the equation that defines EFNMR SNR (equation 3.7).

Besides Johnson-Nyquist voltage noise of the coil, the amplifier will also introduce some voltage noise, $V_{n_{amp}}$, due to its internal resistances, independent of coil impedance. Amplitude of this noise depends on amplifier topology, and typical values range from $1 - 20\ nV/\sqrt{Hz}$. Moreover, the amplifier also introduces current noise, sometimes referred to as shot noise. Current noise arises from the discrete nature of electric charge. In semi-conductors, this is mainly due to the presence of potential barriers which discrete charges cross with some statistical deviation, introducing current noise. Especially in transistors found in amplifiers that are constantly biased to conduct, bias current, I_B, always flows in a junction. When passed through an impedance such as the detection coil, current noise becomes a voltage. The amplitude of the current noise, S_n, is equal to [52]

$$S_n = \sqrt{2 I_B q \Delta f} \tag{3.5}$$

where q is the charge of an electron. Current noise amplitude is temperature independent and depends only on bias current, which is a property solely of the amplifier.

To provide an example of the amplitude of various noise sources, in table 3.1 noise levels in $nV/\sqrt{Hz}$ are given for two differential amplifiers and three coil resistances. At each coil resistance, the dominant noise source is highlighted. The AD8428 differential amplifier has a voltage noise of $1.3nV/\sqrt{Hz}$ and current noise of $1.5pA/\sqrt{Hz}$, while the AD8224 differential amplifier has voltage noise of $14nV/\sqrt{Hz}$ and a current noise of $1fA/\sqrt{Hz}$. The AD8224 has extremely low current noise at all resistances listed in table 3.1. However, its voltage noise is the largest contribution to total noise in amplitude at the three lowest resistances. The AD8428 has voltage noise an order of magnitude lower than the AD8224. However, AD8428 current noise is larger than that of the AD8224. For low source impedances, the AD8428 is better suited than the AD8224, while for high source impedances, the AD8224 gives lower

[1] More on this topic will be discussed in section 3.4 and made qualitative with measurements in section 4.4.

Table 3.1: Noise amplitude in $nV/\sqrt{Hz}$ of various noise sources for different coil resistances. Dominant noise source for each coil resistance highlighted.

	Coil Resistance				
Noise Sources	10 Ω	100 Ω	1000 Ω	10k Ω	100k Ω
AD8428 voltage noise	1.3	1.3	1.3	1.3	1.3
AD8428 current noise	0.015	0.15	1.5	15	150
AD8224 voltage noise	14	14	14	14	14
AD8224 current noise	0.00001	Coil Noise	0.001	0.01	0.1
Coil Noise	0.4	1.3	4.1	13	41

overall noise. Choosing an amplifier that combines both low voltage and current noise is essential to maintain good SNR. Therefore, choosing the amplifier should always consider the detection coil's impedance.

In section 1.4, SNR has been defined to be the ratio between induced EMF and Johnson noise. Resistance of the coil however is assumed to be purely resistive. When the coil's impedance is not purely resistive but also has a reactive component such as in an inductor or capacitor, equation 1.29 can be generalized to [52]

$$V_n = \sqrt{4k_B T Re\left(Z\left(f\right)\right)\Delta f}, \tag{3.6}$$

where $Re\left(Z\left(f\right)\right)$ is the real part of the frequency dependent complex impedance of the coil, $Z\left(f\right)$. Combining all noise sources, SNR in an EFNMR experiment is equal to the ratio of EFNMR amplitude, V_0, to total noise, in the detection coil and first amplification stage.

$$SNR = \frac{V_0}{\sqrt{V_n^2 + Re\left(Z\left(f\right)\right)^2 S_n^2 + V_{n_{amp}}^2 + V_{env}^2}} \tag{3.7}$$

3.3 Detection Coil

NMR signal detection is done with a solenoidal coil. The solenoidal geometry is chosen for its simplicity, axial symmetry and well defined geometric sensitivity, β. The main design goals for the detection coil, are maximum NMR signal level combined with minimum noise and thus maximum SNR. These goals can not always be achieved simultaneously, and therefore the design should be optimized considering all coil parameters. As an example, consider induced EMF with amplitude V_0, and the coil's thermal noise, with amplitude V_n. For given coil geometry, decreasing wire diameter increases the maximum number of turns that fit on the coil, increasing the signal level. However, decreasing wire size also increases the resistance, R, and thereby increases thermal noise which decreases SNR.

Optimizing sensor design, requires quantitative amplitude estimations of both induced EMF and noise. Due to the limited analytical applicability of voltage and current noise of the amplifier, as well as environmental noise, only thermal noise will be analytically analyzed in this section as function of coil parameters. However, for the final design of the detection coil, amplifier noise (both voltage and current noise) are included in all calculations.

Generalized SNR in an EFNMR experiment as given by equation 3.7, considering only thermal noise and expressed in coil parameters, reduces to

$$SNR = \frac{N_c N_l \mu_0 \omega \ \frac{N\gamma^2\hbar^2}{4k_B T} B_p}{\sqrt{4k_B T R \Delta f}} \ . \tag{3.8}$$

Rewriting this equation to separate constants from coil parameters and polarizing field strength, B_p, gives

$$SNR = \frac{\mu_0 \omega \pi \ N\gamma^2\hbar^2}{4\sqrt{k_B^3 T^3 \Delta\omega}} \frac{N_c N_l}{\sqrt{R}} B_p \ . \tag{3.9}$$

We see that apart from natural constants, SNR scales linear with magnetic field strength, $\vec{B}_p$, but also with coil parameters N_c, resistance R and signal bandwidth $\Delta\omega$. Entering the coil's resistance (equation 2.4) into the SNR, we find

$$SNR = \frac{\mu_0 \omega \pi \ N\gamma^2\hbar^2}{8\sqrt{\rho_e k_B^3 T^3 \Delta\omega}} \frac{H_c \sqrt{N_l}}{\sqrt{D_c N_c}} B_p \ . \tag{3.10}$$

For constant coil height, H_c , and diameter, D_c, SNR scales with $\sqrt{N_l/N_c}$. If the coil's resistance is included into the SNR, we can see that increasing N_c, by decreasing wire size, d_w, increases noise level faster than NMR signal level. To illustrate this, in figure 3.2, the number of layers on the coil, its resistance, induced EMF and resulting SNR due to thermal noise, are displayed as function of the wire CSA. These graphs are made for a single solenoidal coil containing a sample of $100mL$ of pure water, homogeneously polarized at $B_p = 10mT$. This coil has an inner diameter of $5cm$ and height of $12cm$. Furthermore, it is assumed that the signal is filtered with a bandwidth of $1.5kHz$ as specified in section 3.1. The AD8428 is selected to produce these plots since the coil resistances are in the region where this amplifier produces the lowest overall noise levels (see table 3.1).

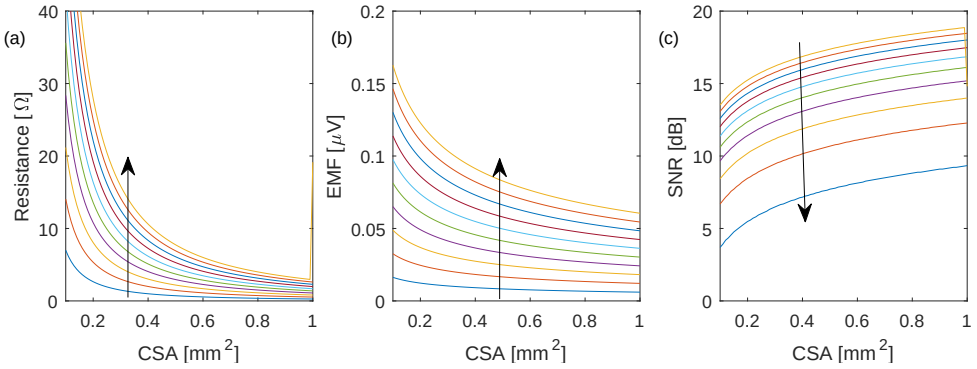

Figure 3.2: Detection coil resistance(a), induced EMF in the detection coil(b) and resulting SNR (c) for a solenoidal coil as function of CSA. With the direction of the arrows in all graphs, the number of layers on the coil, N_l increases from one to 10.

As can also be seen from figure 3.2, it is advantageous to split the total length of wire on a coil into multiple layers, instead of using a single layered coil since winding the coil in N_l layers, increases SNR by $\sqrt{N_l}$.

Making the coil resonant

So far the coil has been considered a simple resistance, while in reality it has a complex impedance consisting of a resistive, inductive and capacitive part. At frequencies where EFNMR will be measured, the coil will be mainly resistive and inductive. Since the coil is inductive, with inductance $L = L_c$, a capacitor with capacitance C, can be connected in parallel with the coil forming a series-parallel RLC circuit as illustrated in figure 3.3.

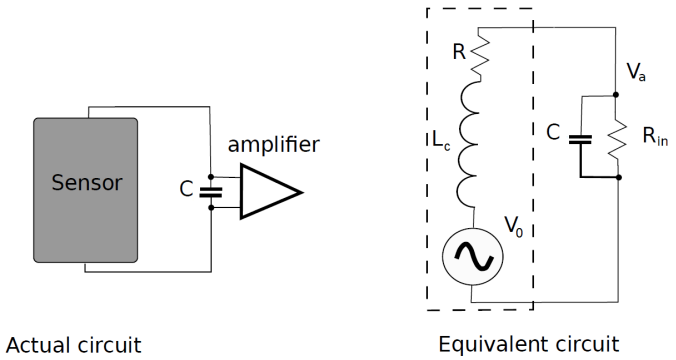

Figure 3.3: Series-parallel RLC circuit. EMF with amplitude V_0, is generated across the detection coil with resistance, R, and inductance, L_c. The capacitor with capacitance C is inserted in parallel to the coil [25].

In this parallel RLC circuit, voltage across the capacitor, V_A, is Q times higher than the voltage across the coil, V_0, if the system is at resonance.

$$V_A = QV_0 \tag{3.11}$$

where Q is the quality factor of the RLC circuit. If the RLC circuit' resonance frequency coincides with Larmor frequency, the measurement signal can be increased in level Q times, selectively around Larmor frequency, lowering the required amplification factor of the amplifier. Although both Johnson, current and environmental noise are all amplified Q times, amplifier voltage noise is not, thereby increasing SNR. Moreover, due to the selective amplification around the resonance frequency, the effective noise bandwidth, Δf, is reduced for

Johnson, current and environmental noise. To determine both resonance frequency and Q factor of the circuit as well as capacitance required, the circuit has to be analyzed using complex impedances.

An inductor has complex impedance $Z_L = J\omega L_c$, with L_c the coil's inductance in Henry and j the complex number. A capacitor has complex impedance $Z_c = \frac{-j}{\omega C}$, where C is the capacitance in Farad. The total impedance, Z_{total}, of the series-parallel RLC circuit in figure 3.3 is

$$Z_{total} = (R + Z_L)\ (Z_C R_{in})\ , \tag{3.12}$$

where R_{in} is the input impedance of the amplifier. Typically, $R_{in} \gg |Z_C|$ and R_{in} can be neglected. The magnitude of the total impedance, $|Z(\omega)|$, as function of frequency is

$$|Z(\omega)| = \sqrt{\frac{R^2 + \omega^2 L_c^2}{(1 - \omega^2 L_c C)^2 + \omega^2 C^2 R^2}}\ . \tag{3.13}$$

The impedance's phase, ϕ, equals

$$\phi(\omega) = tan^{-1}\left(\frac{\omega\left[L_c\left(1 - \omega^2 L_c C\right) - CR^2\right]}{R}\right)\ . \tag{3.14}$$

At resonance, imaginary components of the inductor's and capacitor's impedances cancel, producing a phase angle of zero. This is where the numerator of the arctangent argument equals zero.

$$L_c - \omega^2 L_c^2 C - CR^2 = 0 \tag{3.15}$$

Solving for ω, we find that in a series-parallel RLC circuit the resonance frequency, ω_0, is

$$\omega_0 = \sqrt{\frac{1}{L_c C} - \frac{R^2}{L_C^2}}\ . \tag{3.16}$$

Since the resonance frequency is matched to Larmor frequency, ω_0, capacitance required is directly related to the fixed inductance of the coil. Rewriting equation 3.16, we find the required capacitance to be

$$C = \frac{L_c}{\omega^2 L_c^2 + R^2}\ . \tag{3.17}$$

The quality factor, Q, of the series-parallel circuit is equal to [30]

$$Q = \frac{\omega_0 L_c}{R}\ . \tag{3.18}$$

In addition, the quality factor can be related to spectral bandwidth, $\Delta\omega$, through

$$\Delta\omega = \frac{\omega_0}{Q}\ . \tag{3.19}$$

Incorporating equation 2.9 for inductance, assuming an infinitely long coil, into the quality factor and expressing the resistance in coil parameters gives

$$Q = \omega_0 \frac{\pi\mu_0}{16\rho_e}\ \frac{N_l D_c H_c}{N_c}\ . \tag{3.20}$$

If SNR is again evaluated, considering only thermal noise, but now with Q factor substituted into it, we get

$$SNR = \frac{\pi^2 \mu_0^2 \omega_0^2\ N\gamma^2\hbar^2}{128\sqrt{\rho_e^3 k_B^3 T^3 \Delta\omega}}\ \frac{H_c^2\sqrt{D_c N_l^3}}{\sqrt{N_c^3}} B_p\ . \tag{3.21}$$

Where it must be noted that $\Delta\omega$ is now equal to the bandwidth as calculated by equation 3.19, instead of the specified amplifier bandwidth of $1.5kHz$. We see that SNR scales with $\sqrt{N_l/N_c}^3$, instead of $\sqrt{N_l/N_c}$, increasing the importance of optimizing wire thickness even more. Including the Q-factor of the coil into the SNR is thus essential. Note again, that a coil with few but very thick windings may give good SNR considering thermal noise but will also not generate much signal. It is thus a fine balance between minimizing the thermal noise while maximizing signal level.

Further improvements to the detection coil model

The above model contains two first order simplifications, which must be corrected to get a reasonable resemblance of the real coil to the theoretical model. Firstly, the expected Q-factor of a resonant circuit assumes a lossless coil with resistance equal to its DC resistance. Secondly, the inductance used to determined the quality factor, Q, assumes an infinitely long coil, which is typically not the case for a multi layered EFNMR detection coil.

Due to Alternating Current (AC) power losses, the effective resistance of the coil increases. In general, AC power losses in the coil are due to skin effect (see section A.2) and proximity effect [57]. For a multi-layered coil wound from round, solid wire, the ratio of AC to DC resistance $F_{R(solid)}$ is equal to [42]

$$F_{R(solid)} = \frac{R_{solid}}{R_{dc(solid)}} = A\left[\frac{sinh\,(2A) + sin\,(2A)}{cosh\,(2A) - cos\,(2A)} + \frac{2\left(N_l^2 - 1\right)}{3}\frac{sinh\,(A) - sin\,(A)}{cosh\,(A) + cos\,(A)}\right], \tag{3.22}$$

where A is a parameter given by

$$A = \left(\frac{\pi}{4}\right)^{3/4}\frac{d_w}{\delta}\sqrt{\eta}\,, \tag{3.23}$$

where d_w is the diameter of the solid wire, δ the skin depth of the material (see equation A.15) and η the ratio of wire diameter to average distance between two adjacent windings. As can be seen, increasing number of layers increases the AC resistance of the coil. Especially for multi-layered coils, importance of correcting for AC resistance increases for multi-layered coils. In low frequency limit where EFNMR operates, skin effect does not contribute significantly to overall AC resistance, and only the proximity effect plays a role in the determination of the AC resistance. In this limit, equation 3.22 can be reduced to Dowell's equation [49] as

$$F_{R(solid)} = \frac{R_{solid}}{R_{dc(solid)}} = 1 + \frac{5N_l^2 - 1}{45}A^4\,. \tag{3.24}$$

At $2kHz$, roughly the operating frequency of EFNMR, parameter A for a solid wire with $\eta = 0.9$ is equal to 0.65 if its CSA of $1.0mm^2$, and equal to 0.43 for CSA of $0.5mm^2$.

Total SNR, including effects of AC-resistance becomes

$$SNR = \frac{\pi^2\mu_0^2\omega_0^2\ N\gamma^{22}}{128\sqrt{\rho_e^3 k_b^3 T^3 \Delta\omega}}\frac{F_{R(solid)}H_c^2\sqrt{D_c N_l^3}}{\sqrt{N_c^3}}B_p \tag{3.25}$$

Total SNR also needs to be corrected for inductance of the infinitely long solenoid, which is not realistic for coils other than those with high aspect ratio. Instead, equation 2.9 can be used for the inductance. If the same coil geometry as used to generate figure 3.2 is again used but now with quality factor, AC-resistance and corrected inductance integrated into it, we get the coil properties as displayed in figure 3.4 for the same sample volume of $100mL$.

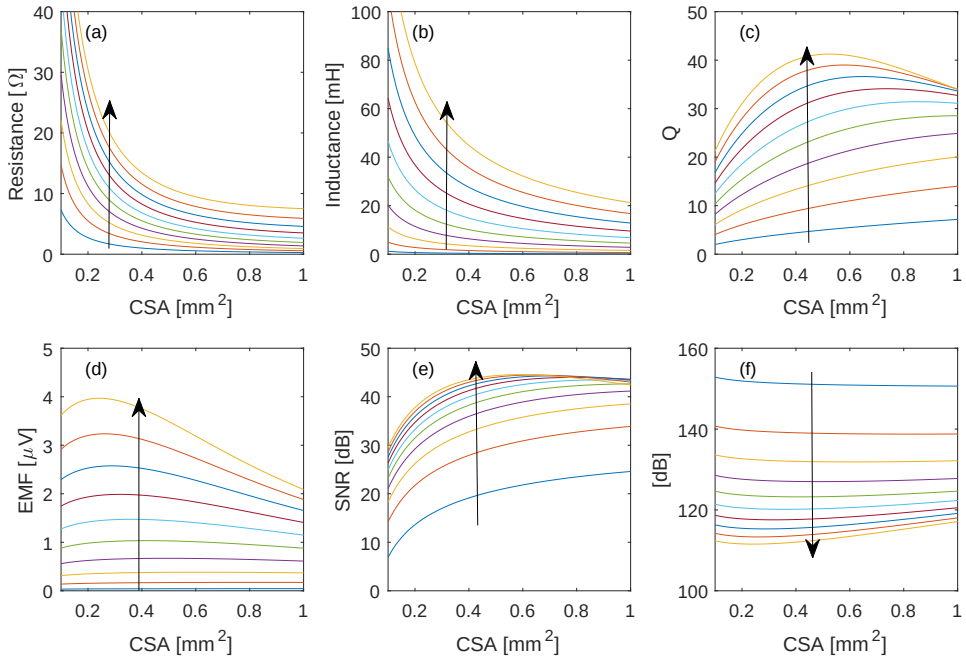

Figure 3.4: Detection coil properties as function of CSA displayed for multiple number of layers, N_c. (a): Coil AC resistance at $2kHz$. (b): Inductance in mH. (c): Quality factor. (d): Induced EMF in μV for a sample volume of $100mL$. (e): SNR in dB for a sample volume of $100mL$. (f): Required amplification factor in dB to amplify EMF shown in (d) to $1V$.
With the direction of the arrows in all graphs, the number of layers on the coil, N_l increases from one to 10.

Inspecting figure 3.4, several observations can be made. First, Q factor of the coil decreases for high CSA when a multi-layer coil is used. This is mainly due to AC losses which are highest for a coil with thick wire and many layers. SNR shows a similar trend, and for a coil with CSA $= 1.0mm^2$, there is virtually no increase in SNR when going from a five, to a 10 layer coil. Despite this lack of SNR increase, absolute EMF still rises and when environmental noise is considered in SNR, more layers still result in better SNR. For low CSA, inductance and resistance quickly rise while SNR degrades. EMF rises too, but slower than inductance and resistance.

Comparing EMF with Q factor included in figure 3.4 (d), to that without Q factor included, shown in figure 3.2 (b), not only shows that EMF is higher for all coils, but also that no longer it is maximum for a coil with minimum wire thickness. SNR thus not only degrades because of increased resistance for coils with thin wire, but also due to decreased EMF when the coil is made resonant.

One final note must be stipulated again. All plots displayed in this section do not include any noise contributions from environmental noise. This is because its amplitude cannot be known a-priori and therefore it does not make sense to try to express it in equation form. The topic of environmental noise is discussed separately in A.2, 3.4 and 4.3.

3.4 Reducing Environmental Noise

Environmental noise is a factor in the total noise of EFNMR measurement which has an amplitude that cannot be known a-priori. However, from all the noise contributions, it is the only one that can be minimized without affecting the measurement itself. This is because the noise is induced from external sources. Two methods of reducing environmental noise exist, the use of a bucking coil [47, 53], or shielding the sample coil.

A bucking coil works by connecting a secondary measurement coil in series but with opposite polarity, relative to the primary measurement coil. The measurement signal should only be picked up the primary coil, while environmental noise is picked up by both coils and canceled. Thereby, the noise can be significantly reduced, increasing SNR. Graphically, the principle of a bucking coil is shown in figure 3.5.

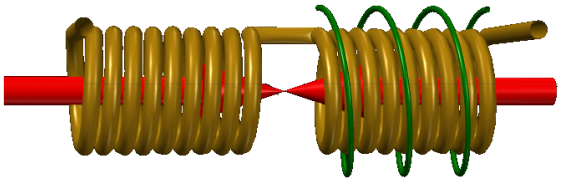

Figure 3.5: Bucking coil principle illustrated. Two coils are connected in series with opposite polarity. In red, EMF induced due to environmental noise with opposite polarity. In green, EMF induced due to the sample present in only one of the coils.

To make environmental noise completely cancel, the induced EMF due to it should be equal in both coils. Inspecting equation 1.28, shows this is possible if the product of N and $\frac{d\phi}{dt}$ is constant. Since magnetic flux, ϕ, and its rate of change are dictated solely by the cross sectional area of the coil, A, the product $N \cdot A$ thus has to be equal for both coils. Three different basic bucking coil configurations exist, each with their own advantages and disadvantages.

In the first configuration, two identical coils are aligned side by side with their axis parallel. Graphically, this is shown in figure 3.6. The assembly of two coils is positioned inside the polarizing coil. The main advantage of this setup is that when the magnetic field inside the polarization coil collapses, ring-down behavior of both sample coils will be in opposite phase, reducing receiver dead-time (see Appendix D). A disadvantage of this setup is that amplitude of the polarizing field is relatively low due to both coils needing to fit inside the polarization coil.

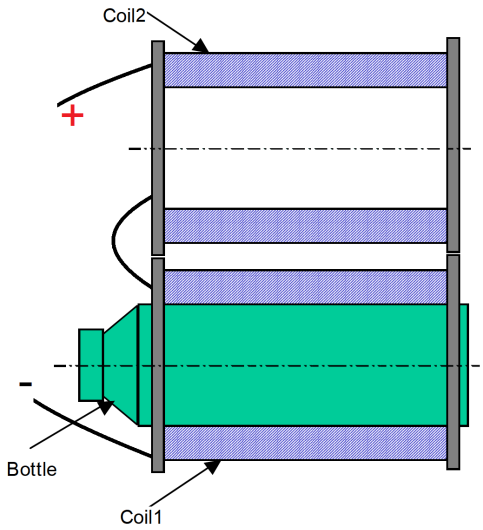

Figure 3.6: Bucking coil configuration of two idential coils aligned side by side.

A second bucking coil arrangement can be thought of having a secondary coil, identical to the primary coil, aligned coaxially with the primary measurement coil yet spatially separated from the primary coil. This configuration is shown in figure 3.7. Using this configuration, the advantage of reduced receiver dead-time is lost. However, magnetic polarization field strength is increased due to a smaller polarization coil. A disadvantage of this setup is that the two coils need to be placed sufficiently far apart such that the NMR magnetic dipole field is coupled only to the primary measurement coil resulting in a larger assembly than for the side by side arrangement.

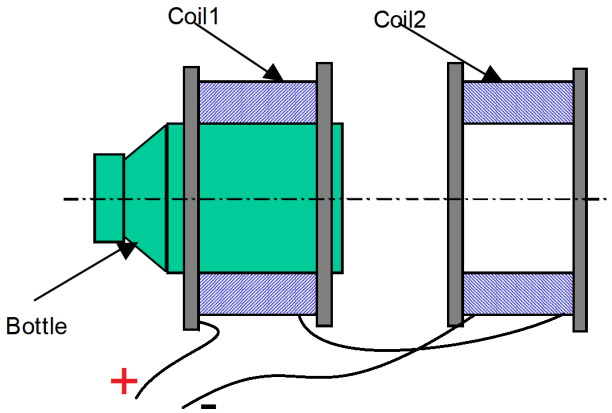

Figure 3.7: Bucking coil configuration of two identical coils aligned coaxially.

A third and last configuration uses two different coils. The primary measurement coil is placed inside the polarization coil, while a secondary coil of larger radius is placed coaxially around the outside of the polarization coil. The secondary coil must have an equal product of number of turns and area as the primary coil to keep induced EMF due to environmental noise equal. This configuration has a stronger disadvantage with respect to the second configuration in the reduction of receiver dead-time; Magnetic field lines outside the polarization coil run in opposite direction compared to inside the polarization coil. Since the two coils of the bucking coil are connected in opposite phase, ring-down behavior will become common mode for both coils which in turn only increases dead-time instead of increasing it. An illustration of the third configuration is shown in figure 3.8.

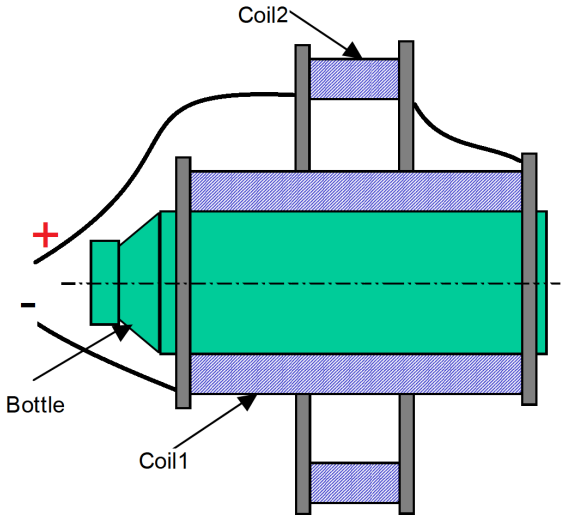

Figure 3.8: Bucking coil configuration of two identical coils aligned coaxially.

Some practical issues limit noise reducing capabilities of a bucking coil setup. Firstly, connecting a secondary coil in series with the primary coil reduces environmental noise, but also doubles both thermal and amplifier current noise. This is because thermal and current noise are caused by random thermal fluctuations which are uncorrelated between the two coils and therefore they do not cancel. To illustrate the effects of doubled voltage and current noise with regards to SNR, the same graphs as displayed in figure 3.4 for a single solenoidal coil are repeated for two solenoidal coils wired in series, are displayed in figure 3.9.

Moreover, the assumption of two identical coils is one which is easily made theoretically but not in practice. Winding two coils perfectly identical in resistance, inductance and overall size is virtually impossible using conventional production methods if alone by small variations in the wire diameter. Finally, the theoretical assumption of perfect cancellation is only valid if the field inside the two coils is equal. In general, this is the case for frequencies where EFNMR works since the wavelengths of the electromagnetic radiation surrounding the coil are significantly bigger than the dimension of the coils. However, in office environments sources of environmental noise are typically in the near field of the pickup coils and show directional behavior. Since the magnetic field of a dipole, which is usually the case for unshielded air wound inductors used in electrical equipment, as well as closely spaced electrical wiring, drops as $1/r^3$, sources close to the pickup coils can induce different magnetic field strengths on both coils. When this is the case, magnetic field cancellation will also show an angular dependency when the source is not oriented along the axis of the two solenoids. This effect is least noticeable for the configuration where two identical coils are placed side by side, and most noticeable for two coaxially aligned identical coils placed a distance apart.

Besides using a bucking coil, the entire assembly can also be placed inside a non-magnetic, conducting metallic box shielding the sample coil from external electromagnetic radiation (see A.2). Skin depth (see equation A.15) for aluminum $\left(\sigma = 3.5010^{-7}\right)$ and copper $\left(\sigma = 5.69710^{-7}\right)$ at $1kHz$ is 2.7 and 2.1 cm, respectively. This means that external electromagnetic radiation is decreased in intensity by a factor $1/e$ at this thickness. An aluminum or copper conductor of adequate thickness can thus reduce environmental noise.

A cubic box of copper or aluminum would measure roughly $20{\cdot}20{\cdot}30cm$ in size to house the setup while allowing room for connectors. The weight of such a box in aluminium or copper respectively (with thickness equal to skin depth at $1kHz$), would be roughly 60 and 24kg. However, if the bucking coil configuration is used, the on axis noise cancellation prevents the requirement for a box of aluminium and a cylinder around the coils can suffice, reducing

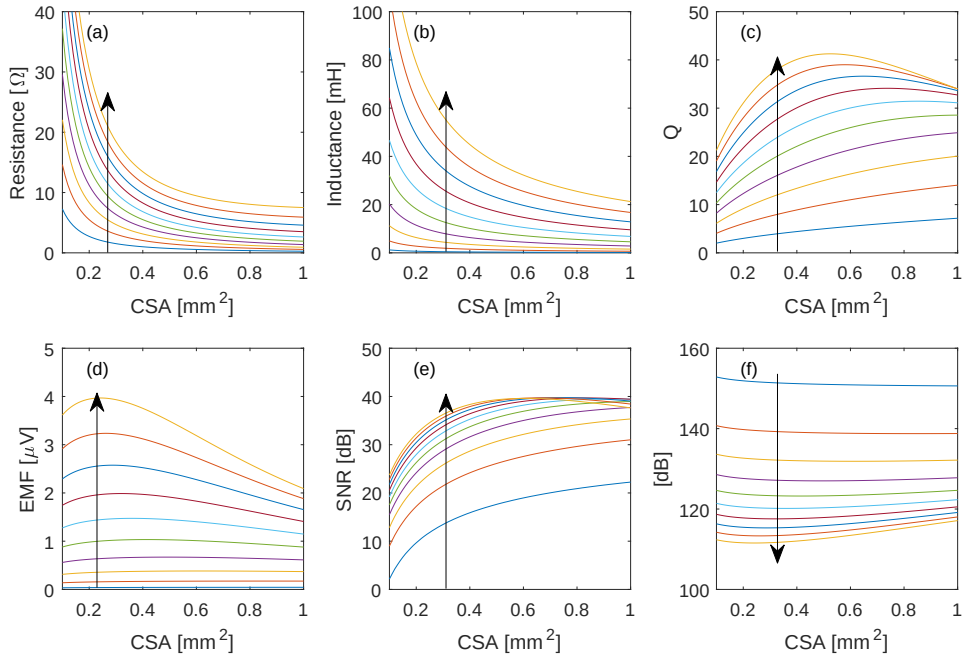

Figure 3.9: Detection coil properties for two solenoidal coils in series as function of the CSA. (a): Coil AC-resistance at $2kHz$ in Ω. (b): Inductance in mH. (c): Quality factor. (d): Induced EMF in μV. (e): SNR in dB. (f): Required amplification factor in dB.
With the direction of the arrows in all graphs, the number of layers on the coil, N_l increases from one to 10.

the weight and cost of the shield. Moreover, using a circular tube is cheaper since there is no additional construction cost associated with construction of the box. Besides practical limitations of the weight in making the setup mobile, also considering current prices of these materials using shielding would make the setup too expensive. For aluminium, such a box would in raw, unprocessed bulk material alone already cost €40, not including the cost of actually constructing the tube or sheet form for the box.[1]

As an alternative to the shielding box, also the polarization coil can be shorted during acquisition. As suggested by Callaghan in his paper on EFNMR [21] this further reduces the environmental noise levels due to shielding of external magnetic fields by skin effect of the copper wire. [2] While the polarization coil may not reach thicknesses sufficient to completely shield the sample coils, any reduction can be helpful and the only change required in the hardware is the addition of a relay.

[1] Completely shielding the EFNMR device is by far the most effective solution when cost nor mobility of the setup is an issue. Retrofitting a shield around the coil assembly is thus always a viable expansion option to improve the setup's performance.

[2] See section A.2.

Chapter 4

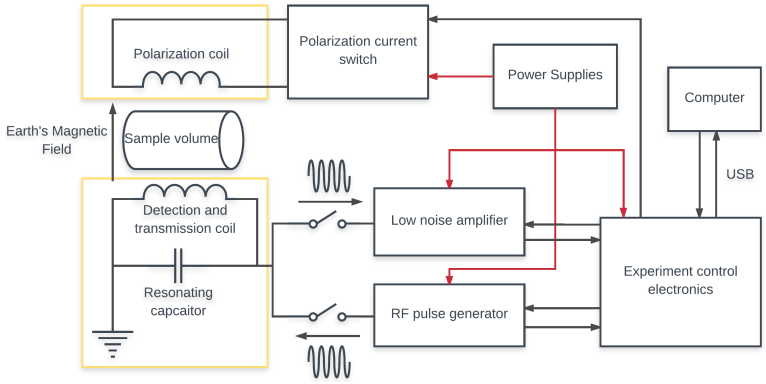

Polarization and detection coil specifications

At this point, we have all the knowledge required to design both polarization and detection coils. Due to the construction of the EFNMR setup where the sample fits inside the sample coil, which is subsequently placed inside the polarization coil, design of polarization and detection coil influence each other. Final design of the polarization and detection coil was done by writing a Matlab script that evaluates all design parameters simultaneously. From this script, the optimum design specifications of both the polarization and detection coil are determined.

In this chapter, we will first specify the design of the polarization coil in section 4.1 and how current is switched using the polarizer in section 4.2. Secondly, we will specify the detection coil and show the entire mechanical assembly of both polarization and detection coils. Finally, we will show the performance of the bucking coils with a few measurements.

4.1 Polarization Coil Specifications

The polarization coil is made from copper wire with a copper diameter of $0.98mm$ giving a CSA of 0.750. Including enamel, the wire has a thickness of $\sim 1.1mm$ such that 127 windings fit per layer. The coil has been wound on an acrylic tubular former with an inner and outer diameter of $125mm$ and $132mm$ respectively. Three layers, each with a winding length of $140mm$ have been wound onto the pipe.

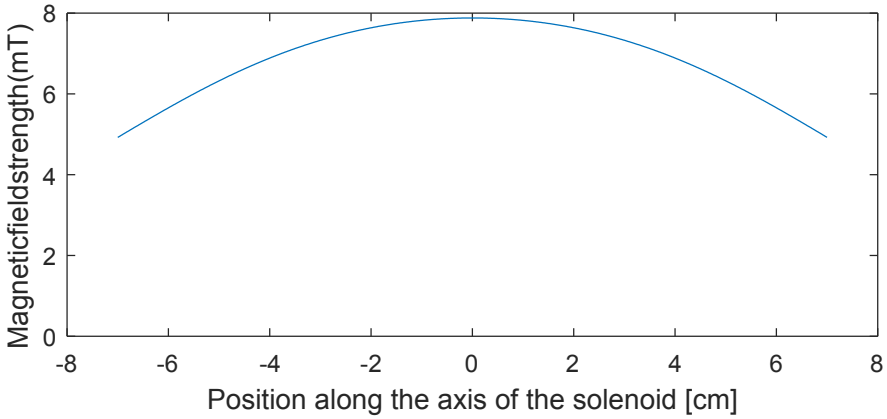

Figure 4.1: Magnetic field strength along the axis of the polarization coil in mT.

For this coil geometry, equation 2.7 gives the coaxial component of magnetic field strength on axis of the polarization coil. This is illustrated in figure 4.1, when the polarization coil

is connected to a voltage source at a potential of $12V$ with an output resistance of 0.2Ω is shown.

As can be seen in figure 4.1, magnetic field strength on axis of the polarization coil varies between $7.9mT$ at the center of the coil, to only $4.9mT$ at its edges. The average magnetic field strength along the axis is $6.9mT$, which is an increase in $\vec{B}_0$ of roughly 140 compared to earth's magnetic field strength.

In table 4.1, calculated and measured coil parameters are displayed. Inductance was measured at $4kHz$[1], using a Hioki 3532-50 RLC tester. This frequency was chosen since it best represents the rate of change in the magnetic field when the current is quenched in a non-adiabatic experiment.

Table 4.1: Coil parameters for the Polarization coil as calculated and measured.

Parameter	Calculated Value	Measured Value
Turns per layer N_c	134	133
Inductance (mH)	13.8	14.0
DC Resistance (Ω)	3.35	3.41
Power absorbed at 12V (W)	40.6	-

4.2 Polarization Current Switch

The polarizer that switches current in the polarization coil has been designed to be a standalone device. The Printed Circuit Board (PCB) onto which it is built consists of several individual sections. There is a polarization current switch section, power supply section, digital isolation interface and finally a gradient driver section, which is currently still in the prototype phase and not described in this report. An overview of the components as laid out on the PCB is shown in figure 4.2. A picture of the polarizer is shown in figure F.3. The

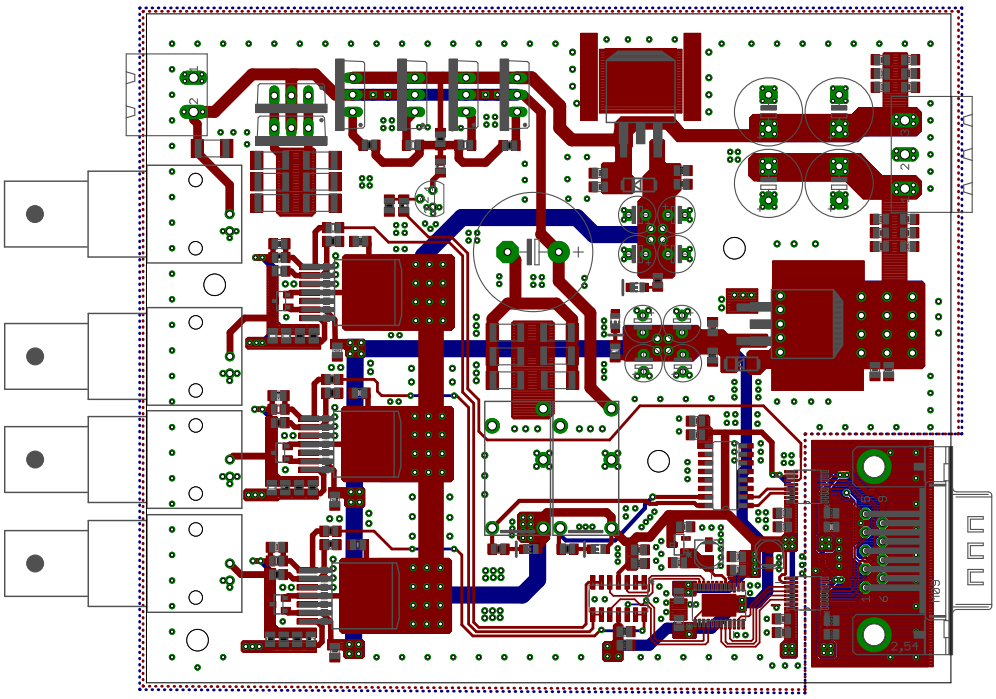

Figure 4.2: Overview of the PCB of the polarizer board.

main section on the polarizer board is the polarization current switch. The basic schematic of this switch is displayed in figure 4.3. It employs four IRF9530 P-channel Hexagonal Field Effect Transistor (HEXFET)s[1] which have a maximum V_{DS} voltage rating of $-100V$ and an on-state resistance, $R_{DS,on}$, of 0.3Ω. Switched in parallel, the total output impedance of the switch, R_{out}, equals 0.07Ω. The HEXFETs are configured in a high side switch configuration directly tied to the positive supply rail V_{cc}, that allows the polarization coil to be always connected at ground potential of the circuit. Gate drive to the HEXFETs is provided by a bipolar NPN 2N3904 transistor in a low side switch configuration. The gates of all four HEXFETs are connected through gate resistors. This limits maximum gate current to the HEXFETs and equalizes switching times of all four devices.

The polarization circuit has to be able to perform both adiabatic and non-adiabatic pulse sequences. For non-adiabatic experiments, current and magnetic field in the polarization coil must be removed on a timescale lower than $0.2ms$, without the polarization coil generating EMF higher than the breakdown voltage of the MOSFETs. To protect the current switch from high back-EMF and allow a path for current to flow when the HEXFETs are turned off, a so-called flyback diode is connected in parallel to the coil, with a damping resistor in series. The value of this high power ($5W$) damping resistor has been selected such that the coil becomes overdamped during the removal of current. Therefore, the behavior of current decay in the circuit during the initial phase of current switching is roughly $3ms$, much slower

[1] A HEXFET is a special variant of a MOSFET designed to optimize performance.

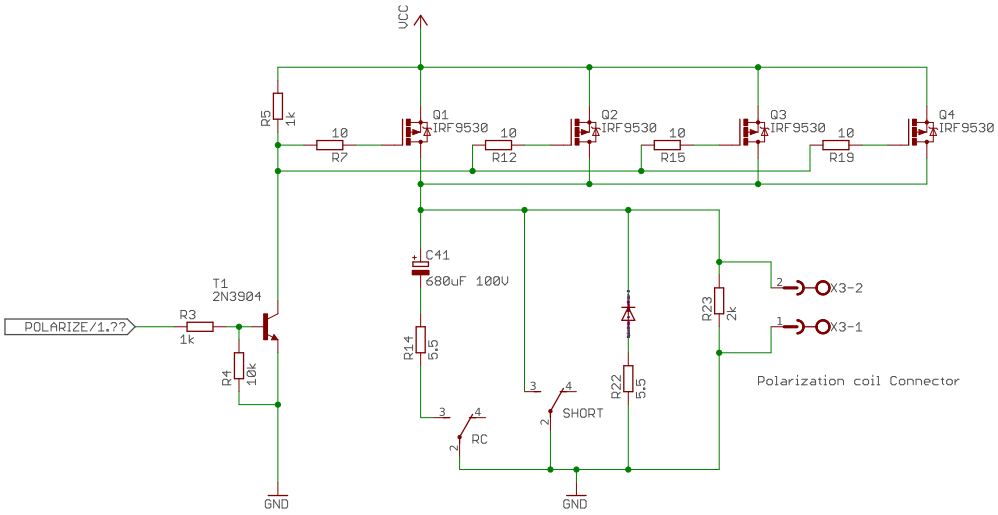

Figure 4.3: Basic schematic of the polarization current switch.

than the required $0.2ms$, and the induced EMF is limited to $-23V$. However, when the voltage across the diode is lower than $0.8V$, it stops conducting. By this time, most of the energy in the magnetic field has dissipated. When the diode cuts off, only the $2k\Omega$ parallel resistors remains, and the system becomes critically damped, reducing the last portion of current and magnetic field as quickly as possible [7, 9]. To see why this transition is still non-adiabatic, consider the following experiment.

During polarization, the total magnetic field vector is composed of the polarization field, $\vec{B}_p$, and earth's magnetic field, $\vec{B}_e$, which are aligned perpendicular to one another. The effective magnetic field vector (see figure 2.1) is aligned almost parallel to the polarizing field vector. When the diode cuts off, there is a current of $280mA$ circulating through the coil. Consequently, the polarizing magnetic field, $\vec{B}_p$, has magnitude roughly ten times bigger ($\approx 0.46mT$) than earth's magnetic field and the resulting magnetic field vector is aligned at an angle of $\approx 5.7°$ relative to the polarizing field vector. Therefore, magnetization in the sample is oriented along this resulting field vector. During the final transition, the remaining magnetic field is removed in $0.03ms$, much smaller than the speed with which magnetization can follow the field vector. Therefore, free precession follows with an amplitude almost equal as it would have been if the entire magnetic field was removed on a timescale smaller than $0.2ms$.

Adiabatic experiments can be performed when a capacitor is switched in parallel to the coil through a relay, such that the system becomes an RC circuit. During a polarization cycle, the capacitor charges to the power supply potential V_{cc}. When the HEXFETs are switched off, the capacitor discharges itself. The resistors in series with the capacitor act to limit the current and voltage spikes through it. The capacitance is chosen such that the total system is over-damped and the current decays in roughly $20ms$, even when the diode cuts off. When this is done, the effective magnetic field inside the polarization coil, which depends linearly on the current through it, decays on a timescale much larger than $0.2ms$, and net magnetization in the sample follows this net direction according to the adiabatic theorem stated in 2.2.

Finally, a relay is switched parallel to the polarization coil such that during measurements, the coil can be shorted. As described in A.2, shorting the polarization coil shields the sample coil from external electromagnetic radiation and increases SNR. Both the shorting relay as well as the RC relay are driven through a ULN2003 darlington transitor array.

4.3 Detection Coils Specifications

The final sample coil design consists of two coils, each wound on an acrylic tube with an inner diameter of $47mm$, outer diameter of $50mm$ and winding height of $12cm$. The copper wire has a diameter of $0.60mm$, which equals $CSA = 0.28mm^2$. The wire is enameled and the total thickness of the wire, d_w, is $0.70mm$ such that a total of $N_c = 171$ windings fit per layer. Eight layers are wound onto each coil, making the total diameter of each coil roughly $61.2mm$.

Key parameters such as inductance and resistance have been calculated and measured, of which the results are shown in table 4.2. Inductance and AC impedance were measured using a Hioki 3532-50 RLC tester at a frequency of $2kHz$. Current noise for both coils using the

Table 4.2: Calculated and measured values of the detection coils.

Parameter	Calculated value	Measured value coil 1	Measured value coil 2	Measured, both coils in series
Turns per Layer N_c	171	170	169	-
Inductance (mH)	38.2	38.69	38.76	80.72
DC Resistance (Ω)	14.83	14.71	14.73	29.44
AC impedance (Ω)	15.90	15.82	15.84	31.66
Johnson noise $\left(\frac{nV}{\sqrt{Hz}}\right)$	0.69	-	-	1.38
Total coil Quality factor at $2kHz$	28.84	-		30.43

Analog Devices AD8428, is negligibly small at 0.048 $nV/\sqrt{Hz}$. Including voltage noise of the amplifier and excluding environmental noise, a theoretical total noise level of 2.92 $nV/\sqrt{Hz}$ exists before the first amplification stage.

Measured inductance and Q factor at $2kHz$, of two coils connected in series, is slightly higher than calculated. In the calculation of inductance for both coils, it is assumed that total inductance of both coils, is equal to that of two coils in series. The increase in inductance, and thereby Q factor, could be due to mutual inductance between the coils.

Resistance of both coils is slightly lower than was calculated. This is because in the calculations an exact equal number of turns per layer, N_c was used. However, due to transitions between layers and imperfect winding, N_c was slightly lower.

The EMF expected, for a homogeneously polarized (at $12V$, using the polarization coil specified in section 4.1), $100mL$ sample of pure water is $2.57\mu V$. This results in an SNR of $47dB$ without considering environmental noise. At this signal level, an amplification factor of $111dB$ is required to amplify the EMF to voltage around $1V$.

Diameter of each sample coil, $61.2mm$, allows the two coils to fit exactly inside the polarization coil (with inner diameter of $125mm$) with a few millimeters of play. A mounting plate was laser cut from acrylic to which the sample coils were glued, fixing the coils in place with respect to each other. A mechanical drawing of the entire assembly is displayed in figure 4.4.

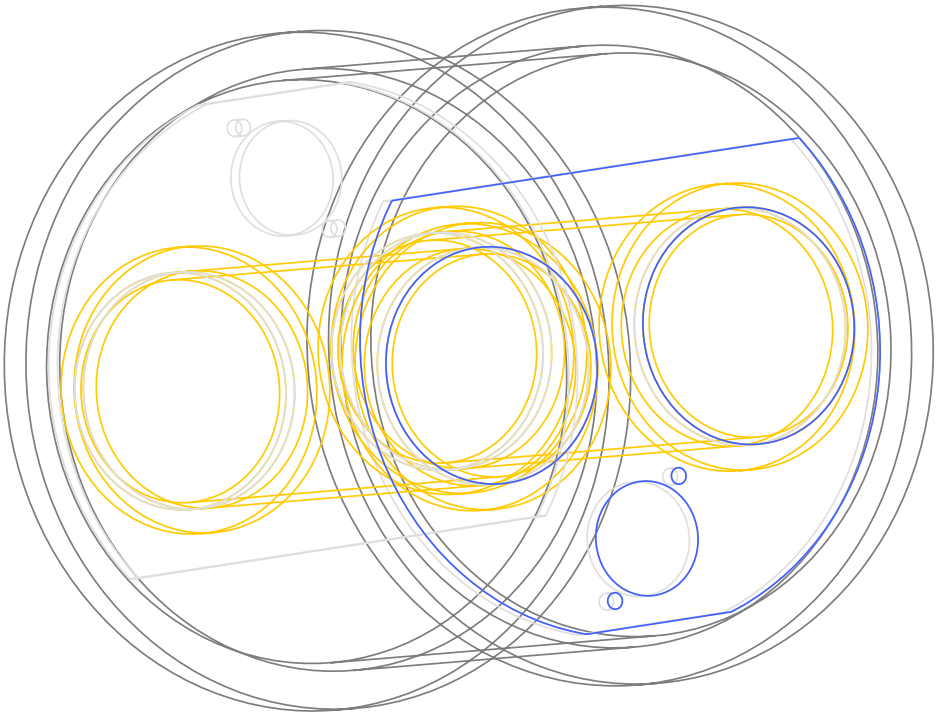

Figure 4.4: Coil assembly showing the sample coils in yellow and the laser cut mounting plates in blue as inserted into the larger outer tube representing the polarization coil.

The connecting wires of the sample coils are twisted to minimize inductance and electromagnetic pickup, in the connection to the connector. An XLR cable is used to connect the sample coils to the amplifier. This shielded pair cable is widely available in different wire gauges and terminated to a compact, sturdy connector, at low cost. The detection coil assembly can easily be placed into and removed from the polarization coil. A picture of the entire coil assembly is shown in F.4.

4.4 Noise Reduction from Bucking Coils

In a perfect situation where all noise sources are in the far-field of the detection coils, the secondary bucking coil will reduce environmental noise to zero. Some notes about the limitations of noise canceling qualities of the bucking configuration are made in section 3.4 However, no qualitative measures are predicted due to the nature of the noise. Therefore, to estimate the effectivity of the bucking coil configuration, only empirical measurements in typical environments can be made. To this end, the bucking coils were placed in an office environment where typical environmental noise is present and the noise reduction measured.

A first measurement sequence was performed with only a single coil enabled, and the second coil shorted to ground. The second sequence measured differentially across both coils in bucking configuration. Thermal noise of the coils is thus twice as big in the second sequence compared to the first sequence. Since thermal noise of the coils accounts for roughly 50% of total amplifier noise (see section 3.1), total noise level for a single coil, including amplifier noise but excluding environmental noise, is roughly 25% lower than for two coils.

For these measurements, the resonance circuit was disabled and no sample was present in either of the two coils. Moreover, the polarization coil was shorted for all measurements. Each sequence consists of 16 measurements, each measurement 1 second long. To optimize full scale digitization capabilities of the ADC, amplification factor was optimized to match the full scale voltage swing of the input signal while avoiding digital clipping. All other measurement parameters were kept equal.

First a typical noise spectrum of a single coil measurement is displayed in figure 4.5.

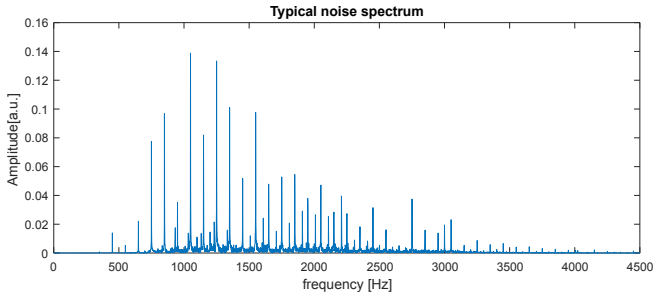

Figure 4.5: Typical noise spectrum measured inside an office environment, made using only 1 of the two coils in bucking configuration.

The typical noise spectrum is dominated by harmonics of the powerline, which is $50Hz$ in the Netherlands. In addition, it can be seen that the spectrum is filtered by the bandpass filter present in the amplifier around its intended bandwidth although lower frequencies do show higher amplitude. For the average of the 16 measurements Root Mean Square (RMS) noise amplitude was found to be $0.301V$ at an amplification factor of 10. Comparing this to the total noise with 1 coil connected consisting of amplifier noise and thermal noise of one coil (see 4.3), this is roughly 200 times bigger. Environmental noise when using a single coil is thus the dominant noise contribution in EFNMR experiments, by two orders of magnitude.

For the bucking coil configuration the same measurements were performed at an amplification factor of 400 yielding an average RMS noise level of $0.1325V$. The amplifier and thermal noise equal roughly $0.08V$ at this amplification factor and thus thus the environmental noise makes up only 40% of the total noise. By using the bucking coil, environmental noise is reduced by a factor 227 or $47dB$ and total noise level by a factor 90, or $39dB$. To indicate total noise level and its composition based on the numbers in this 3.2 and 4.3, in 4.3 an overview of noise contributions in a typical office environment is given. When a measurement is performed outside and away from noise sources, or placed inside a conducting

Table 4.3: Overview of the contributions of the various components to the overall noise level in an EFNMR measurement using the bucking coils.

Noise contribution	
Amplifier current and voltage noise	34 %
Thermal noise of coils	26 %
Environmental noise	40 %

material of sufficient thickness, noise levels can be reduced further until almost only amplifier and thermal noise of the coils remain.

As explained in section 3.4, noise reduction of the bucking coils has an angular dependency. To illustrate this, assume a directional noise source is present close to the setup. On axis, cancellation will be maximum. Perpendicular to the axes of the coils no noise will not be any picked up and somewhere in between these two, noise reduction will be minimal. To show this, a measurement was made with a small air core coil placed $1m$ away from the bucking sample coils. It was connected to a signal generator producing a single frequency sine equal to the sample coil's resonance frequency, minimizing the influence of other environmental noise sources. The bucking coils were rotated in steps of ten degrees around the point where the XLR cable connects to the sample coils. The resulting signal amplitude is displayed in figure 4.6. In the polar plot, 0° corresponds to the point on axis and 90° and 270° degrees is

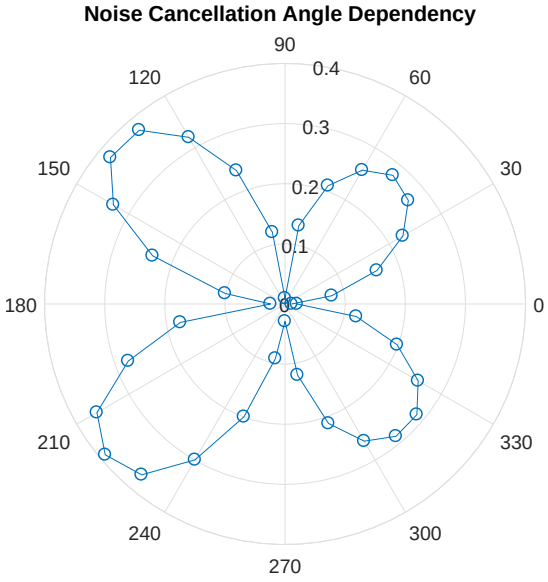

Figure 4.6: Polar plot of signal amplitude as function of rotation angle of the bucking detection coils relative to a directional source.

perpendicular to the axes of the bucking coils. Signal amplitudes in the plot are linear values derived from Fast Fourier Transform (FFT) peak value. The polar plot shows an asymmetry for the left half plane compared to the right half plane. This is due to the rotation point being the front of the bucking coils, instead of their center. Distance between the bucking coils and source is thus smaller when the bucking coils are oriented with the connector away from the source, compared to when the connector is oriented towards the source. This has been done on purpose, to illustrate the effects of near-field sources. While on axis of the coils the noise reduction is large, towards the sides, signal amplitude is roughly 30 times larger than on axis. Therefore, small changes to the orientation of the setup can have a big impact on total SNR if directional sources are present nearby the setup.

Chapter 5

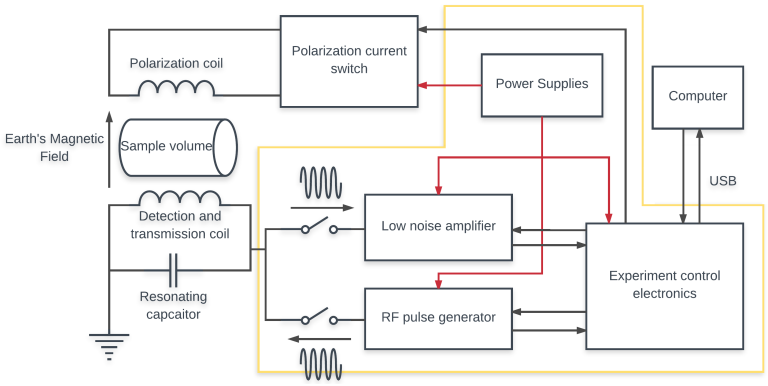

Signal Amplifier and Experiment Control Electronics

Now that the polarization and detection coils have been designed, the measurement signal needs to be amplified and filtered. To design an amplifier, the required amplification, filtering and various other parameters required to make an EFNMR signal amplifier, first a specific overview of demands the electronics must satisfy is given. Only after these demands have been defined, does the actual specification of the electronics themselves begin.

The development process of the experimental setup describing how it transformed from a simplistic setup, capable of only measuring FID with low SNR, to the setup as it is today, is given in appendix B.

5.1 EFNMR Amplifier Requirements.

Based on the EMF, calculated for the sample coils, with a sample of $100mL$ of pure water, the amplification factor required to boost the EFNMR signal from the microvolt range (see section 3.3) to the digitization level is around $111dB$. This requires precise, noise free amplification. Designing such an amplifier requires great attention since if only a portion of the output signal is fed back to the input, the amplifier will easily oscillate. In addition, the electronics also need to be flexible enough to allow various samples to be measured, as well as allowing room for possible later re-developments of the measurement coils, without needing to redesign the amplifier. To allow this, several orders of magnitude in variance of the total amplification factor should be possible.

A second requirement the signal amplifier must fulfill, is that it has to be able to make the detection coil resonant by inserting the correct capacitance in parallel with the detection coil. Since the resonance frequency of the coil has to match the Larmor frequency, and we already noted that the Larmor frequency varies both per location throughout the day as well as per location, the resonance frequency must be variable. This can be achieved by wiring different capacitors in parallel and enabling the correct combination of these capacitances, depending on the desired resonance frequency. Whether this switching is done mechanically through a switch, a relay or some other method, it must provide satisfactory frequency resolution to obtain an optimal resonance frequency that maximizes signal amplification due to the quality factor of the coil.

Thirdly, output signal from the signal amplifier has to be a band-pass filtered before digitization. Ideally, signal supplied to the ADC for digitization contains only EFNMR signal. However, this is far from realistic. Several noise sources exist in a typical EFNMR measurement as described in section 3.2 which degrade SNR. In the magnitude of all these noise sources, the bandwidth of the noise, Δf, appears. Lowering the bandwidth of the measurement signal thus improves SNR. Moreover, given the Nyquist theorem, to prevent aliasing

the signal must not contain frequencies above half the sampling rate. To fulfill both demands, EFNMR signal must be band-pass filtered to remove unwanted frequencies, while passing the full frequency range needed to perform EFNMR measurements around the globe (see section 3.1). This filtering, in the range of $1.0kHz$ to $2.5kHz$, should pass unaffected. The stopband should be attenuated as much as possible, without drastically affecting the impulse response of the filter.

General experiment control and digitization requirements

An EFNMR measurement cycle contains multiple events. These can consist of starting and stopping a polarization cycle, a measurement cycle, various pulses at any given moment, as well as sending measurement and control data to and from the host interface. The timing of these events require high temporal resolution since small shifts of these events can introduce measurement artifacts in the results. Although a modern stand-alone computer is fast enough to handle these tasks, it is not suited for these time critical tasks due to the way interrupts are handled in the operating system. Therefore, to perform all the time critical tasks in the experiment, a microcontroller is used.

A microcontroller is a small, user programmable processor that can run a set of code depending on the conditions of several inputs. For the EFNMR hardware, the open-source Arduino platform is used. Arduino is a combination of off the shelf complete hardware, that integrate a microcontroller and other essential electronics onto a standard size PCB. Moreover, it has an Integrated Development Environment (IDE) in which the microcontroller can be programmed. Within the Arduino IDE, many standard, well-tested libraries that incorporate all sorts of useful functions are readily available and the user base is very big. Moreover, the Arduino IDE uses a code based on C++ which can be easily learned for anyone familiar with programming. Finally, to ease the testing process of new Arduino code, also the flashing of firmware to the microcontroller is performed from within the Arduino IDE.

A typical Arduino has multiple input and output ports, both analog and digital. An analog input port can be used to measure a voltage applied to it whereas digital inputs can only differentiate between a high and low state. Similarly, analog outputs can output voltage in a discrete manner, while digital outputs can only output a high and low, on or off voltage. The microcontroller also features a serial connection which can be used to communicate to and from a host computer. This can be used to transfer any form of control information or signal data.

To fully optimize the integrated capabilities of the Arduino platform, EFNMR signal sampling is performed using the built in ADC. This ADC must fulfill the following requirements.

1. Sampling frequency should be at least twice the highest spatial frequency in the measurement signal following the Nyquist theorem.

2. Total sampling length must be sufficient such that a full FID or pulse sequence can be measured in a single measurement.

The Arduino which satisfies these constraints and was eventually selected[1] to be used is the Teensy 3.6. In section 5.2 properties of this Arduino will be highlighted.

[1] In appendix B.2, we describe why the Arduino Uno, which was first used, was replaced for an Arduino Due and later for a Teensy.

5.2 Main Board

The electronics of the setup consists of a main board and a polarization board, which was already described in section 4.2. The main board is split into four sections, a measurement signal input section, a pulse section, a hardware control section and an auxiliary section comprising the power supplies and interfacing connections. In figure 5.1, an overview of the

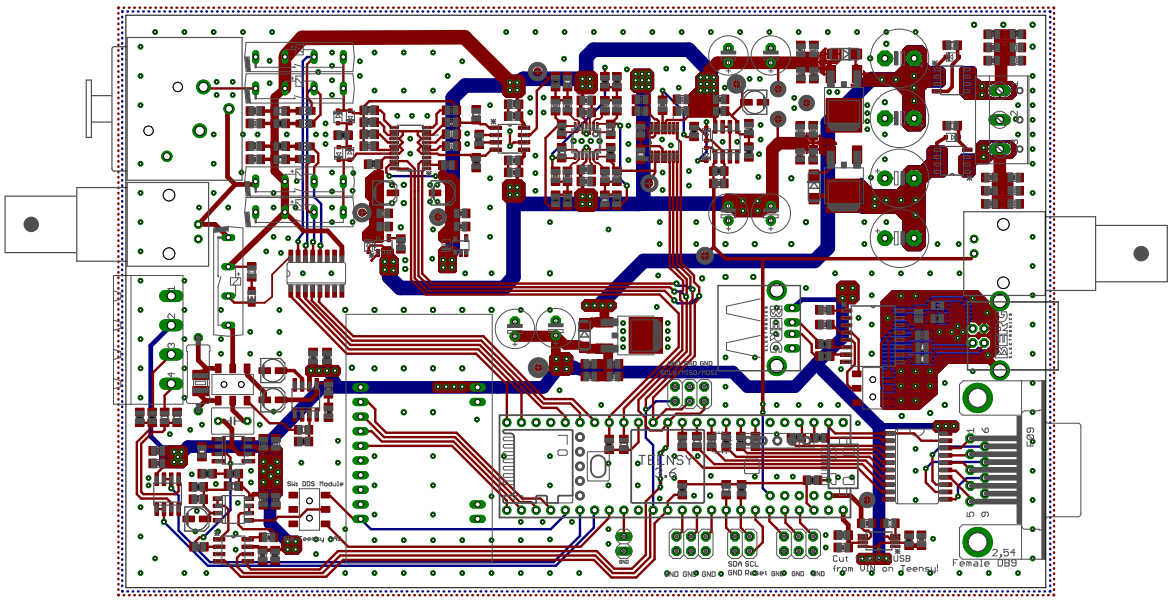

Figure 5.1: Overview of the PCB layout of the main board.

main board as it has been laid out on a 2-layer PCB is given. A PCB consists of a substrate with multiple copper planes on it. These planes can be etched such that what is left are the electrical connections between various electrical components. [1] In blue, signal and power traces on the bottom layer are shown and in red those on the top layer. The EFNMR signal input connector is mounted on the top left of the board, with four reed relays to switch the coils, placed in line towards the right. To the right of the relays, the resonant circuit tuning is placed. As we move further to the right, the first amplification stage, bandpass filter, variable amplification and ADC conditioning are placed. The left-to-right layout has been chosen since this best separated input and output, minimizing the chance of crosstalk and oscillations.

At the bottom left corner of the PCB, the pulse generation can be seen and at the bottom right the Teensy as well as external interfacing buffer is placed. At center right, the Universal Serial Bus (USB) connector which connects the host computer galvanically isolated from the hardware. Finally, at top right the power supplies for the analog section of the board are placed. The digital supply that power the Teensy and pulse section, is placed in the center of the board. Attention has been paid to keep digital and analog parts of the circuit as well separated as possible. Pictures of the main board can be found in appendix E.

Input switching and first amplification

The input section of the main board consists of a signal selector, resonant coil tuning circuit, pre-amplifier, bandpass filter, variable gain amplifier and ADC signal conditioning. The basic functional blocks of the circuit, two coils of the bucking setup, input switches, protection

[1] In appendix B.1 and B.3, development of the main board is described. In this chapter, multiple reasons for using a PCB are given.

diodes and switched capacitors as well as the first amplification stage is shown schematically in figure 5.2. Note that this figure does not show an actual schematic but serves only to illustrate the building blocks. The signal selector has been designed with four reed relays that

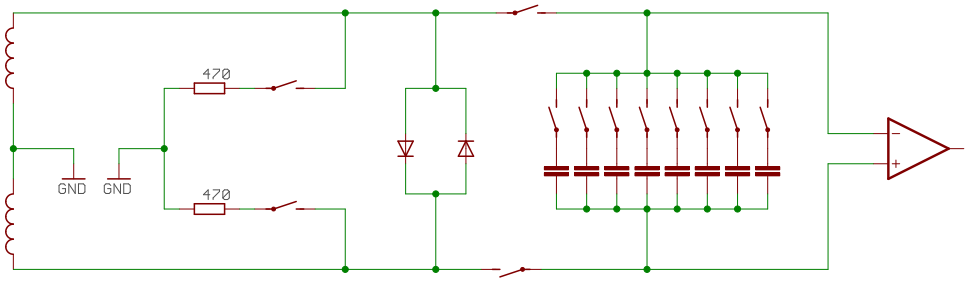

Figure 5.2: Illustration of the basic functioning of the first stages of the signal amplifier. At the far left, two coils of the bucking coil configuration are shown, towards the right first the protection diodes, damping resistors and switches, switched capacitors and finally the instrumentation amplifier are shown.

allow either unipolar measurements across a single coil, as well as differential measurements across two coils in bucking setup. For each coil, a series enable relay is used as well as a parallel relay that can switch the coil to ground through a resistor. The resistor value is selected such that a critically damped RL circuit is formed when the coil is switched to ground. This minimizes both damping time of the energy in the coil as well as suppress ringing after the end of a pulse. As alternative to this energy dissipation through a resistor, also active feedback schemes can be used such as those described by [45] and [3] . Reed relays were selected since they have a lower switching and settling time compared to conventional mechanical relays. Relay drive is performed by a ULN2003, which provides sufficient drive current to the relay coils as well as isolate the microcontroller from the inductive kickback behavior upon relay switching. Each of the relays is paralleled by a light emitting diode (LED) to visually indicate relay operation. Finally at the input section, diodes are placed parallel to each of the connecting coils such that the downstream circuitry is protected from voltage spikes that may occur.

Variable resonant coil tuning is implemented using an Analog devices ADG714. This is a serially controlled, octal CMOS switch which can be set through a serial peripheral interface (Serial Peripheral Interface (SPI)), allowing the microcontroller to set the state of each switch individually. Each of the eight switches is connected in parallel to the differential coils, with a series capacitor of differing value per switch. Using different combinations of the switched capacitors a wide range of total capacitance can be achieved. Following equation 1.9, thereby the coil's resonance frequency can be varied. This allows the coil to be optimally tuned to each Larmor frequency in the range of earth's magnetic field intensities across the globe as well as allow room for different tuning frequencies for various sample materials, all whilst using a single coil. In traditional NMR this would be impossible since the voltages used for RF pulsing are much higher. This makes it difficult if not impossible to switch various capacitances to allow variable tuning frequencies.

The pre-amplifier employs a low noise Analog Devices AD8428 instrumentation amplifier. The instrumentation amplifier is connected across the switched capacitors to utilize the resonant behavior of the RLC circuit as explained in 3.3. The AD8428 has an input impedance of $1G\Omega$, so it does not load the measurement coils, and the assumption made in section 3.3 of negligible input impedance, R_{in}, is valid. The AD8428 provides a fixed differential voltage gain of 2000. Moreover, it features an access point to the internal gain resistors allowing the connection of a parallel capacitor to low-pass filter the input signal and prevent high frequency noise directly in the pre-amplifier. The total voltage noise of the amplifier is

$1.5nV/\sqrt{Hz}$ and its current noise $1.5pA/\sqrt{Hz}$. As alternative to the AD8428, also the Burr-brown INA166 from Texas instruments was considered. It offers comparable voltage noise and slightly lower current noise and lower voltage offset. The package size of this Integrated Circuit (IC) is however larger and it does not offer the filter possibility of adding a filter capacitor. Moreover, it could not be sourced from any supplier.

Effectively, the pre-amplifier amplifies the input signal in the microvolt range to the millivolt range. Moreover, this stage converts the measurement signal from a unipolar measurement across a single coil or a differential measurement across two bucking coils to a single ended signal referenced to ground potential. To allow for this, the center tap of the bucking coil is connected to this ground potential through the shield of the XLR cable.

Filtering and final amplification

The bandpass filter is designed as an 8th order Chebyshev filter, optimized to have smooth group delay and impulse response through the bandwidth of $1.0 - 2.5kHz$ while providing unity gain and steep roll-off either side of the pass-band. Once the design criteria were set, the filter was designed with low noise as optimization goal since the signal level passing through it is still in the millivolt range and the resistors also cause Johnson noise. To achieve this goal, resistors with low resistance values as low as possible were used. The op-amp selected is a Analog Devices ADA4851. This is a rail-to-rail capable op-amp with low voltage offsets.

Filter topology used for the bandpass filter is a series of four cascaded infinite-feedback, second-order bandpass filters. The schematic design of the bandpass filter with correct values is shown in figure 5.3. The variable amplification stage contains a Linear Technologies

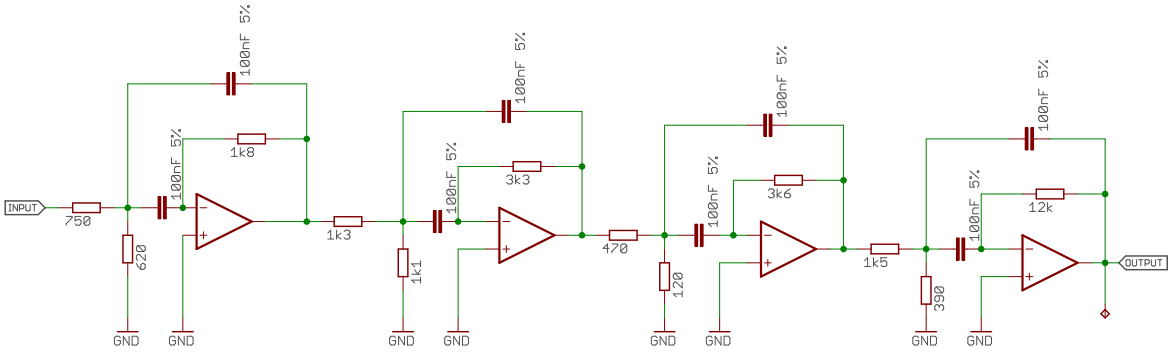

Figure 5.3: Schematic of the 8^{th} order Chebyshev bandpass filter

LTC6912-1 Programmable Gain Amplifier (PGA). It is controlled through an SPI interface by the Teensy and has two (inverting) amplifiers with adjustable gain between unity and 100. The two amplifiers are cascaded in series, allowing for multiple gain values between unity and 10000. The total amplification of the entire amplifier including the first stage can thus be as low as 2000, or as high as 20 million. This is sufficiently high to measure any EFNMR signal even from small samples or other sample coils with less windings. Moreover, the two stages are AC coupled to again low-pass filter the measurement signal. Note that this PGA, as well as the ADG714 were both selected since their SPI interface do not require any clock signal to be present in normal operation, but only during setup. This prevents high frequency noise on sharp transitions of clock pulses to bleed into the measurement signal.

Noise levels of the LTC6912-1 decrease monotonously as the amplification factor is increased, from 31.1 $nV/\sqrt{Hz}$ at unity to 12.6 $nV\sqrt{Hz}$ at gain 100. Therefore, in the programming, the first of two cascaded amplifiers always uses the highest gain possible, minimizing noise introduced by the PGA.

The third and final stage comprises an op-amp with two amplifiers. This stage provides

buffering as well as level shifting and voltage limiting to feed the ADC onboard the Teensy. The first amplifier buffers the reference voltage with which the measurement signal is level shifted. This offset voltage is properly decoupled to provide a clean and stable, low impedance voltage source, even under powerline fluctuations. The signal is then passed to the second amplifier, which acts as a buffer and level shifter. It utilizes Zener diodes in its feedback network to limit the maximum output voltage going to the ADC, to protect it from overvoltage which could potentially damage it.

Pulse generation electronics

Pulse generation is currently implemented using an Analog Devices AD9850 Direct Digital Synthesis (DDS) IC, with integrated Digital-to-Analog Converter (DAC). The DDS-IC can be programmed using the Teensy to generate sinusoidal signals with frequencies between DC and $40MHz$, with spatial resolution of 0.0093 Hz. Moreover, it can be quickly switched on and powered down by the Teensy, allowing discrete timing of start and stop times of pulses and thereby total pulse length. Initial phase of the output waveform can be varied in steps of 12.5° between zero and 347.5° and thus CPMG sequences are possible. The AD9850 is purchased as sub-assembly with clock crystal and low-pass filter integrated onto a small PCB, allowing easy replacement or removal.

This might happen if the Teensy is programmed to support DDS directly. At this moment, this has not been done. However, to allow for this possible future expansion, a selector switch is placed on the PCB that allows switching of the signal between the DDS module and a DAC onboard the Teensy.

Following the selector switch, the signal is buffered to provide a low impedance source for the LM1917 variable attenuation IC. The LM1917 can attenuate a signal in steps of $1dB$ between unity gain and $-60dB$. It also has a mute function and the IC is controlled through an SPI connection. The pulse amplitude can hereby be controlled.

Before supplying the signal to the sample coils, it is buffered for the correct coil impedance. To allow a wide range of coil impedances to be used, two buffer circuits are integrated on the PCB. The first is a high current conventional op-amp that is able to power impedances as low as 100Ω and higher. The second circuit features an LM386 which can power low impedance detection coils as low as 8Ω. The entire pulse signal is then AC coupled and offered to a relay that can be switched to the detection coils.

Hardware control

The Micro Controller Unit (MCU), is the heart of the EFNMR platform. The MCU used is the Teensy 3.6 that runs at $160MHz$ and has 192kB of Random Access Memory (RAM). When storing a measurement signal to RAM as 16-bit integers, it offers a maximum of roughly 500.000 measurement points. At $F_s = 10kHz$, this is enough to capture a signal lasting 50 seconds, enough to measure any pulse sequences. It also has an integrated ADC which has been tested to sample stably at sample rates up to $35kHz$ while performing single value averaging of up to 64 averages per measurement point, with a total resolution of 12 bits.[1] Its maximum safe operating and input voltage is 3.3V and the ADC is not $5V$ tolerant.

During an EFNMR experiment, the MCU performs multiple tasks such as pulse generation control, relay switching and sampling. The most important task performed by the MCU is precise sampling of the measurement signal. Precise timing of all other events however, is

[1] At sample frequencies above $35kHz$, sometimes a conversion would take one additional clock cycle which effectively reduces sample frequency. This test was performed using the same 64 point, single value average as actual measurements use. Sampling frequency can be increased further by reducing the number of averages per sample point, which increases sampling noise.

critical for repeatability. To make sure that this is possible, the Teensy 3.6 was selected which features Direct Memory Access (DMA). DMA allows data to be transferred directly between the ADC and RAM without interference from the central processor. When the ADC has finished a conversion, it sets an interrupt flag. This flag is continuously polled by the DMA interface such that upon detection of the flag, the DMA controller moves the ADC result directly to the RAM, leaving all processor power available for other events.

To allow connection of the external board that houses the polarization hardware and the prototype gradient drivers, eight digital outputs of the MCU are broken out on a D-Sub connector containing also the ground connection and regulated digital $5V$ supply. Since both ground and powerline are supplied on the connector, the host side of the cable can enable digital isolation with an Analog Devices AduM2401 to isolate external hardware from the main board, minimizing noise on the powerlines. Moreover, this allows the polarization circuit to be powered from a different power supply than the one feeding the main board.

Finally, the Teensy has the capability of running a full speed $12MBps$ USB connection to the host computer, to quickly transfer measurement data. The Teensy is bought as external module and plugged onto the main PCB with headers to allow easy replacement should it be required as well as reducing assembly cost.

Auxiliary interfacing and power supply

On the main board, input voltage is supplied by a polarized 3 pole Phoenix MSTB connector that allows easy plug and play power connection with external power supplies. To protect the main board from power errors such as voltage reversal, several protection features have been integrated. Moreover, to be able to power the NMR platform circuitry from any power source, linear voltage regulation is employed that offers the hardware a stable and clean voltage source. It allows connection of input voltages between $8VDC$ and $36VDC$. This makes it possible to power the hardware from batteries, to operate the setup outside where power is not accessible.

Ground and power potentials on the EFNMR electronics are isolated from those of the host computer connecting to the hardware through USB. This is done with an Analog Devices AduM3160 USB isolator. This prevents noise from the host to cross onto the EFNMR electronics.

To conclude, two analog inputs which are buffered before being offered to the Teensy, are added on the main board. The input connector used also has a power and ground connection for various powered sensors such as flux gate magnetic field sensors. In addition, the amplified measurement signal is supplied to a BNC connector such that it can be viewed on external equipment such as an oscilloscope.

5.3 Amplifier Noise and Bandpass Filter Response

When the amplifier's inputs are shorted, total amplifier noise level can be evaluated. Noise originates from multiple positions in the amplifier although when the amplifier is designed properly, primary noise sources are voltage noise of the AD8428 as well as the series resistors in the bandpass filter (see figure 5.3 for the schematic of the filter) and the noise produced by the PGA, which varies with the amplification factor used. Current noise of the AD8428 can be neglected since no resistance is present to convert it into a voltage.

Voltage noise density of the AD8428 amplifier, according its data sheet, equals $1.3nV/\sqrt{Hz}$. When amplified by the constant amplification factor of 2000, this becomes $2.6\mu V/\sqrt{Hz}$. Voltage noise density of the bandpass filter was designed to be $100nV/\sqrt{Hz}$. Noise from the bandpass filter is thus 26 times smaller compared to noise from the first amplification stage. The theoretical total RMS equivalent noise across the filter bandwidth of the amplifier, $1.5kHz$, equals $101\mu V$ after the bandpass filter.

The total RMS amplitude of the noise level, averaged over 16 measurements of 1 second, was obtained to be 0.0441 V at a PGA amplification factor of 400. The total equivalent RMS noise before the PGA equals $110.3\mu V$. At this amplification factor, the total (unfiltered wideband) noise induced by the PGA itself (LTC6912-1) equals $7.7\mu V$ RMS at its input. There is thus a discrepancy of roughly $1.6\mu V$ of RMS noise between the calculated noise level of only the raw components. This can be due to parasitic resistances in PCB tracks, finite resistance of the wires used to short the inputs of the amplifier or a slightly different true bandwidth of the filter. Moreover, the discrepancy is small compared to the total noise of only the raw components and spec-sheet data does not necessarily conform to device-to-device performance.

The total amplifier noise of $0.0441V$ calculated backwards to the equivalent noise density at the first stage assuming the $1.5kHz$ bandwidth equals 1.74 $nV/\sqrt{Hz}$, only slightly higher than the voltage noise of the amplifier itself. Since noise thus primarily originates from voltage noise of the AD8428 when its inputs are shorted, measured noise signal also shows the frequency response of the bandpass filter. Normalized frequency of both simulated (red) and measured frequency response in blue is shown in figure 5.4.

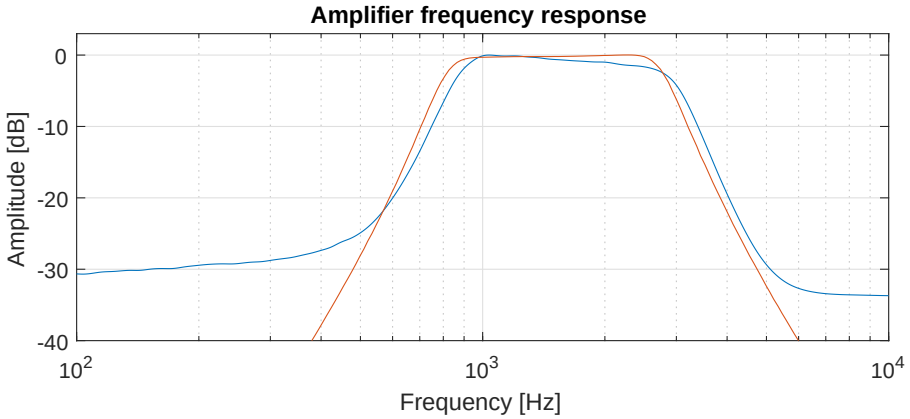

Figure 5.4: Frequency response of the bandpass filter. In red the simulated response of the filter is shown and in blue the actual measured frequency response.

As can be seen from figure 5.4, the response of the constructed filter matches the designed response well. Over the passband from $1kHz$ to $2.5kHz$, deviation is $1.6dB$ maximum. Also, the passband is shifted slightly upwards compared to the design goal. These deviations originate primarily from component tolerances in the bandpass filter.

5.4 Variable Amplification Linearity

One of the fundamental assumptions in all EFNMR experiments, is that the amplification factor of the PGA scales linearly with the desired setting, supplied by the Matlab Graphical User Interface (GUI) (see section 6.1). The manual of the PGA shows good linearity of amplification at all amplification factors allowed. However, actual performance depends on implementation of the IC and therefore a calibration measurement has been performed. To do so, the bucking coils were connected to the amplifier with the resonant circuit disabled. A series of 32 measurements of one second were performed per amplification factor step. RMS noise value was assessed per measurement and the results averaged, to find the average RMS noise amplitude. This process was repeated at each amplification factor. The results of this measurement series are displayed in figure 5.5. In red the linear fit of the amplification factor

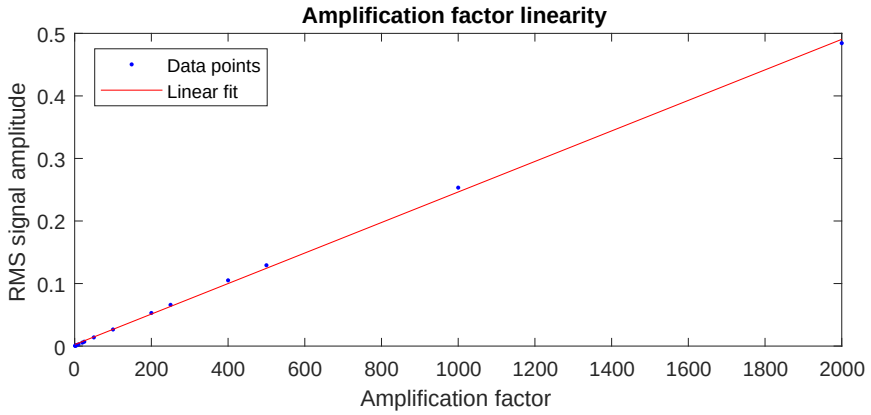

Figure 5.5: Actual measured amplification factor as function of set amplification factor.

is shown while the raw data points are displayed in blue. Adjusted R^2 of the linear fit was 0.9992 showing good linearity of the amplification factor. Moreover, this measurement shows no programming errors have been made in setting up the communication between the PGA and Teensy.

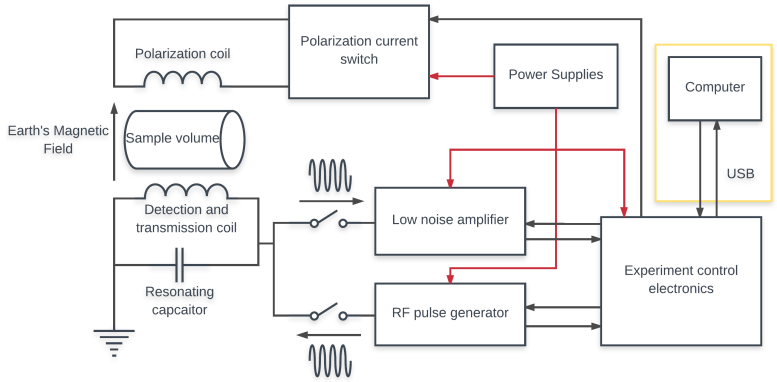

Chapter 6

Performing an Experiment

All mechanics and electronics required to perform an EFNMR experiment have been analyzed, desgined and described. We are now ready to perform experiments. However, we cannot directly interface ourselves to the electronics. To bridge the gap between a list of parameters and the electronics, which are controlled by the Teensy, a Matlab GUI has been developed. In addition, essential parts of programming and sequence timing used in both the Matlab GUI as well as on the Teensy, are explained in appendix C.

6.1 Matlab Measuring GUI

In Matlab a GUI has been developed, capable of performing various EFNMR pulse sequences; the adiabatic FID, adiabatic spin echo, adiabatic CPMG sequence as well as their non-adiabatic equivalents.

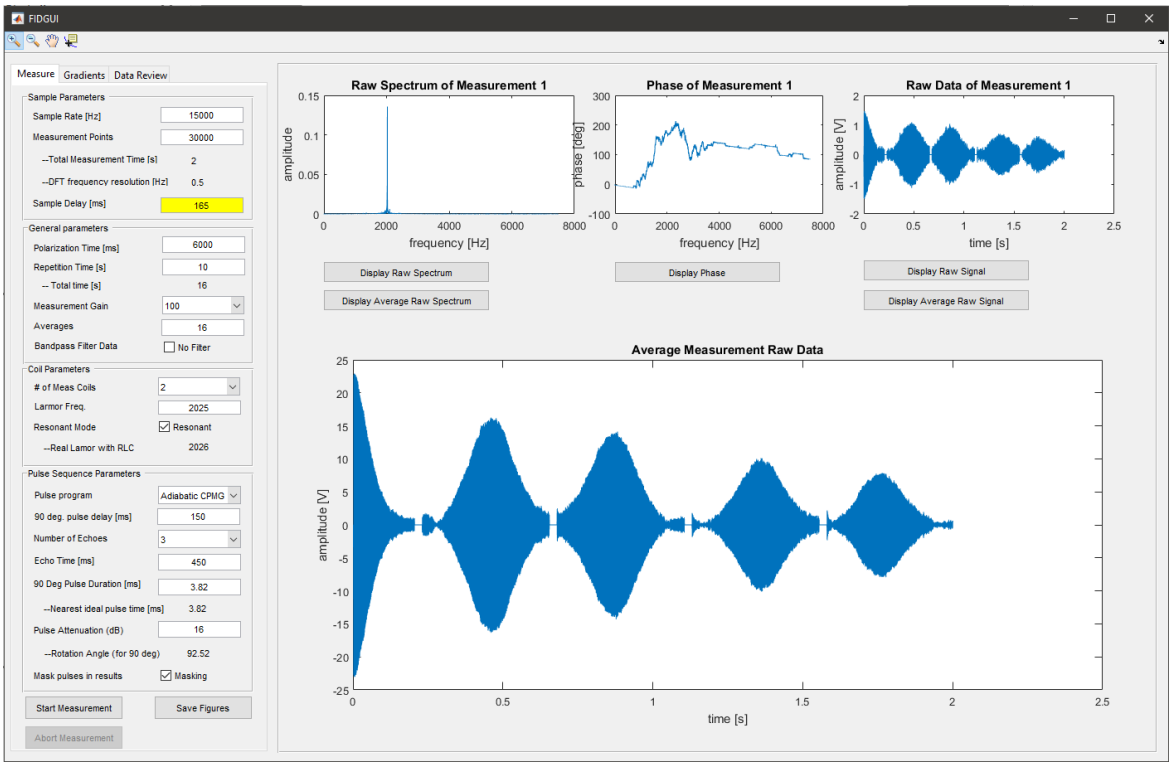

Figure 6.1: Measuring Tab of the GUI.

During GUI initialization, coil parameters such as inductance, resistance and dimensions are read from a *.txt* file. By using a *.txt* file, the GUI can easily be changed to work for

various coils without requiring access to the code inside it such that the user can easily use multiple coil configurations without having Matlab on their computer. Moreover, all edit- and text boxes in the GUI obtain a default value.

When the GUI has initialized, it starts by default in the measurement tab as displayed in figure 6.1. Inside the measuring tab all process parameters are divided into the groups sample parameters, general parameters, Coil parameters and pulse sequence parameters. In the sample parameter group, sample rate F_s, number of measurement points *pts* as well as sample delay $T_{MeasWait}$ can be changed. When this is done, the GUI will show total measurement time as well as resulting spatial resolution of the FFT.

In the general parameters group, the polarization time, T_{pol}, repetition time, T_R, as well as the measurement gain of the variable amplification IC on the signal amplifier and the number of averages in the measurement series can be set.

The coil parameter file contains the number of coils used to measure a signal can be changed. If a single coil is connected, measuring across 2 coils is pretty useless however if a bucking coil is used, switching between either 1 or 2 coils shows the user the difference between the noise levels in a bucking mode configuration compared to a single coil of the bucking configuration. Furthermore, the coil can be switched between a non-resonant state as well as a resonant state of which the resonance frequency can be varied. The resonance frequency set here also controls the frequency of the excitation pulses.

In the pulse sequence parameter group, the experiment type can be selected as well as all the parameters that control the pulse shape and amplitude as well as the echo time T_{Echo} and the number of echoes N_{Echo}. Choosing a correct combination of pulse amplitude and length can be difficult without writing out the full equations on paper. Therefore, using these two parameters as well as the coil parameters, the GUI automatically calculates an estimate for the effective rotation angle of a 90°pulse to aid the user and reduce the time required to obtain a first signal.

6.2 Matlab Data Review GUI

Besides running an experiment, the Matlab GUI can also be used to review and analyze data. These operations can be performed on a finished experiment that is still loaded in the memory of the GUI, or from previously finished experiments. The data review and analysis features are implemented on a different tab than the measurement options which can also be accesses while a measurement is still running. In the Data Review tab shown in figure

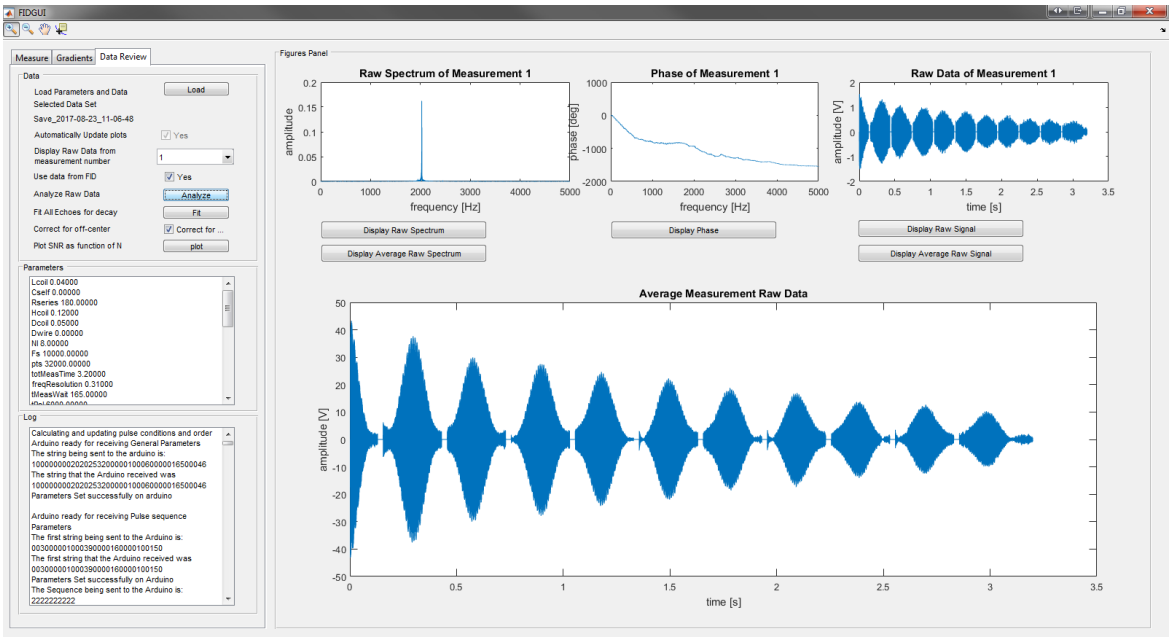

Figure 6.2: Data Review Tab of the GUI.

6.2, three pains are present, the data pain, parameters pain and log pain. The data pain features a load data button which can be used to retrieve data from a previously finished measurement. When a valid measurement file is selected, its name is displayed such that the user always knows which data set is displayed. If a measurement is running, this area will also show the name of the currently running measurement. Below the loading button, a selection box is placed which is enabled during measurements to either automatically update the plots in all the windows inside the figures panel or to freeze it. Moreover, the raw data of each measurement in the series can be displayed in the figures panel both after completion as well as during an experiment.

Data analysis options are analyzing the raw data of a single measurement, fitting all the echoes in all measurement to determine the T_2 times and plotting the SNR as function of the number of averages. Moreover, when an FID only measurement series is finished or loaded, the GUI automatically displays the FID peak frequency as a function of time to investigate temporal behavior of the earth's magnetic field strength and Larmor frequency.

The parameters pain shows all the experiment parameters used to generate the measurement results. The log pain shows all events and short statistics of each individual measurement such as data transfer elapsed time, real sample rate used and signal to noise ratio. During a running experiment, the log pain is updated after each measurement to give the user a real-time view of the experiment status.

The button "*AnalyzeRawData*" displays all the processed information from a single raw measurement. These are the sum of all spectra of all echoes in the measurement, the peak frequency inside the FFT per echo, the peak value in the FFT per echo and the Signal to Noise Ratio per Echo. An example of this window is shown in figure 6.3. The sum of spectra

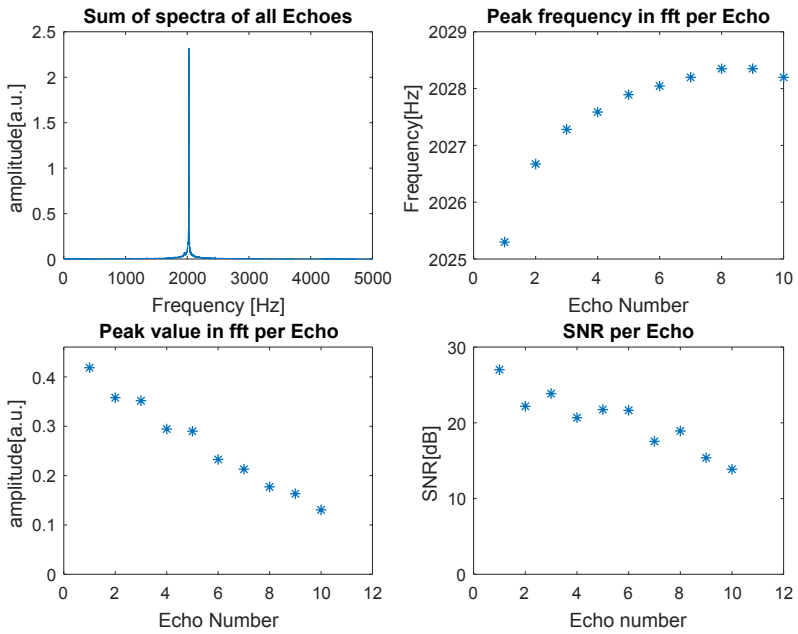

Figure 6.3: Example of the "Analyze Raw Data" Window showing processed data of a single measurement.

of all echoes is simply the sum of all the Fourier transforms of all individual echoes. Note that in figure 6.3, no zero padding is used such that the user can see the influences of the spectral resolution. The peak value of each echo is the amplitude of the highest value present in each spectrum and the peak frequency is the frequency at which that peak occurs.

In figure 6.3, the FID has not been included in the processed data shown, however it can be. In the data pain, a checkbox can be marked such that this FID data is either used or skipped during processing. This is done to maintain integrity of the data itself since the FID is at least twice as short as subsequent following echoes and distorted by transient decay. In the spectrum, FID peak amplitude is thus always lower than that of the first echo, which will result in distorted T_2 fits.

Chapter 7

NMR Measurements

In this chapter, capabilities of the setup and effects using various measurement configurations are shown. First, we study the influence of the current switching method on the FID. Secondly, we analyze T_1, T_2 and signal amplitude for water and Galden. In this section we also show the capabilities of performing basic spectroscopy using a reference sample.

To conclude, we highlight some aspects on the temporal stability of the earth's magnetic field strength and its influence on measurement results, especially concerning averaging.

7.1 T_2 of Adiabatic and Non-adiabatic FID

An FID can be measured in two ways; adiabatic or non-adiabatic. The differences between these two methods are described in 2.2. However, the influence of these differences on measurement signal has not been discussed.

Transversal decay time T_2, is not necessarily equal to the measured decay time. Instead, T_2^* is measured (see equation 1.34). Since T_2^* is a measure of field inhomogeneity, it can be significantly smaller than T_2, if the earth's magnetic field strength or RF-field are not homogeneous across the sample volume. From equation 1.19 it is known that on axis of the sample coil, which is also used to generate the RF field, magnetic field strength is not uniform. Thus, per equation (1.19) also the flip angle cannot be uniform across the sample. Since the adiabatic FID uses a pulsed RF field to generate the 90°pulse, T_2^* is expected to be lower for an adiabatic FID than for a non-adiabatic FID. In figure 7.1, the FID following

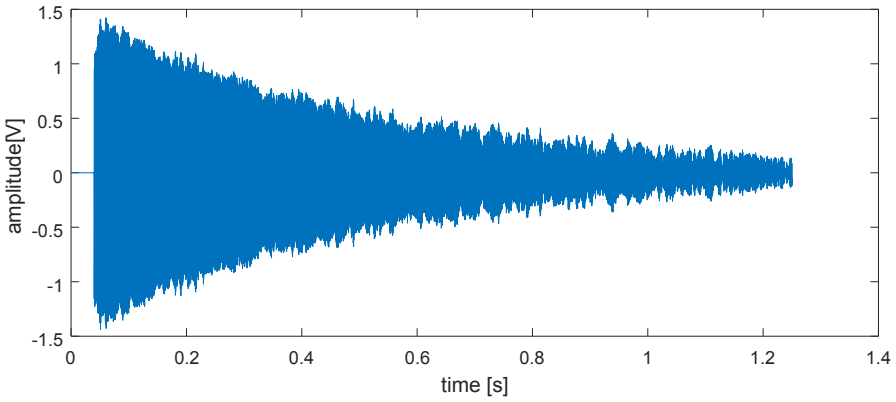

Figure 7.1: Signal of a non-adiabatic FID

a non-adiabatic transition after a polarization time of 6 seconds is shown. To obtain this FID, the setup was placed outside in a field and the coil was made resonant at the Larmor frequency. To optimize signal intensity, a sample of $145mL$ was used. Receiver dead-time is roughly $40ms$. Decay time T_2^* can be determined using spectrum Full Width at Half

Maximum (FWHM) ans equals 0.77 seconds.

Using the same settings for the setup but performing an adiabatic FID cycle yields the image displayed in figure 7.2 and has a T_2^* value of 0.13 seconds. RF field Inhomogeneity

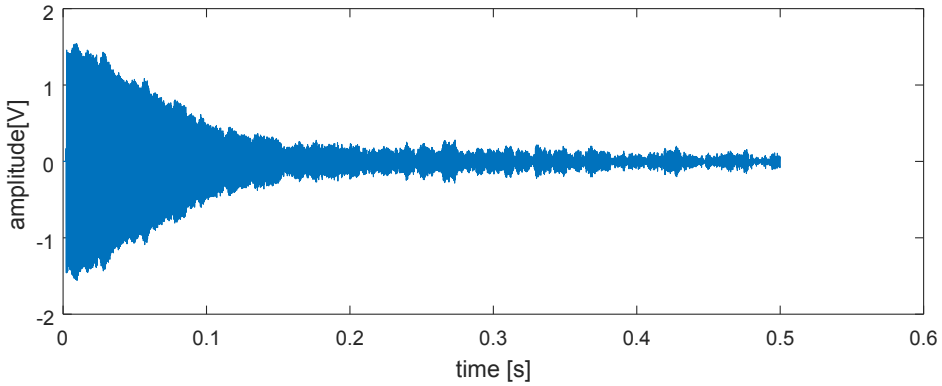

Figure 7.2: signal of an adiabatic FID

thus accounts for an additional reduction of 0.64 seconds in apparent T_2 decay time.

7.2 Signal Amplitude and Relaxation Times of Water

Longitudinal relaxation time T_1 time can be measured using two different methods as described in section 2.2. The first method uses a varying polarization time T_{pol} and measures peak amplitude in the FFT spectrum of the frequency corresponding to the water signal. The second method uses a constant polarization time, but varies the waiting time between the end of the polarization cycle and the beginning of the 90°pulse, T_{90}. Note that the first method works for both adiabatic and non-adiabatic measurements but the second only works for adiabatic measurements. For all measurements presented in this section, adiabatic transitions were used.

EFNMR Signal amplitude

Theoretical induced EMF for EFNMR signals is analyzed in 1.4 and given by equation 1.28 for a solenoidal coil. This equation is expanded in section 3.3 to include the quality factor of the coil when it is made into a resonant RLC circuit. For the solenoidal, bucking detection coils used in this report, final specifications such as induced EMF and resulting SNR have been given in section 4.3. Simultaneously in section 4.4, total noise level was investigated and we found the composition of total noise. One final step to verify the design, is to evaluate total signal level after amplification and compare it to the theoretical value.

For the non-adiabatic FID shown in figure 7.1, Larmor frequency equals $2023Hz$. The sample was polarized for 6 seconds. Assuming a T_1 around 3 seconds, according equation 2.1 this means that sample magnetization was 86% of the theoretical maximum. Since 3.3 and 4.3 calculate EMF using $f = 2kHz$, EMF induced for the measurement shown in figure 7.1 is roughly 88% lower than theoretical maximum considering both different sample magnetization and Larmor frequency. Theoretical maximum EMF expected, for a homogeneously polarized (at $12V$, using the polarization coil specified in 4.1), $100mL$ sample of pure water is $2.57\mu V$.[1] However, to boost signal level, a polarization voltage of $15V$ and sample volume of $145mL$ were used. Corrected for all these changes, expected EMF equals $4.05\mu V$. At a total amplification factor of 400.000 used to measure the FID, this amounts to an expected voltage at the amplifier's output of $1.62V$.

If the time-domain signal of the non-adiabatic FID is corrected for receiver dead-time of $40ms$, then using an exponential decay fit of the RMS FID envelope, measured RMS voltage at $t = 0$ equals $(1.07 \pm 0.02)\,V$. This corresponds to a peak voltage of $(1.51 \pm 0.03)\,V$.

There is a difference of 7% between expected and measured EMF. This difference is negligibly small considering all process parameters involved such as deviations in assumed T_1, exact sample volume, exact amount of detection coil windings, detection coil geometric sensitivity, exact tuning of the RLC circuit and exact polarizing magnetic field strength.

T_1 fit with variable polarization time

To determine T_1 using the first method, the polarization time, T_{pol}, has to be varied while all other parameters remain constant. For each polarization time, waiting time between the first 90°pulse, T_{90} was 150 milliseconds. Repetition time between subsequent measurements is 9 seconds, excluding polarization cycle time. At each value of T_{pol}, an adiabatic FID was performed. The peak value in the spectrum of the FFT was obtained and the measurement repeated, with the peak values averaged. Values of T_{pol} lower than 600 ms were averaged 64 times, between 700 and 100 ms, 32 measurements were averaged while for values higher, only 8 averages were used.

[1] To calculate theoretical EMF expected, a sample volume of $100mL$ assumes pure water containing two protons per molecule and N_A molecules per mole of material. Molar mass of water assumed to be $18.01528\frac{g}{mol}$

Following equation 2.1, the peak values can be fitted to produce the value of T_1. This gives $T_1 = 2.9 \pm 0.2$ seconds. The peak values and fit are shown in figure 7.3.

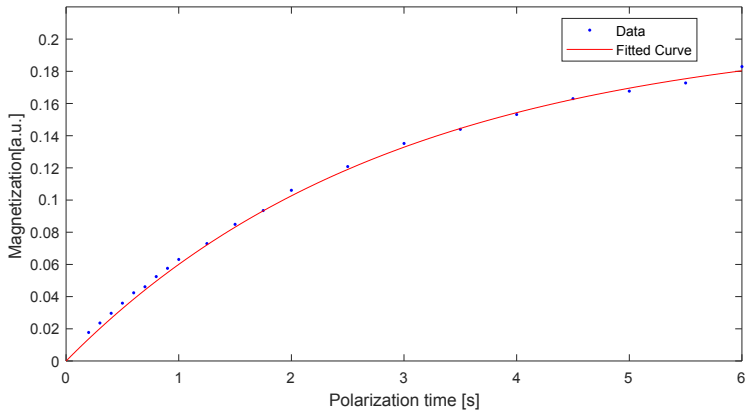

Figure 7.3: Magnetization of water, determined by peak values of the FFT spectrum as function of the polarization time in seconds.

T_1 fit with fixed polarization time

To determine T_1 with a fixed polarization time but variable T_{90}, a CPMG sequence consisting of 5 echoes with an echo time, T_{Echo}, of 275 ms is performed. Sequences with t_{90} between 0 and 2500 ms were averaged 16 times whereas those with T_{90} higher than 2500ms were averaged 32 times due to low SNR. Repetition time between subsequent measurements is 9 seconds, excluding polarization cycle time. Using the averaged signal, y, an exponential decay fit was made to extract FFT peak amplitude at the time corresponding to T_{90}. An exponential decay fit of the form

$$y = a - be^{\frac{-t_{90}}{T_1}}, \tag{7.1}$$

where a and b are fitting parameters, was then performed to determine T_1. Both peak values of FFT amplitudes at T_{90} as well as the exponential fit following equation 7.1 are displayed in figure 7.4. Weights for each point used to produce the fit are the SNR of the average of all first echoes in the CPMG sequence.

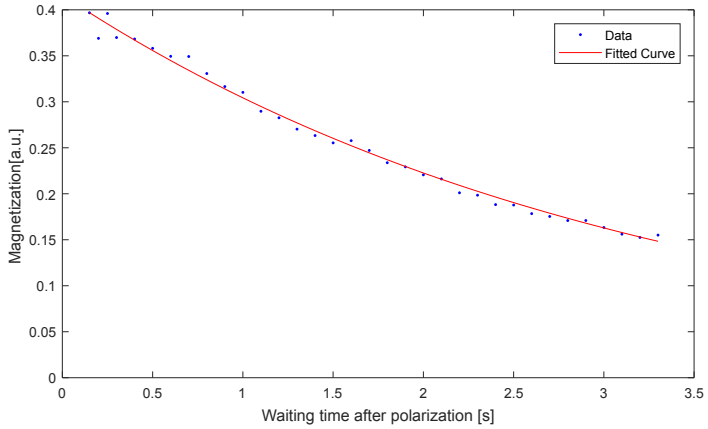

Figure 7.4: Magnetization of water, determined by peak values of the FFT spectrum as function of the waiting time after the polarization cycle, T_{90}.

Using this fitting method, T_1 was determined to be (3.2 ± 0.3) seconds.

T_2 fit

Transversal relaxation time, T_2, of water can be determined using either a spin echo sequence that varies the echo time, T_{Echo}, or using a single CPMG sequence. A CPMG sequence is performed on a sample of $100mL$ of distilled water using 10 echoes with an echo time of $300ms$. The resulting time domain signal when this sequence is averaged 32 times is displayed in figure 7.5.

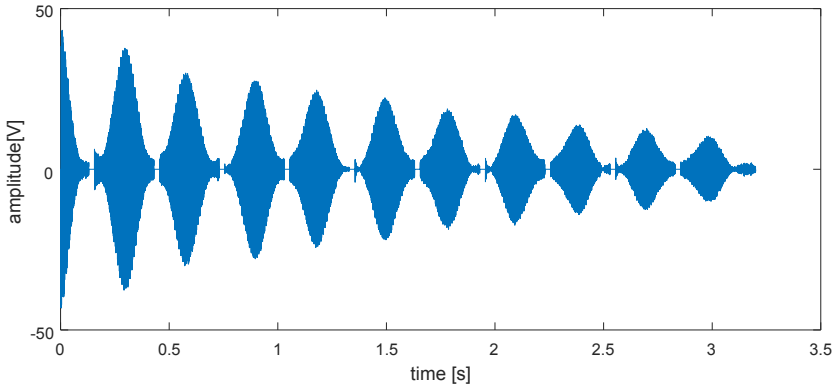

Figure 7.5: Time domain signal of a CPMG sequence of water averaged 32 times.

T_2 fitting of data is performed using the peak value of the FFT of each signal, either FID or echo, combined with the center time of the signal as input data. The center time of the signal can be either the center of the window during which a signal is present, or it can be determined from a Gaussian fit of the signal. The Gaussian fit can be useful when the 180°-pulses are not exactly 180°pulses since they will shift the center of the echo. Fitting peak values of the FFT, which do not occur at the center of the window will then distort the fitting. The user can switch between the two options to see the effects of the correction of the time-offset on the fitted T_2 value. The weights of the data points used to fit the data are the SNR in decibel such that the latest data points with low SNR contribute the least to the overall fit quality. Moreover, the Gaussian fit is only performed when SNR of an individual echo is at least $6dB$ such that no false Gaussian fits for echo signals with low amplitude distort the fit if time-offset correction is used. The resulting fitting window displayed by the GUI excluding the FID with time-offset corrected T_2 fitting is shown in figure 7.6. As can be

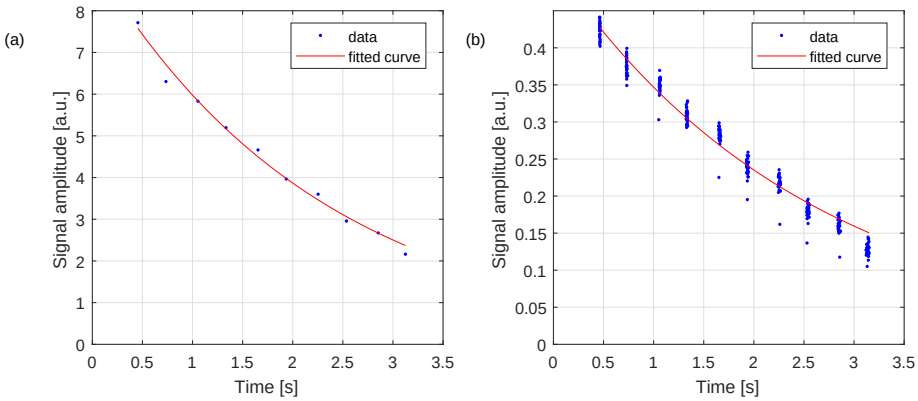

Figure 7.6: T_2 fit of peak FFT values for the CPMG sequence shown in figure 7.5 (a): Decay fit for peak FFT values of all time domain measurements averaged. (b): Decay fit for peak values of all time domain measurements separately.

seen from figure 7.6, two separate fit results are shown. In (a), a decay fit is performed for the sum of all signals combined and in (b) a decay fit is performed with all the data points from the individual measurements. Typically, these lead to different values of the fitted T_2 time. For the measurement shown, fitted T_2 values are shown in table 7.1.

Table 7.1: Fitted T_2 values for the measurement shown in figure 7.6.

Fit type	Time-offset corrected	Non corrected
Sum of all signals combined	2.3 ± 0.2	2.3 ± 0.3
All data points from individual measurements	2.60 ± 0.05	2.62 ± 0.08

The fitted decay values of the data which has not been corrected for the time offsets shows higher uncertainties in the fitting bounds as can be expected. The uncertainty intervals of the two different fits, which are 95% intervals, do not overlap. Moreover, the separate data points fitted have a longer fitted decay time.

The lower T_2 value for time domain averaged echoes is easily explained. Assume there is a shift in earth's magnetic field strength and thus Larmor frequency. At the start of an experiment, excitation and Larmor frequency are set to match exactly. Over time when averaging, averaged echo intensity decreases as absolute phase gradually changes. Especially for echoes further away from the initial 90°pulse, this becomes a bigger problem. Therefore, time domain averaged fits of T_2 will always produce lower values of T_2 compared to fits of individual measurements' FFT peak values.

When performing a CPMG sequence, each subsequent echo decays with T_2^*. Using the FWHM as explained in A.4, T_2^* can be determined. For the CPMG sequence used in this section both the average values of T_2^* as function of echo number for all separate measurements, as well as T_2^* of the time domain average of all measurements is displayed in table 7.2. Clearly, average T_2^* values are roughly 50% higher than the value of T_2^* for the time domain

Table 7.2: T_2^* values of each echo in the CPMG sequence used in this section. Table shows averaged T_2^* values for all individual measurements (average T_2^*) as well as T_2^* for each echo in the time domain averaged sequence as shown in figure 7.5.

Echo number	1	2	3	4	5	6	7	8	9	10
T_2^* averaged	41	42	42	43	42	42	43	43	43	42
Average T_2^*	59	62	62	63	63	64	64	63	62	68

average. This indicates that indeed there are changes in Larmor frequency during averaging, which decrease T_2^* of the time domain average.

7.3 Galden

Galden is a fluorinated inert liquid (PerFluorPolyEther) typically used in heating systems for its high thermal conductivity, heat capacity and thermal stability. Because it is fluorinated, the chemical element responsible for the NMR signal is ^{19}F instead of ^{1}H used so far. Therefore, it will have a different Larmor frequency. Because the resonance frequency of the sample coils can be varied, both water and Galden can be measured with the same setup. Moreover, since there are two sample coils, a sample of each liquid can be inserted into one of the sample coils. By measuring both samples simultaneously, the gyromagnetic ratio of Galden can be determined.

A sample of $100mL$ of each fluid is inserted into one of coils used in the bucking coil configuration. First, the non-adiabatic FID is used and the Larmor frequency of both samples is roughly determined. The Resonance frequency of the coils is then set in between these two frequencies such that the sensitivity for both frequencies is roughly equal. To be able to excite both frequencies, an adiabatic measurement was made using a short duration, high amplitude pulse.[1] The resulting spectrum of a measurement made at this setting is shown in figure 7.7.

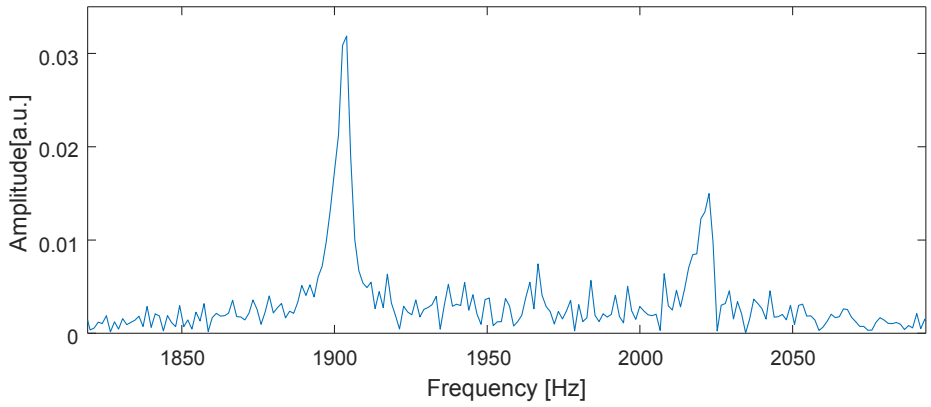

Figure 7.7: non zero-padded frequency spectrum of a Non-adiabatic FID made with a sample of Galden and water inserted into each of the two bucking coils.

The spectral peak of water sample can be found around 2023Hz and the peak of Galden around $1904Hz$. Average shift in peak frequency of Galden compared to distilled water for an average of 16 measurements is $-5866ppm$. Using the gyromagnetic ratio for water of $42.577MHz/T$, gyromagnetic ratio of Galden is $40.08MHz/T$.

For Galden, T_2 is determined using varying polarization time and fitting method described in section 7.2. Varying T_{90} is not used because T_2 of Galden is much shorter than that of water, and a minimum T_{90} is required, which result in few data points at low times.

[1] As can be seen from equation 1.19, rotation angle θ can be achieved by varying both pulse amplitude as well as duration. Following the same analysis as presented in section A.3, using a short pulse can be seen as multiplying the time domain signal with a rectangular function. In frequency domain this becomes a sinc function, whose width is inversely proportional to the pulse duration. Shorter pulses thus excite a wider frequency bandwidth.

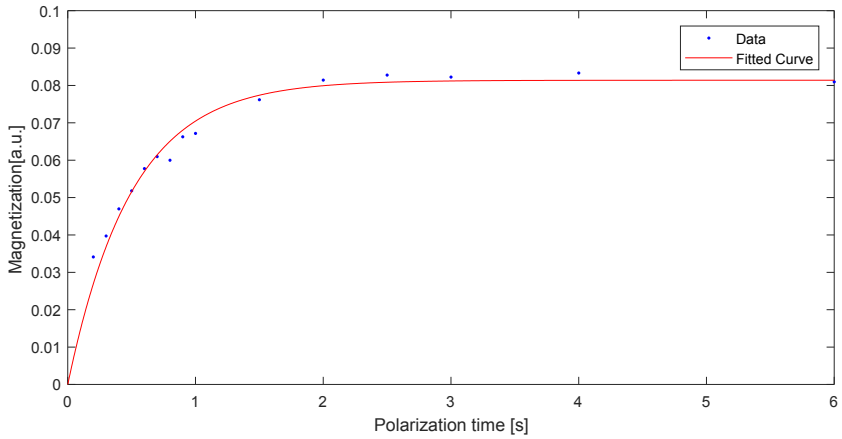

Figure 7.8: T_1 fit of Galden using a varying polarization time.

The T_1 value of Galden using the exponential fit as shown in figure 7.8 equals $T_1 = 0.49 \pm 0.05\ s$.

Similar to the T_2 decay fit for water given in 7.2, a CPMG sequence is used with 5 echoes with an echo time of 250ms. 32 averages were used to measure the CPMG sequence. In figure 7.9, both raw data points and fitted curve is shown.

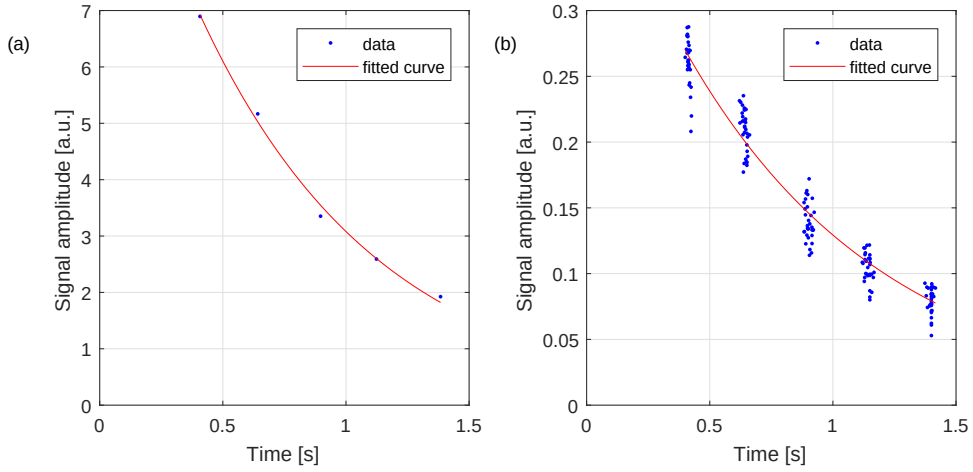

Figure 7.9: T_2 fit of a CPMG sequence for Galden. (a): Time domain averaged data. (b): separate measurements.

The fitted T_2 time of this measurement is 0.8 ± 0.2 seconds for the separate values, and 0.7 ± 0.1 seconds for time domain averaged values.

7.4 Long-term Earth's Magnetic Field Strength Variations

We have already seen hints of temporal instability in the earth's magnetic field in several measurements in this chapter. For example, the measurement shown in figure 7.5, of which the fitted T_2 results are displayed in table 7.1, shows lower T_2 values for time domain averaged values compared to individual measurements. To investigate this and conclude whether or not temporal instability really is the main cause, several long-term measurement series have been performed.

A non-adiabatic FID does not depend on a pulse sequence for excitation. This is of use when we want to study the earth's magnetic field strength over time without having excitation frequency influence our results. We perform an FID every minute, and plot the resulting peak frequency as function of time using the FFT. The detection coil's axis was aligned horizontal such that the vertical component of earth's magnetic field is measured. The first time this measurement has been performed, it was ran over the period of six hours inside an office between 10:00 and 16:00. The results of this measurement are shown in blue in figure 7.10.

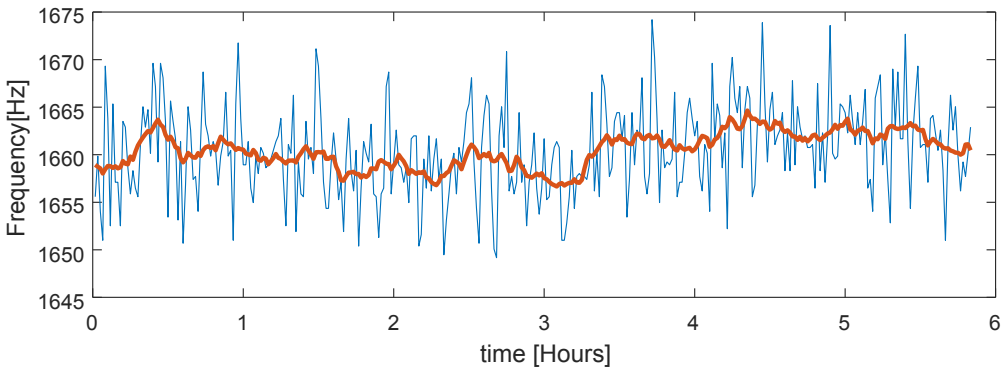

Figure 7.10: Peak frequency of a non-adiabatic FID over a period of six hours. In blue, raw data is shown, whereas in red the same data is shown but filtered with a 15 minute moving average filter

The FID peak frequency over a period of six hours has a bandwidth of $25Hz$. Moreover, field frequency variation has both fast and slow components. Since the measurement was made in an office environment, fast components could be due to metallic objects moving around in the building or switching of electrical appliances. Due to low sampling rate, digital filters cannot be easily used to spatially filter the data such that slow variants become visible. However, a moving average filter can be used. This filtered data is shown red in figure 7.10.

When the data is filtered with the moving average of 15 minutes, slow variations still show a bandwidth of $10Hz$. Since this measurement was made during daytime, a second measurement was started with a period of four days, starting on Thursday afternoon 16:30. The results of this measurement are shown in figure 7.11, where a 30 minute moving average filter has been used.

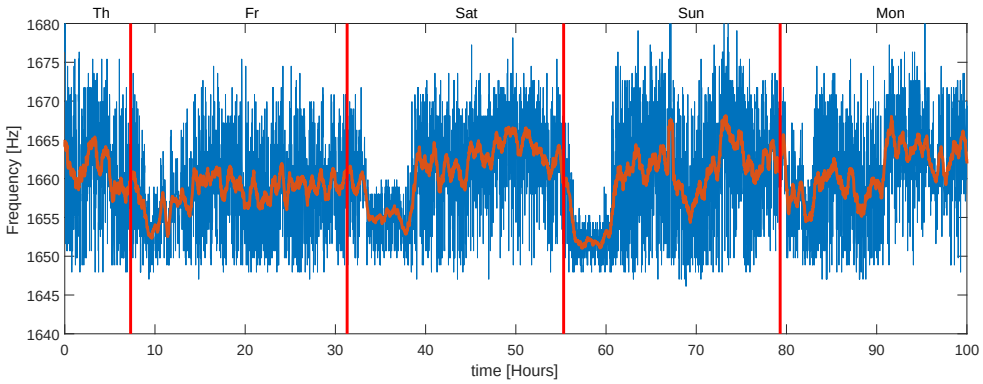

Figure 7.11: peak frequency of a non-adiabatic FID over a period of four days. In blue, raw data is shown, whereas in red the same data is shown but filtered with a 30 minute moving average filter. The vertical red lines indicate 24:00 midnight.

Inspecting figure 7.11 shows that Larmor frequency and thus earth's magnetic field strength varies with roughly the same bandwidth across several days, at nearly $15Hz$. Indicated by the vertical red lines 24:00 is shown. As can be seen, during nighttime Larmor frequency is significantly lower than during daytime. Moreover, the second and third night show a much clearer and lower amount of variation in Larmor frequency. Since the measurement was started on Thursday afternoon, the first night is that from Thursday to Friday. During this time, office equipment, HVAC installations and other measurement setups are most likely switched on, while this is not true for the nights from Friday to Saturday and Saturday to Sunday.

7.5 Averaging to Improve SNR

In appendix A.1 the effects of averaging on SNR are discussed. The conclusion is that when a measurement is repeated N times, SNR is improved by$\sqrt{N}$. This is a theoretical assumption, which only works when all boundary conditions of the experiment remain constant. However, we have already seen in several measurements averaged over short times, as well as long term measurements in section 7.4, that earth's magnetic field strength and thereby Larmor frequency are not constant. This means that theoretical improvement of SNR with$\sqrt{N}$ cannot be achieved.

To investigate SNR improvement, the data review tab of the GUI as shown in figure 6.2, offers functionality to plot SNR as function of averages[1]. An example of the output window this produces is shown in figure 7.12. In figure 7.12 (a) SNR per echo is shown for all individual measurements. In figure 7.12 (b), cumulative SNR of all echoes is shown as they are averaged over time, with the horizontal axis displaying $\sqrt{N}$ such that the resulting lines should be straight. The measurement used for this example is that of the CPMG sequence shown in figure 7.5. Inspecting cumulative SNR as function of number of averages per echo,

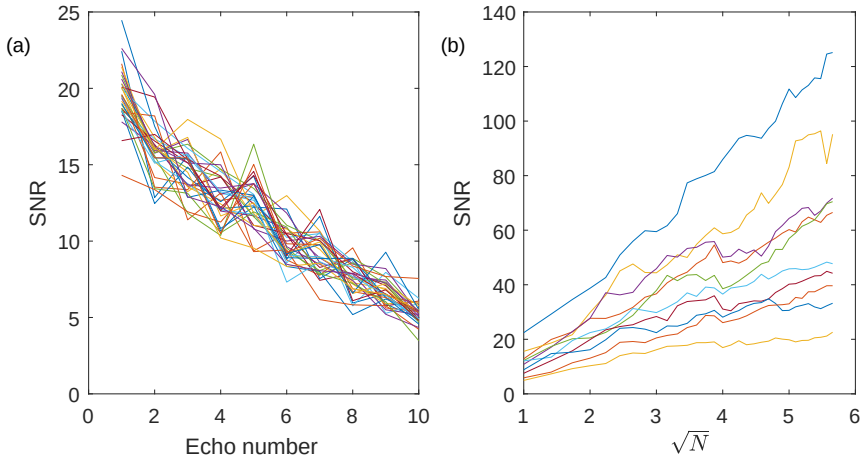

Figure 7.12: SNR as function of the echo number for the measurement shown in figure 7.5. (a): SNR per Echo, per measurement. (b): Cumulative SNR as function of the number of averages per echo.

shows that SNR does not monotonically increase for all echoes. This indicates that the signal changes from measurement to measurement. Moreover, in this specific measurements series, SNR does not seem to increase with the same rate for all echoes.

If we assume that SNR improves with N^A, where A is a positive fraction, we can determined how close this power is to 1/2. Since the measurement used in figure 7.12 uses only 32 averages, we perform a new CPMG measurement with 21 echoes spaced at $T_{Echo} = 250ms$, averaged 128 times. SNR per echo and SNR of the time-domain averaged signal are shown in figure 7.13. Fitting all traces in figure 7.13 (b) to $y(x) = Ax^B$ produces the values shown in 7.3. Missing echo numbers were omitted if the adjusted R^2 was smaller than 0.9. As can be

Table 7.3: fitted values of the equation $y(x) = Ax^b$ to the cumulative SNR as function of the number of averages, x, shown in figure 7.13.

Echo number	1	2	4	5	6	8	9	10	11	12	15	16
A	21.5	19.5	15.4	11.2	8.1	6.3	6.3	5.7	3.0	3.4	2.4	3.7
B	0.38	0.36	0.33	0.36	0.48	0.40	0.37	0.37	0.45	0.43	0.43	0.31

[1]To see how Matlab computes SNR, please refer to [34].

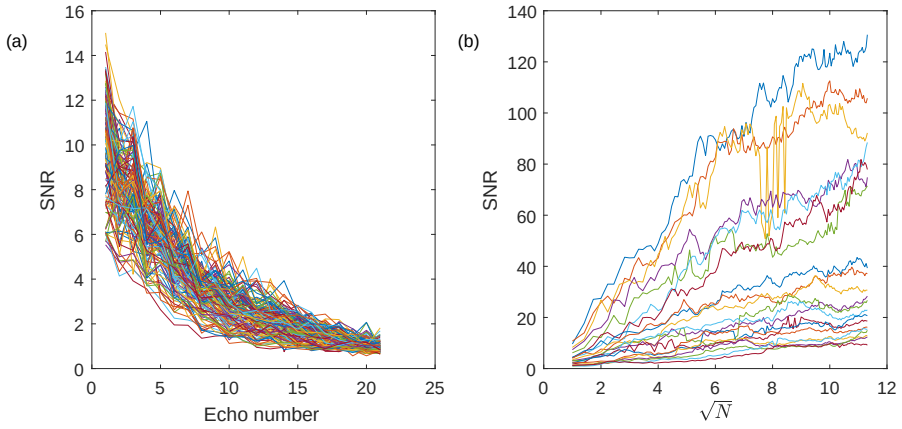

Figure 7.13: SNR on linear scale for a CPMG sequence with 21 echoes. (a): SNR per echo, per measurement. (b): Cumulative SNR per echo as function of the number of averages.

seen from 7.3, the value of B is lower than 0.5 for all echoes. Its mean is 0.38 which means that SNR does not increase as$\sqrt{N}$ but as $N^{0.38}$. This further illustrates the effects temporal instabilities have on averaging.
In addition, we can investigate the time-domain averaged signal of the non-adiabatic FID measured for a duration of four days as shown in figure 7.11 to estimate the bandwidth across which FIDs are produced. We know that starting phase of the FID is constant throughout all processes and equal to zero. Over time, dephasing of the FID at differing frequencies will cause time-domain averaged intensity to decrease once we have sample for a duration $t > 1/\Delta F$, where ΔF is the bandwidth of all FIDs. This is effectively our new T_2^* time. The time-domain averaged signal spanning four days is shown in figure 7.14. As can be seen

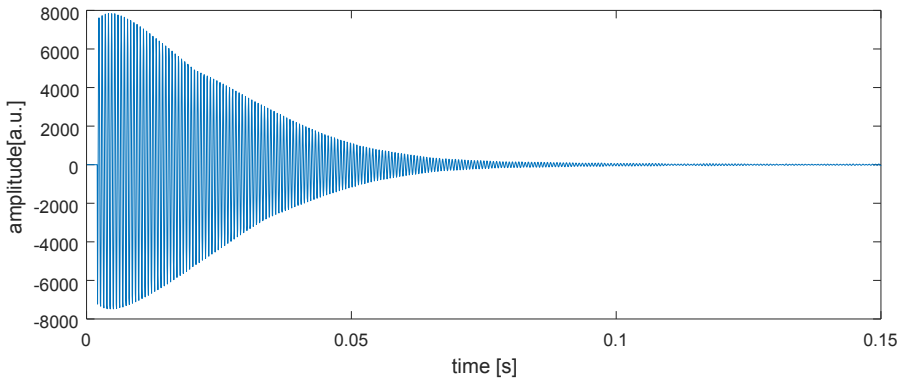

Figure 7.14: Time-domain averaged non-adiabatic FID of the long-term measurement shown in figure 7.11.

from this measurement, apparent T_2^* time has been reduced to roughly 0.05 seconds. This corresponds to a spectral bandwidth of $20Hz$, which is in agreement to the actual bandwidth observed in section 7.4.

Conclusion

A hardware platform has been constructed for a cost price of roughly €440[1]. This platform can measure free induction decay, spin-echo as well as CPMG sequences using both adiabatic as well as non-adiabatic transitions in the earth's magnetic field. Hardware control for the setup is a Teensy, which is a module part of the Arduino family of microcontrollers. Furthermore, usage of the open-source Arduino platform allows anybody to inspect and improve upon the source-code running the hardware platform. Finally, power supplies have been used which allow a wide range of input voltages to be used to power the platform. This allows the setup to be used outdoors, powered from batteries.

A GUI has been developed in Matlab to perform all interfacing of the hardware platform to a computer. The GUI has been compiled into a standalone executable that can run on any computer and its source-code can be inspected using a text editor. Several features are integrated into the user interface as well as hardware to make operation of the setup easier even for users without experience on NMR. These include automatic suggestion of measurement parameters as well as the ability to connect fluxgate magnetometers to monitor earth's magnetic field strength.

Measurements have been performed to verify design compliance. Main results of these measurements are the following.

1. Bandpass filter response of the amplifier is in accordance with the design with variations mainly due to component tolerances.

2. Implementation of the programmable gain amplifier to optimize digitization capabilities of the Analog-to-Digital Converter (ADC) show good linearity across the range of amplification factors.

3. A bucking coil configuration has been implemented to gain a reduction of 227 times the original environmental noise inside a typical office environment. This decreases total noise level by $39dB$ which without, makes obtaining measurements with sufficient SNR impossible. Moreover, the angular dependency of noise reduction has been measured.

To show the capabilities of the setup, samples of water and Galden have been measured. T_1 and T_2 times were measured of both samples using CPMG sequences. T_1 time of water was determined using a variable polarization time but constant 90°pulse delay, as well as using a constant polarization time but variable 90°degree pulse delay. These two different measurement result give equal values, within measurement inaccuracy. Both T_1 and T_2 values, which vary between 2.69 and 3.1 seconds, match literature values [21].

The measured signal amplitude of a sample of $100mL$ of de-mineralized water using a CPMG sequence is in good accordance with the theoretically predicted value using design specifications of the setup.

For Galden, which is a fluorinated liquid, the ability of performing basic spectroscopy using the setup is shown. Gyromagnetic ratio of Galden has been found to be $40.08MHz/T$,

which is in good accordance with literature values[2] [44]. T_2 of Galden was found to be $(0.8 \pm 0.2)\,s$. T_1 was found to be $(0.49 \pm 0.05)\,s$. These values are in contradiction with the statement in section 1.5 that in general $T_2 > T_1$. Systems in which $T_2 > T_1$ are rare and only occur when relaxation is mainly transversal and the shielding tensor is antisymmetric [54]. This result is thus not something that would normally be expected from typical materials, but it is certainly not impossible.

To conclude, the setup has been successfully used to monitor earth's magnetic field strength over a window of several days. Temporal instabilities in the earth's magnetic field strength have shown to have significant influence on effective decay times when averaging multiple measurements especially over a longer period of time. Instead of the theoretical improvement in SNR following a $\sqrt{N}$ dependency, it showed a dependency ranging from $N^{0.31}$ to $N^{0.48}$. This has been found to be due to temporal instabilities in the earth's magnetic field strength and therefore Larmor frequency of a sample.

[1] An expanded summary of the total cost price of the setup is given in appendix E

[2] See also table 1.1

Discussion and Outlook

The current hardware is capable of performing all experiments required in the goal of this project. However, several improvements could be made to increase setup performance further. Some of these improvements are optional, and would not add core-functionality, while others would significantly increase usability and performance. A list of the main improvements is given in the following overview.

1. Receiver dead-time has been reduced from $80ms$ from the first amplifier and coil revision to only $40ms$. However, improvements to this can be made if better damping mechanisms are used. An example of this is active feedback of the coil response during switching such as described in [45].

2. Currently, eight capacitors can be switched to form the total capacitance used to make the detection coils resonant. The spectral resolution this provides is roughly $20Hz$. While this is sufficient for applications shown in this report, when imaging is to be performed it is rather low. If a second ADG714 would be used, double the amount of capacitors can be switched which greatly increases spectral resolution available for resonance tuning.

3. The current hardware offers an additional input to connect several types of sensors. This has been used throughout the work to connect a fluxgate magnetometer to estimate Larmor frequency. To decrease measurement setup time and increase usability, a fluxgate magnetometer can also be integrated onto the main board. An example of such an IC is the Freescale FXOS8700. It is possible to program a startup sequence onto the Teensy which first reads this sensor, and automatically suggests the user with Larmor frequency close to the true Larmor frequency.

4. The pulse transmitter currently implemented using the AD9850 can be programmed into a DAC library onboard the Teensy to reduce part-count. Moreover, it can increase flexibility when also soft-pulses of random shape can be used instead of the pure sinusoids used at the moment.

5. The polarization coil used produces a field of only $6.9mT$ on average across its center axis. However, the sample coils do not take up the entire space inside the polarization coil. Firstly, the coil could be wound using more than three layers, to increase conversion efficiency as shown in figure 2.8. This will however require a careful re-examination of the polarizer to limit back EMF, or increase the maximum back EMF allowed. Secondly, the coil could be wound in a rectangular shape instead of in a circular shape such that effectively the field inside it will increase in intensity while keeping current equal.

6. No polarization current is measured at this moment. This means that when the coil heats up, current will decrease which in turn decreases signal intensity. This has a neg-

ative effect on measurement results and can be prevented when the current is actively measured.

Unfortunately, not all goals with respect to the open-source character of the project have been achieved. This mainly concerns the GUI, which has been developed in Matlab. Matlab source code may be available and compiled into a stand-along executable, however compiling it by a user is impossible. Therefore, no changes can be made by the user to the source code. Some improvements concerning the GUI are:

1. Port the Matlab GUI to open-source software such as Octave. This is an open-source software package similar to Matlab, but developed by individuals and covered by the GNU open-source license.

2. Publish all design documents, descriptions and software source code on a website for everybody to access.

In addition, the hardware has been designed to be assembled by anybody with reasonable soldering skills. However, surface mounted components have been used that make it hard if not impossible for somebody who does not have experience. Therefore, it would be good to produce the electronics and sell them for cost price for anybody interested. Likewise, the sample coils favor a similar treatment.

Finally, additional functionality can be added to the setup. As has been briefly mentioned in 4.2, three prototype gradient drivers have been implemented on the polarization current switch board. These could be used to power gradient coils that can provide gradients across the sample, allowing imaging to be performed using the setup. During this work, there was not enough time to finish these gradient drivers. However, with some more time they could be made to work, which greatly increases the applicability of the setup.

SNR improvement as function of the number of averages does not show exact $\sqrt{N}$ improvement when averaging N times. This has been found to be due to temporal instabilities in earth's magnetic field strength. To improve upon this, a possibility would be to compensate resonance frequency of the coils and excitation frequency while a series of measurements is being performed. This option has been employed by Qiu Long-Qing et. al. [32] where they showed the employment of Time-domain Frequency Correction (TFC) to extend T_2^* almost up to T_2 even with temporal instabilities. Using this method with a fixed reference sample, the ability of performing spectroscopy with EFNMR is increased.

Appendix A: Additional Theory

This chapter contains additional theory which is not per se required for the understanding of NMR, EFNMR, or the setup itself. However, these topic do offer additional insight into a better understanding in some of the principles used in the setup. Therefore, they have been placed in the appendix.

The first topic in this appendix is averaging. This section explains how SNR is improved by a factor $\sqrt{N}$ when a measurement is repeated N times. Secondly, we explain how a conductor can shield the setup from electromagnetic radiation by the skin effect. Thirdly, we will explain the basics of Fourier Transformations and the generalized FFT as well as sampling and windowing. To conclude this appendix, we investigate how T_2^* relaxation influences spectral width of NMR signals.

A.1 Averaging

In an EFNMR experiment, several noise sources degrade SNR of a measurement. By repeating the experiment and averaging the results, SNR can be improved. To see why averaging works, an analysis of the SNR is performed based on the assumption that the time signal $s(t)$, with power, S , remains constant over time.

We first define the expectation value of a signal x as $E[x]$. The signal's variance, σ^2 , equals the expectation value of the squared deviation from its mean, $\mu = E[x]$. In equation form, the mean μ of a signal is

$$\mu = E[x] = \int_{-\infty}^{\infty} xP(x)\,dx \ , \tag{A.1}$$

where $P(x)$ is the probability density function which must fulfill the following condition

$$\int_{-\infty}^{\infty} P(x)\,dx = 1 \ . \tag{A.2}$$

Variance, σ^2 , is defined as

$$\sigma^2 = E\left[(x-\mu)^2\right] \ . \tag{A.3}$$

Assume an NMR signal is composed of true signal, $s(t)$, with added stochastic noise, $n(t)$. By the stochastic nature of noise, it has mean $E[n] = 0$ and variance σ^2 . Furthermore, we assume the noise is uncorrelated to the signal

$$E[s(t)\,n(t)] = E[s(t)]\,E[n(t)] = E[s(t)]\,0 = 0 \ , \tag{A.4}$$

as well as uncorrelated with itself

$$E\left[(n(t))^2\right] = E[n(t)]\,E[n(t)] = 0 \ . \tag{A.5}$$

The power, S , of signal $s(t)$ equals

$$S = \int_o^T E|s(t)|^2 dt \ . \tag{A.6}$$

SNR is equal to the ratio of signal power, to variance of the noise

$$SNR = \frac{S}{\sigma} = \frac{S}{\sqrt{\sigma^2}} \ . \tag{A.7}$$

The experiment is now repeated N times. Since the signal power remains constant, the total power of N subsequent measurement of $s(t)$ is simply NS , such that the average power is also S . The variance of the noise, averaged over N measurements varies as

$$\sigma^2(N) = \sigma^2\left(\frac{1}{N}\sum_{i=1}^{N} n_i(t)\right) \tag{A.8}$$

Expanding gives

$$\sigma^2(N) = E\left[\left(\left(\frac{1}{N}\sum_{i=1}^{N} n_i(t)\right) - 0\right)^2\right] = \frac{1}{N^2}E\left[\sum_{i=1}^{N}\sum_{j=1}^{N} n_i(t)\, n_j(t)\right] \tag{A.9}$$

Since noise, $n_i(t)$, is random and uncorrelated with itself, ($E[n(t)]\,E[n(t)] =$), we see that only terms where $i = j$ contribute to the total variance and we conclude that

$$\sigma^2(N) = \frac{1}{N^2}N\sigma^2 = \frac{\sigma^2}{N} \tag{A.10}$$

The SNR for N averages thus scales as

$$\frac{S}{\sqrt{\sigma^2/N}} = \sqrt{N}SNR \tag{A.11}$$

It thus makes sense to average an NMR signal to increase SNR, as it improves by $\sqrt{N}$ when averaging N times.

A.2 Shielding and Skin Depth

A conducting material placed around the sample coil can increase SNR of a measurement by shielding the coil from environmental noise. Inside a conductor, the intensity of externally imposed electromagnetic fields decay exponentially along the direction of the conductor following Beer-Lambert law. To be exact, electromagnetic fields decay as [19]

$$I(z,t) = I_0 e^{i(kz-\omega t)} \ , \tag{A.12}$$

where z is the distance from the surface of the conductor and k the wavenumber. The wavenumber is given by the dispersion relation

$$k^2 = \mu\epsilon\omega^2 + i\mu\sigma\omega \ , \tag{A.13}$$

where σ is the conductivity of the material, ω the radial frequency, ϵ the electric permittivity of the conductor and μ its magnetic permeability. At low frequencies where EFNMR operates, in a good conductor typically $\sigma \gg \epsilon\omega$ and the equation reduces to

$$k \cong \sqrt{i\mu\sigma\omega} \tag{A.14}$$

A commonly used parameter to characterize the damping properties of a conductor is the skin depth δ. It is defined where the intensity of externally imposed electromagnetic fields has decreased by $1/e$. Substituting the solution for wavenumber k into equation A.12 we can see

$$\delta = \sqrt{\frac{2}{\mu\sigma\omega}} = \sqrt{\frac{1}{\mu\sigma\pi f}} \ . \tag{A.15}$$

A.3 Fast Fourier Transform, Sampling and NMR Spectra

An NMR signal typically does not contain only spectral components at exactly Larmor frequency. Only if the external magnetic field strength is exactly constant throughout the sample and all participating elements precess at exactly Larmor frequency, this is possible. When small gradients are present, this does not hold since they spread the spectral content across a larger spectral bandwidth. In fact, this is the principle used in MRI, which uses magnetic gradient fields to produce a position dependent Larmor frequency.

Moreover, due to the various noise sources, NMR signals contain frequencies across a much wider bandwidth than only the Larmor frequency. If an NMR signal is evaluated in time domain, all signals spread across the spectrum are used to define an amplitude, while only the amplitude of a single frequency is desired. Therefore, the Fourier transform is used to analyze the recorded data. The Fourier transform transforms a signal in time domain, to a signal in frequency domain producing a frequency spectrum.

Fast Fourier transform

The Fourier transform, $\mathcal{F}$, of a time continuous signal, $f(t)$, is defined as [26]

$$\mathcal{F}\{f(t)\} = F(\omega) = \int_{-\infty}^{\infty} f(t)\, e^{-i\omega t} dt \,. \tag{A.16}$$

To illustrate this with an example, the time domain signals $f_1(t) = \frac{1}{2}e^{-it}$ and $f_2(t) = e^{-it} + 2e^{-2it}$ and the absolute value of their Fourier transforms are $F(f_1(t)) = F_1(\omega) = \frac{1}{2}\delta(\omega - 1)$, $F(f_2(t)) = F_2(\omega) = (\delta(\omega - 1) + 2\delta(\omega - 2))$ respectively, as shown in figure A.1.

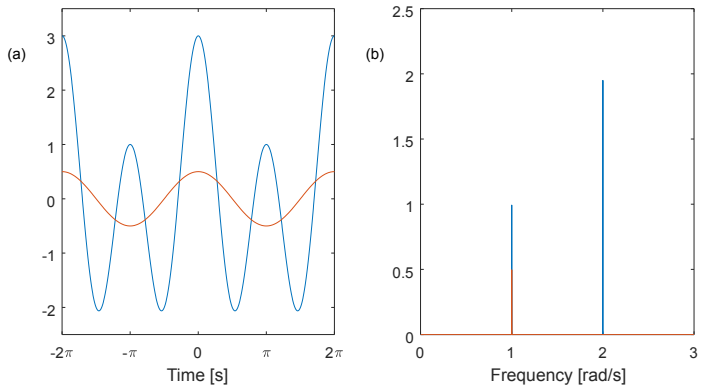

Figure A.1: Time domain signal amplitude as function of time (a) and Fourier spectrum as function of frequency (b) for the functions $f_1(t) = \frac{1}{2}e^{-it}$ (red) and $f_2(t) = e^{-it} + 2e^{-2it}$ (blue).

A stationary oscillating wave in time domain produces a single well-defined spike in frequency domain.

A signal, x, is sampled at sampling frequency, F_s, with sampling period t_s, in an even number of $2n$ samples given by

$$x_n = (x_0, x_1, , x_{n-1}) \,. \tag{A.17}$$

The discretized signal produces discretized, complex-valued frequency components, as given by the Discrete Fourier Transform (DFT), $y_m = F(x(n))$ [22]

$$y_m = \sum_{k=0}^{n-1} x_k e^{-\frac{2\pi i m k}{n}} \,. \tag{A.18}$$

Realizing that the DFT is antisymmetric for odd and even values of k, the concept of the FFT is defined. Using the symmetry properties only half the coefficients, the odd or the even, need to be calculated. In Matlab the command $fft\left(x, N_{FFT}\right)$ calculates this Fast Fourier Transform and thereby generates a doubled sided spectrum consisting of both the negative and positive frequencies with N_{FFT} points of the signal $f\left(x\right)$. The frequency spectrum is then given by the range $\frac{Fs}{N_{FFT}} * \left[0, 1, , \frac{N_{FFT}}{2}\right]$.

Sampling, zero-padding and zero crossing rate

The Nyquist-Shannon theorem [48] states that a signal sampled with a sample rate two times higher than the maximum frequency, F_{max}, contained in the signal, the original time-domain signal can always be obtained from the frequency spectrum calculated by the Fourier transform. In that sense, the Fourier transform is exact as long as

$$F_s > 2F_{max} \ . \tag{A.19}$$

If this condition is not satisfied, aliasing occurs. Aliasing both degrades signal quality, and can lead to false data. To assure this will not happen, a signal is low pass filtered before being sampled such that the inequality in equation A.19 is satisfied.

Because the FFT is a discrete operation, it yields a discrete spectrum. The number of separate frequency bins directly influence spectral resolution. Similar to not being able to determine a body's position and velocity simultaneously, a large acquisition time, T_{acq}, is needed to determine the exact frequency of a signal. The spectral resolution depends solely on the total acquisition time as

$$\delta f = \frac{1}{T_{acq}} = \frac{1}{N_{FFT} t_s} = \frac{F_s}{N_{FFT}} \ . \tag{A.20}$$

If after FFT, an NMR signal has insufficient spectral resolution, zeros can be added to it to increase its length. This operation known as zero-padding increases the spectral resolution, making it easier to resolve multiple frequencies in a spectrum, without changing its physical interpretation.

As alternative to the FFT, Larmor frequency can also be determined electronically using the zero-crossing frequency. When it is implemented using a comparator and counter, no additional computational resources are required. Therefore, it is most commonly used in the PPM, where a simple display of the Larmor frequency and thereby earth's magnetic field strength is the desired quantity. However, accuracy and reliability of the zero-crossing detection is limited by construction, since it cannot distinguish between signal and noise, which influences the periodicity of zero-crossing.

Windowing

The convolution, $h\left(x\right)$, of two functions $f\left(x\right)$ and $g\left(x\right)$ is defined as

$$h\left(x\right) = \left(f * g\right)\left(x\right) = \int_{-\infty}^{\infty} f\left(y\right) g\left(x - y\right) dy \ . \tag{A.21}$$

The Fourier transform has the convolution property, that in time domain a convolution is equal to a multiplication in frequency domain. This property is given by the convolution theorem and in equation form it reads

$$\mathcal{F}\left\{f * g\right\} = F\left\{f\right\} F\left\{g\right\} \ . \tag{A.22}$$

An EFNMR signal unequal to zero at the edges of the sampling domain introduces a ripple in frequency domain. This is because the FFT operates on time discontinuous signals on the interval $[0, N-1]$. This can be seen as a convolution of the signal on the infinite interval, with a rectangular function. Since $F\left\{rect\left(\frac{t}{\tau}\right)\right\} = \tau sinc\left(\frac{\omega\tau}{2}\right)$, the time discrete nature of the FFT gives a sinc-shaped ripple across the spectrum.

To suppress ripple, EFNMR signal is multiplied with a windowing function, forcing the edges to be zero. Since this is effectively a convolution of the original signal with the spectrum of the windowing function, therefore, the spectrum itself is affected. Depending on the windowing function, side lobe suppression, main lobe amplitude and main lobe width are all affected. An overview of several window function is displayed in figure A.2.

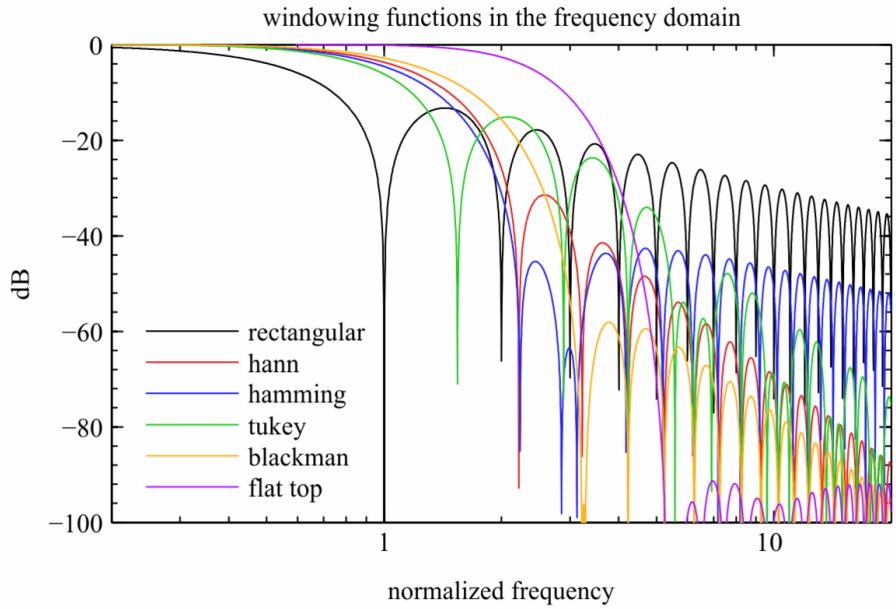

Figure A.2: normalized transfer function of multiple window functions that can be used to filter the signal before calculating the FFT as function of normalized frequency [31].

For time discrete signals containing mostly a single frequency component, the Hanning window is often used. It gives good side lobe rejection while maintaining peak amplitude of the signal at minimum line width increase. It is defined on the interval $n \in [0, N-1]$ as

$$w(n) = 0.5\left[1 - cos\left(\frac{2\pi n}{N-1}\right)\right] \tag{A.23}$$

The Hanning windowing function also scales total energy contained in the signal. To correct for this, the windowed time domain EFNMR signal is normalized with the inverse mean of the window function magnitude before FFT.

Moreover, to absorb differences in the amplitude of spectral components for signals with differing lengths such as the FID and echoes, the signal is also normalized to its length. This absorbs the effects of changes in N_{FFT} throughout several measurements. If zero padding is employed in the calculation of the Fourier transform, the signal should be windowed first before zero padding to provide a continuous transition to the trailing zeros. If this is not done, spectral leakage will occur and resulting spectral amplitudes will be incorrect.

A.4 NMR Spectrum Line Width

T_2^* Relaxation influences the spectral width of EFNMR signals. Using this spectral width, we can determine T_2^*. To do so, we need to analyze how these two are linked.

We realize that T_2^* relaxation is an exponentially decaying process while the NMR signal itself oscillates at Larmor Frequency ω_0. The signal thus looks like

$$f(t) = e^{i\omega_0 t} e^{-t/T_2^*} \ . \tag{A.24}$$

When split by FFT to its monochromatic components of frequency ω, it yields a complex spectrum with amplitude $F(\omega)$ equal to

$$F(\omega) = \frac{-1}{\sqrt{2\pi}} \left\{ \frac{1}{i(\omega_0 - \omega) - 1/T_2^*} - \frac{1}{i(\omega_0 + \omega) + 1/T_2^*} \right\} \ . \tag{A.25}$$

Due to this reason, there are frequency components both above and below Larmor frequency ω_0, if $T_2 < \infty$. Since $|\omega_0 + \omega| \gg |\omega_0 - \omega|$, the second term in equation A.25 can be dropped. Moreover, to simplify, assume $f(0) = 1$ and take the absolute value to find the (normalized) spectral density function, $I(\omega)$

$$I(\omega) = \frac{1/T_2^*}{(\omega_0 - \omega)^2 + (1/T_2^*)^{\ 2}} \ , \tag{A.26}$$

which is a Lorentzian. If we consider the Half Width at Half Maximum (HWHM) we find

$$I(\omega) = \frac{I(\omega_0)}{2T_2} \tag{A.27}$$

$$(\omega_0 - \omega)^2 + (1/T_2^{*\ })^{\ 2} = \frac{2}{(T_2^*)^2} \tag{A.28}$$

Which can be simplified to find

$$|\omega_0 - \omega| = 1/T_2^* \tag{A.29}$$

The FWHM is thus equal to

$$FWHM = 2|\omega_0 - \omega| = \frac{2}{T_2^*} \ . \tag{A.30}$$

This gives for T_2^*

$$T_2^* = \frac{2}{FWHM} \ , \tag{A.31}$$

where FWHM is in radian. NMR spectrum is thus composed of Lorentzian peaks whose FWHM is related to decay time T_2^*. Higher relaxation times thus result in more well-defined peaks in the spectrum of the NMR signal.

Appendix B: Electronics development

Between the first and final version of the amplifier and coils, multiple iterations have been tried and tested. Since development of both the hardware and software of the setup as presented has been a primary time consumption during the research, an overview of key improvements is given to show the advancements.

B.1 Signal Amplifier and Detection Coil, version 1.

At the start of this project, some electronics were already present. Both the signal amplifier as well as polarization current switch were inspired on a paper by Carl A. Michal [40]. These electronics were simplistic in both their design and implementation. Despite being suboptimal, the polarization current switch worked flawless and was only replaced towards the end of this project by the polarizer board described in section 4.2.

The design of the signal amplifier V1 can be seen in figure B.1. The amplifier comprised

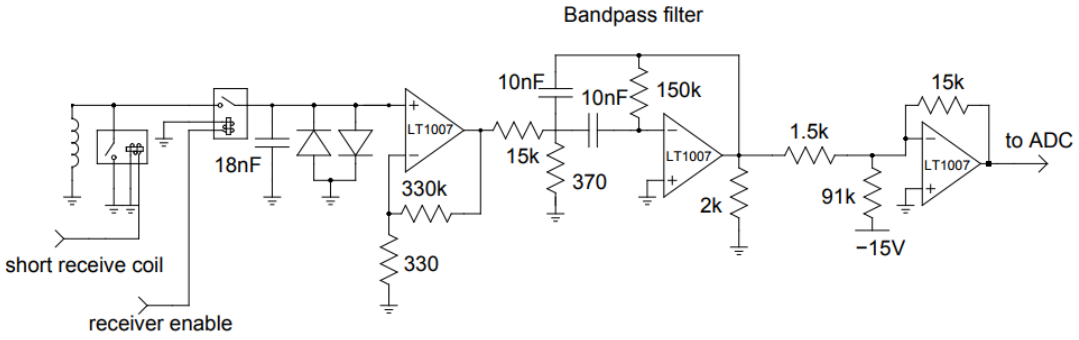

Figure B.1: Schematic of the input amplifier from the paper of C.A. Michal.

of three stages. The first stage is an op-amp in inverting configuration with fixed gain of 1001. The second stage comprises a single infinite gain multiple-feedback bandpass filter centered at Larmor frequency, which also amplifies the signal a factor 20. The third and final stage features a single op-amp, boosting the signal another factor 10 as well as provide level shifting for the ADC in the Arduino Uno, which was used at the beginning. Total gain of the amplifier is fixed at 200.000.

Although all op-amps (Linear Technologies LT1007) were selected for low noise $\left(V_{n,amp} = \ 3.8nV\sqrt{Hz}\right)$, feedback resistors also add Johnson noise. More specifically, the first stage has total voltage noise density, $V_{n,inv}$, equal to

$$V_{n,inv} = \sqrt{4k_BT\left(\frac{R_1R_2}{R_1+R_2}\right)} + V_{n,amp}, \tag{B.1}$$

where $R_2 = 330.000\Omega$ and $R_1 = 330\Omega$. Entering the values of R_1 and R_2, we find

$$V_{n,inv} = \sqrt{4k_BT\,(329.7)} + 3.8 \times 10^{-9} = 6.2 \times 10^{-9} V/\sqrt{Hz}. \tag{B.2}$$

As can be seen from equation B.2, thermal voltage noise due to the amplifier is over four times higher than that for the final amplifier using the AD8428 which has voltage noise of only $1.5nV/\sqrt{Hz}$.

The first detection coil build was also inspired on the same paper by Michal. The coil is wound from copper wire, on an acrylic pipe with inner diameter of $100mm$ and winding

length of $100mm$. The coil's AC-resistance at $2kHz$, and its inductance at $42Hz$, measured using a Hioki 3532-50 RLC tester. Due to the coil's large dimensions, it fits a sample of $750mL$ of water inside. An overview of the main coil parameters is given in table B.1.

Table B.1: Overview of coil parameters of the single detection coil inspired on the paper of Carl A. Michal [40]

Coil parameter	Measured value
Wire diameter mm	0.34
Number of layers N_l	10
Number of windings per layer N_c	294
DC resistance Ω	226
AC impedance at $2kHz$	229
Inductance mH	380

Using the same equations as given in section 2.6 and 3.3, figure B.2 is produced. In this figure, the coil is not made resonant. This image was produced using amplifier specifications of the LT1007 and voltage noise density as given in equation B.2. As can be seen from figure

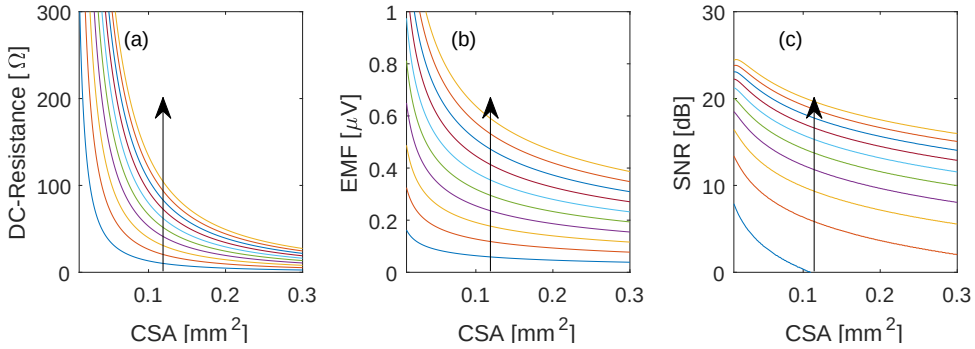

Figure B.2: Coil parameters of the unipolar coil initially used as function CSA. (a): DC-resistance in Ω. (b): EMF in V. (c): SNR in dB.
With the direction of the arrows in all graphs, the number of layers on the coil, N_l increases from one to 10.

B.2, the coil's DC-resistance grows rapidly for thin wire. EMF is several times bigger than that for the bucking-detection coil due to larger sample volume. Despite high amplifier noise for the given amplifier topology compared to the AD8428, increased EMF due to larger sample volume more than compensates this. Total thermal noise for the unipolar coil is low compared to induced EMF, resulting in high SNR. Controversially, despite EMF being higher than for the detection coils used in bucking configuration described in section 3.4 and depicted in figure 3.9, the increase in SNR cannot make up for the drastic increase in environmental noise. When the coil is made resonant and AC-resistance is taken into account, we obtain figure B.3. Evaluating figure B.3, it can be seen that induced EMF for this detection coil, using a sample volume of $750mL$ is $22.8\mu V$. Resulting SNR when the coil is made resonant equals $48dB$, without considering environmental noise. At an amplification factor of 200.000, resulting signal amplitude is $4.5V$ if bandpass filter center frequency as well as coil resonance frequency equal Larmor frequency. However, no significant EFNMR signal could be measured using the amplifier and coil. Mainly powerline harmonics filled the measurements results. Measurements performed using these electronics also revealed that it was easy to make the amplifier oscillate. To overcome this issue, total amplification factor was reduced to 109.300 by lowering the value of the $330k\Omega$ resistor to $180k\Omega$. This was

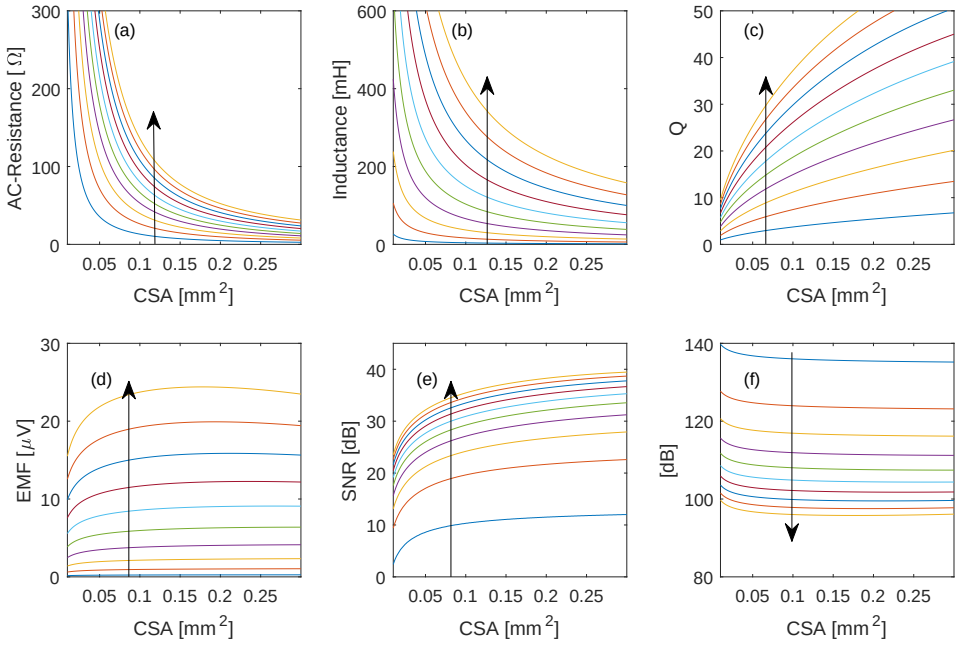

Figure B.3: Various coil parameters as function CSA.
(a): AC-resistance at $2kHz$ in Ω. (b): inductance in mH. (c): coil Quality factor, Q. (d): Induced EMF in μV. (e): SNR in dB. (f): Required amplification factor to boost EMF to $1V$.
With the direction of the arrows in all graphs, the number of layers on the coil, N_l increases from one to 10.

sufficient to suppress oscillations. Moreover, additional Power supply decoupling was added at the power inputs of every op-amp and ground potential was better defined by flooding the bottom of the circuit with solder where possible. Several issues prevented any EFNMR signal to be measured.

1. The fixed parallel tuning capacitor made it difficult to match the detection coil's resonance frequency to Larmor frequency.

2. Similarly to 1, the bandpass filter's fixed center frequency meant that every time it needed shifting, soldering was required.

3. No form of environmental noise reduction was used. The original polarizer did not feature an option to short the polarization coil during detection. To improve on this, either a heavy and expensive shielding box is required, or the coil has to be redone to allow bucking configuration.

4. EFNMR signal sampling was instable due to limited temporal resolution and stability of the Arduino Uno used.

5. Receiver dead-time of $80ms$ (see appendix D) meant that the initial part of an FID could not be measured.

To improve SNR and measure EFNMR signal above the noise floor, all of these issues had to be improved upon. First up was replacing the Arduino Uno.

B.2 Replacing the Arduino Uno for a Due.

The initial MCU used was an Arduino Uno. This is the cheapest and most widely available Arduino there is. However, it is also the simplest Arduino and various better Arduino's exist. Several limitations of the Uno made experiment control and signal digitization difficult. These limitations as well as their solutions are explained in this section.

An Arduino Uno can sample at a maximum frequency of $4.3kHz$. Near this frequency, sampling times became instable, leading to distorted measurements. Moreover, since $4.3kHz$ is below the Nyquist frequency necessary to capture EFNMR signals across the desired bandwidth (see section 3.1), meant that sampling frequency had to be increased. In addition, effects of under sampling could already be seen in the results in the form of aliasing. This is most likely due to limited filtering steepness of the single stage bandpass filter.

Sampling resolution of the ADC on the Uno is 8 bits, which means there are $2^8 = 256$ distinct values available on the input scale of $0 - 5V$. Every step therefor is $\frac{5}{256} = 0.01925V$ large. If the signal should be very small compared to the noise and thus the SNR low, the signal might be contained in the Least Significant Bit (LSB). Therefore, increasing sampling resolution is also a desired improvement when switching from the Uno to a different MCU.

Initially, a simple Matlab communication routine was used to let the Uno start a polarization cycle, wait during the polarization cycle and start sampling during FID. After sampling had completed, it sent the sample values to Matlab where the results were plotted. Serial communication between the Uno and host Personal Computer (PC), across which samples are sent, has a maximum speed of 9600 bits per second (bps). Serial communication allows only 8-bit ASCII characters to be transferred. This allows a maximum of 1200 characters and thus 400 sample points to be transferred per second. This speed is too low to allow real-time data transfer between Uno and Matlab. Therefore, the entire signal has to fit inside the memory of the Uno. Since this is only $2kB$ large, it is full after roughly 0.3 seconds when sampling at $4.3kHz$. For a single FID in a homogeneous field this is already short, and any pulse sequence is impossible.

The solution to these problems presented itself in the Arduino Due. The Due is an Arduino based on an 16-bit Atmel cortex ARM processor running at $84MHz$, whereas the Uno is an 8-bit AVR chip running at only $16MHz$. This increase in base frequency means that sampling frequency can be increased from $4.3kHz$ to $10kHz$. This prevents aliasing and makes it possible to measure EFNMR signals at any place around the globe. Moreover, this Atmel chip has an internal memory of $96kB$, almost 50 times bigger than the Uno's memory. This increases maximum measurement duration to several seconds, long enough for a full FID or pulse sequence. Another benefit is that the Due can sample with 10 *bits* which allows 4096 unique values to be obtained on the input voltage span. The input voltage span on the Due however is smaller than on the Uno, being $3.3V$ (a common digital voltage for microprocessors) instead of 5 volts. This means the LSB is $8.06 \times 10^{-4}V$, a factor 25 improvement over the Uno thus greatly improving the SNR of the measurements. Finally, the Due can communicate with the host PC at a rate of 115200 *bps*, 12 times faster than the Uno.

Maximum input voltage of the Due, $3.3V$, meant that the amplifier's output had to be centered at $1.65V$ instead of$2.5V$, which the Uno needed. This again needed soldering on the amplifier. By this time, the amplifier had been modified too many times, became unusable and was ready for replacement.

B.3 Prototyping the Signal Amplifier, version 2.

The original amplifier had been constructed on proto-board. This is a substrate with drilled holes and soldering pads on a regular grid. This type of board has high parasitic inductances and capacitances between connections, and required short wires to be used to connect parts. These properties make it difficult to produce a low noise, stable amplifier. Therefore, the original design was re-drawn in eagle CadSoft, a Computer Aided design software package which allows electronics schematics to be easily transformed into actual board layouts.

When this was done, a DIP switch was added to make it possible to mechanically switch various parallel combinations of capacitances in series with the coil to vary its resonance frequency. To make the inputs more ruggedized, double input protection diodes were inserted at the inputs of the amplifier to distribute the transient currents and improve the overall reliability of the amplifier. The general purpose small signal relays used for switching the sample coil on and off during switching of the polarization coil were replaced for Reed relays which have lower settling times and less contact bounce. Resistors used in the bandpass filter were replaced for trimmer potentiometers to allow the bandpass filter center frequency to be changed.

The finialized design was sent to a local PCB manufacturer where it was etched from a single sided copper substrate. A major advantage of a PCB compared to proto-board is a significant decrease of parasitic inductances and capacitances in the connections between components. Also a much bigger, well defined ground plane was now available from nearly any position on the PCB that was previously connected with wires. After assembly and testing, the new design proved to be much more stable than the initial version and the amplification factor could be restored to 200.000. Also, the variable coil's resonance frequency and adjustable bandpass filter center frequency proved very useful.

For the first time, a measurement signal was measured with SNR greater than $3dB$. This measurement is shown in figure B.4. To reduce environmental noise and increase SNR, a relay

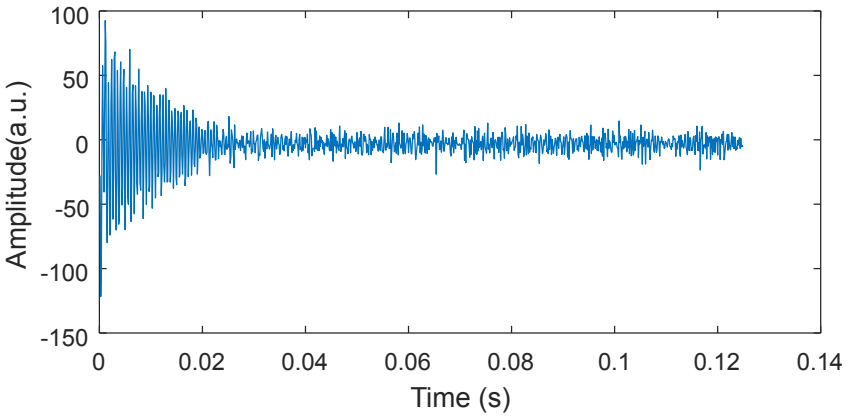

Figure B.4: First FID ever measured using version two of the amplifier.

was added to the polarization current switch, shorting the polarization coil during acquisition. This gave a reduction in noise of roughly a factor of 2, but still SNR of the measurements were not much bigger than $6dB$. Moreover, tuning the resonance frequency and bandpass filter center frequency took long to do. To summarize, the following improvements had been made compared to the original setup;

- Electrical noise, parasitic inductance and capacitance of the amplifier have been reduced drastically due to better PCB design.

- Increased flexibility in the coil's resonance frequency setting.
- Increased flexibility in bandpass filter center frequency.
- Longer measurement times at higher sample rate and higher bit-depth provide better measurement resolution due to the replacement of the Arduino Uno with the Arduino Due.
- Shorting the polarization coil during signal acquisition reduces environmental noise, increasing SNR.

At this stage, the main source of noise as well as the primary reason why measurements were not of high quality as expected, is environmental noise. Therefore, first the detection coil needed a re-design.

B.4 Switching from a Single Coil to Bucking Detection Coils.

For the measurement setup described in this research, the first bucking coil configuration was selected. In this configuration, two identical coils are aligned parallel and placed side by side. Some practical issues with the bucking coil.

Using the bucking coil requires that both coils are wired in series with a common center tap connected to ground. Signal across the two coils then has to be measured differentially since only the differential component contains the signal. Since the current iteration of the input amplifier is permanently grounded on the inverting input, this is not an option since this would differentially load the two coils removing the effectivity of the bucking coil as well as making it impossible to set the first stage' gain. To overcome this an instrumentation amplifier needs to be employed in the first stage of the input amplifier that does not load the detection coils yet still provides constant differential gain.

It was not possible to alter amplifier V2 to house a differential amplifier. Therefore, again a complete redesign of the amplifier was required. This time, the redesign was more thorough and several things were changed. Requirements the new amplifier had to satisfy are stated in section 5.1. When the amplifier was redesigned and assembled, the setup was placed outside, and a first EFNMR signal with more than $6dB$ SNR was measured. Both time domain signal, as well as the spectrum of this measurement, is displayed in figure B.5. A picture of the V3 prototype amplifier is shown in figure F.1.

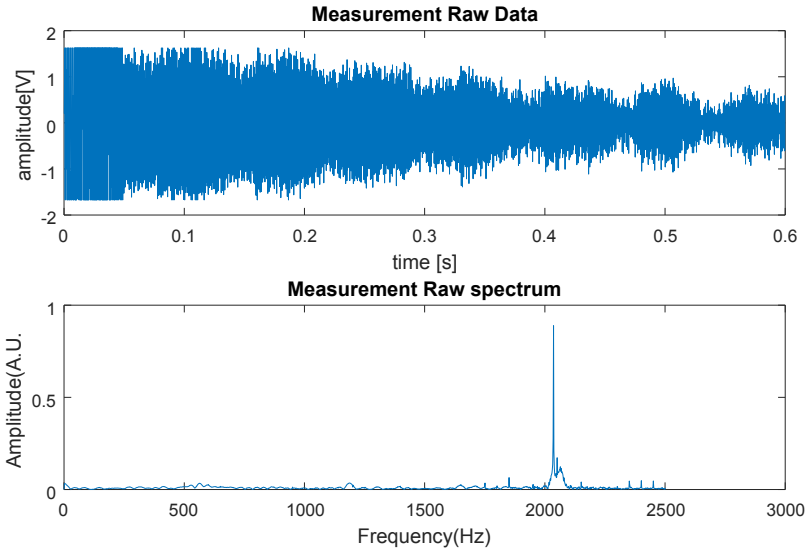

Figure B.5: Raw time-domain data and spectrum made using the bucking coils and third version of the EFNMR signal amplifier.

As can be seen from figure B.5, the FID is present with much higher SNR than in figure B.4, while both measurements only use a single measurement, no averages, and the sample volume used in figure B.5 is only$100mL$, instead of $750mL$.

After this success, the amplifier was expanded into what is currently the main board. This houses not only the signal amplifier, but also the MCU, power supplies, interfacing for external equipment as well as a pulse section to allow pulse-sequences to be performed. Design specifications of this main board are given in section 5.2. Moreover, the polarization current switch was also re-designed, and its specifications are given in section 4.2.

Appendix C: Programming and Usage

A majority of the work that went into this project was in smart programming of both the Teensy as well as the Matlab GUI and the code running it. The goal was to make operation of the setup and performing an experiment as simple as possible, while allowing room for tuning of all process parameters. Experiment control is a combination of programming and parameter selection inside the GUI with execution of preprogrammed sequences inside the Teensy. In this chapter, basic functioning and features of the programming living on the Teensy and inside the GUI are explained.

C.1 Teensy Programming

The Teensy is an MCU which relies on commands given to it to perform certain functions. In the EFNMR experiment, four individual blocks are triggered when the GUI sends the appropriate command across the Serial interface. These four blocks form an experiment when they are sequentially executed.

1. *Parameter programming :* Before a measurement is started, the Teensy is programmed with experiment parameters such as pulse timing, sample rate and measurement duration. Memory is reserved for measurement data and all IC on the mainboard such as the PGA and ADG714 are programmed by the Teensy.

2. *Verification :* When parameter programming is finished and no errors are encountered, the Teensy returns a control word to the GUI confirming correct parameter values. The GUI continues to ask the Teensy to run a second block where the teensy confirms correct parameter programming.

3. *Running the experiment :* After confirmation from the Teensy, the GUI sends a signal to the Teensy to start the experiment. The Teensy performs all timing functions such as pulse generation, relay switching and signal measurement. Once a measurement is finished, it returns a control word to the GUI to let it know it is done and data has been successfully stored.

4. *Transferring data :* Once the GUI knows the Teensy has finished, it initializes data transfer. Data processing by the GUI starts after complete data transfer. Simultaneously, a new experiment is started using the same parameters if the measurement have to be averaged. This cycle is repeated until all averages have been completed. At any time, measurements can be aborted after which unset data is cleared.

Teensy Programming - Parameter programming

Any experiment the Teensy can perform, is controlled by parameters entered by the user in the GUI. Parameters are transferred across the serial interface and received by the Teensy where they are stored. However, these parameters do not contain any timing or sequencing of events. Therefore, to transform the parameters into an experiment, the Teensy' s primary task is to calculate the exact times at which events must be triggered and to start the appropriate timers.

Matlab puts in the following parameters to the Teensy

T_{pol}	Polarization time
T_{pulse}	Pulse time
T_{Echo}	Echo time
N_{Echo}	Number of echoes
$T_{MeasWait}$	Time between end of polarization cycle and start of sampling
T_{90}	Time until pulse in adiabatic experiments
Adiabatic	Adiabatic mode
PulseAtt	Pulse Attenuation relative to $0dB$
pulseString	Pulse sequence i.e. $\{90°, 180°, ...\}$

From these parameters, the Arduino calculates the duration of each pulse. These are the times during which the pulse output is enabled and connected to the sample coils. In-between two pulses, the Arduino only has to sample. Since this occurs on the background and does require any attention, all the Arduino has to do is wait for a specified amount of time until the next pulse has to be applied. In the code below, the *pulseTimes*[] and *waitTimes*[] are calculated. Moreover, pulse trigging uses a timer with time interval *timeResolutionDef* which is set to trigger every $10\mu s$. Therefore, *nwaitTimes*[] simply contains the number of times the timer must trigger in a waiting phase. In this code, the *program*[*i*] string contains either a 1 representing a 90°pulse, or a 2 representing a 180°pulse.

```
timeResolutionDef = 1;   // corresponds to 0.01ms (10us)
timeResolutionCust = 10; // corresponds to 0.1ms (10u0s)
tEcho2  = tEcho / 2;
tPulse2 = tPulse / 2;

// get the pulse seQuence
pulseString = readInputFromMatlab();
if (pulseString.length() > 0) {
  String temp;
  for (i = 0; i < nEcho ; i++) {
    temp = pulseString.substring(i, i + 1); // get String
    program[i] = temp.toInt();              // get 1 characters
        consectually
    pulseTimes[i] = tPulse * program[i] * timeResolutionDef; // time
        per pulse
  }
  pulseString = ""; i = 0;
}
else {
  Serial.println("Error");          // Matlab Error confirmation
  return;
}

// the first element is different from the rest
waitTimes[0]  = tEcho2 - tPulse2 * program[0] * timeResolutionDef;
nwaitTimes[0]  = waitTimes[0] * timeResolutionCust;
for (i = 1; i < nEcho ; i++) {
  waitTimes[i]   = tEcho - tPulse2 * (program[i - 1] + program[i]);
  nwaitTimes[i]  =  waitTimes[i] * timeResolutionCust;
  }
i = 0;
Serial.println("ParametersSet");        // Matlab Done confirmation
```

Teensy Programming - Running the experiment

After time arrays *PulseTimes*, *waitTimes*[] and *nwaitTimes*[] are calculated and programmed into the Arduino's memory, the 10μs hardware timer is started. The Arduino now has all the information required to start the experiment. Any experiment, be it FID spin echo or CPMG is first initialized. During initialization which is shown in the code snippet below, the system state is reset, coils are made resonant, polarization is started and the ADC and DMA are started to measure the signal. Subsequently, if required in adiabatic mode, a 90°pulse is generated.

```
resetSamples();      // Clear all the samples
initsys();         // Intialize the system state
setCoilMeas(nCoil);    // Set relays to measuring mode
writeRLC(RLCSendByte);  // Make the sample coils resonant
polarize();        // Start polarization

if (tMeasWait != 0) {
  // Trigger the tMeasWait timer to start the Interrupt Service Routine
     .
  measDelayTimer.begin(measTimer_isr, tMeasWait);
  // this also does beforeTime = micros();
}
else {
  beforeTime = micros();
  measure();       // start measurement
}

if (adiabatic == 1) {     // Delay before performing 90 degree pulse
  countTimer((uint32_t)((t90 * timeResolutionCust) - (tPulse *
     timeResolutionDef) ));
  // pulser a 0 degree phase offset pulse lasting tPulse at frequency
     fLarmor
  pulseDDS(fLarmor, 0, tPulse);
  digitalWrite(polCoilShort,    HIGH);  // SHORT Polcoil during
     measurements
}
else {
  digitalWrite(polCoilShort,    HIGH);  // SHORT Polcoil during
     measurements
}
```

After initialization, the general experiment core is ran. In this code, four pulse phase are used. The explanation of each phase is given below in table C.1

Table C.1: Different stages of a generalized experiment running on the Teensy.

Phase 0	This is the initial waiting phase. Measurement coil are disabled and not made resonant. Duration of this phase is equal to *nwaitTimes*[0]. This phase could be merged with phase 2, but this is clearer.
Phase 1	Echo phase. Coils not resonant and engaged to the pulse transmitter. In this phase is where we increment i. Moreover, in this phase we can switch either to phase 1 or phase 3.
Phase 2	Memasurement phase. Sample coils are made resonant and engaged to the signal amplifier. From here only a switch to phase 1 is allowed.
Phase 3	This is the final waiting phase. Like phase 2, coils are resonant and engaged to the signal amplifier. Note; this occurs outside the *while*() loop.

```
i = 0; int Phase = 0;

// start with waiting phase, then pulse phase, until we are at the last
    pulse phase. each cycle, count timerInterrupt till nwaitTimes[i],
   PulseTimes[i]
while (i < nEcho) { // Echo loop.
  if ( timerInterrupt == true && Phase == 0) {      // initial waiting
     phase
    countTimer((uint32_t)nwaitTimes[0] );          // wait nwaitTimes(0)
    Phase = 1;                                     // switch to Phase 1
  }
  else if (timerInterrupt == true && Phase == 1) {  // Echo phase
    pulseDDS(fLarmor, 90, pulseTimes[i]);
    if (i == nEcho - 1) {
      Phase = 3; // if final pulse phase > switch to Phase = 3
    }
    else {
      Phase  = 2; // if not final waiting phase > switch to phase 2
    }
    i++;                                           // increment i;
  }
  else if (timerInterrupt == true && Phase == 2) {  // interecho phase
    countTimer((uint32_t)(nwaitTimes[i] - );       // wait
    Phase = 1;                                     // switch to pulsing
       phase
  }
  else {}   // wait until timerInterrupt becomes true
}
// Final waiting phase starts here.
while (sampleDone == false) {            // dmaADC_isr() sets
   sampleDone = true
  if (timerInterrupt == true && Phase == 3) {
    Phase = 0;
  }
  else if (timerInterrupt == false && Phase == 3) {
  }
}

//de-initialize
sampleDone = false;               // reset the Done flag to false.
afterTime = micros();
elapsedTime = afterTime - beforeTime;
initsys();                    // reset system state
Serial.println("Done");
}
```

In the code above, *countTimer*() simply counts the number of times the timer triggers and returns operation to the rest of the code when this number has been reached, providing flexible time delats between sequential actions. As can be seen, this flexible programming allows all sorts of experiments to be ran by the Teensy without it specifically knowing what the experiment is. An FID is simply a sequence with $n_{Echo} = 0$, a spin echo experiment is a sequence with $n_E = 1$ and a CPMG sequence an experiment with $n_{Echo} > 1$.

C.2 Matlab Programming; Pulse Validity

All parameters in the edit boxes and drop-down menus in the measurement tab of the GUI shown in section 6.1 can be changed by the user. However, not all values are possible. Certain parameters have limits dictated by the hardware, which the user cannot cross such as the maximum number of samples captured or the sample rate. The range of these values however is sufficiently wide to perform all types of experiments as well as allowing fine adjustments to them.

While all parameters can be set within their maximum range, not every combination of the parameters combined will return a measurement signal of an experiment, which is physically possible or even useful. Therefore, a few checks are ran each time a parameter is changed to verify its validity to the experiment selected at that moment.

When we run a pulse sequence measurement, we want to sample the signal at least until the end of the last echo. In an experiment, a sequence is controlled using the parameters shown below.

F_s	Sample rate
pts	Number of samples
T_{Echo}	Echo time
N_{Echo}	Number of echoes
$T_{MeasWait}$	Time between end of polarization cycle and start of sampling
T_{90}	Time between end of polarization cycle and 90°pulse in adiabatic experiments

A default set of values for all experiments is implemented in the Matlab code and GUI by default. The user can however enter any random combination of parameters into the GUI and run an experiment. Some combinations however will mean that not the entire signal is sampled and thus a check needs to be ran that verifies the combination of parameters. An example of a measurement is displayed in figure C.1 as function of the echo time T_{Echo} with a total of 4 echoes, and $T_{90} = T_{MeasWait}$. To sample the entire signal we require the following

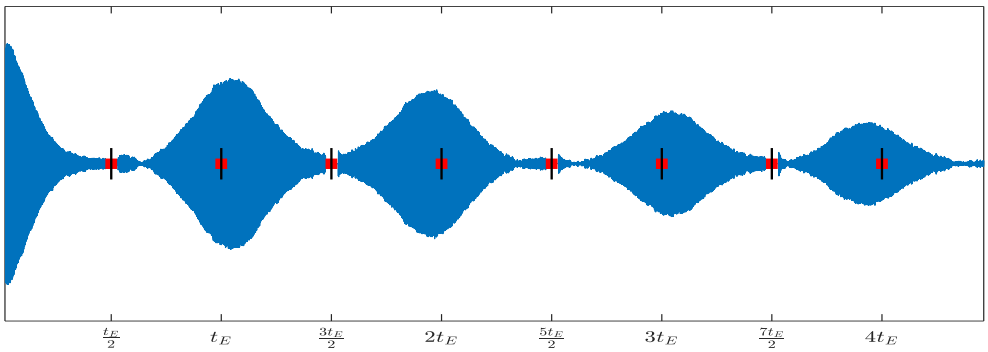

Figure C.1: Example of a sampled signal with the horizontal axis labeled as function of the echo time T_{Echo}. Note that in this CPMG sequence, the echoes are not perfectly centered on $N_{Echo} \cdot T_{Echo}$ due to an incorrect rotation angle.

inequality to be true

$$\frac{pts}{F_s} + T_{MeasWait} \geq T_{90} + T_{Echo}\left(N_{Echo} + \frac{1}{2}\right) \tag{C.1}$$

If this condition is not met, the parameter must be changed such that the condition is true.

In the case of pts, decreasing it is not allowed and the limit is a minimum

$$pts_{min} = F_s \left(T_{90} - T_{MeasWait} + T_{Echo} \left(N_{Echo} + \frac{1}{2} \right) \right) \tag{C.2}$$

In the case of F_s, increasing it is now allowed and the limit is a maximum.

$$F_{s_{max}} = \frac{pts}{T_{90} - T_{MeasWait} + T_{Echo} \left(N_{Echo} + \frac{1}{2} \right)} \tag{C.3}$$

And equally for T_{Echo} and N_{Echo}

$$T_{Echo_{max}} = \frac{1}{\left(N_{Echo} + \frac{1}{2} \right)} \left(\frac{pts}{F_s} + T_{MeasWait} - T_{90} \right) \tag{C.4}$$

$$N_{Echo_{max}} = \frac{1}{T_{Echo}} \left(\frac{pts}{F_s} + T_{MeasWait} - T_{90} \right) - \frac{1}{2} \tag{C.5}$$

If a value entered by the user was changed, a message box displays this information to the user as well as providing a reason for why it was changed. For the non-adiabatic pulse sequences, t_{90} can be removed from the expressions above.

C.3 Matlab Programming; Calculate Times

In Matlab, a similar function to that implemented on the Arduino is used for the calculation of the times at which pulses and echoes occur. The purpose of calculating these times within Matlab is however different from that on the Arduino. On the Arduino, the sole purpose of the calculations is to trigger pulse generation starting and stopping times. In Matlab, the times need to be calculated such that the individual echoes in a measurement signal can be extracted and the pulses can be masked from the total measurement.

Matlab calculates two time sequences, the *PulseTimesFirst* sequence and the *SignalTimes* sequence. The *PulseTimes* sequences contains the sample numbers of the measured signal during which a pulse is present in the signal. These pulses need to be masked from the measurement signal since they reduce SNR and distort results. The *SignalTimes* sequence contains sample numbers of begin and end times during which either an FID or echo is present in the signal which needs to be extracted from the total measurement.

PulseTimes consists of two individual sequences, those containing the first sample of a pulse and those containing the last sample number of a pulse and they are calculated using the semi-code as shown below.

```
nPulse = nEcho + adiabatic;

if adiabatic == true
  PulseTimesFirst(1)= t90 - tPulse - tMeaswait;
  PulseTimesLast(1) = t90 - tMeaswait;
end

for i = 1:1:nEcho
  j = i + adiabatic;
  pulseTime =  the duration of pulse number i;
  PulseTimesFirst(j) = (i-1/2)*tEcho - pulseTime/2 - tMeaswait + adiabatic*
      t_90;
  PulseTimesLast(j)  = (i-1/2)*tEcho + pulseTime/2 - tMeaswait + adiabatic*
      t_90;
end
```

After this code has been executed, it may be possible that entries of either *PulseTimesFirst* or *PulseTimesLast* or both are smaller than zero. This implies that $tMeaswait$ is larger than the time between $t = 0$ and the specific pulse. When this is the case, the first pulse is not recorded and the echo might also need to be removed from the measurement if it is not sampled fully since it can otherwise distort fitting results due to a lower number of points in the FFT.

The EchoTimes sequence also consists of two separate sequences, *EchoFirstTimes* and *EchoLastTimes*. They are calculated using the script below.

```
if measurementType = = "FID"
  EchoFirstTimes = PulseLastTimes(1);
  EchoLastTimes = (1000*pts)/Fs;
  Break; % We know enough
end

EchoFirstTimes(1) =  PulseLastTimes(1);
EchoLastTimes(1)  =  PulseFirstTimes(2);

for i = 1:1:(nEcho-1)
  j = i + 1;
  EchoFirstTimes(j) =  PulseLastTimes(i+adiabatic);
  EchoLastTimes(j)  =  PulseFirstTimes(i+1+adiabatic));
end

%Do the last echo separately
EchoFirstTimes(nEcho+1) =  PulseLastTimes(nEcho + adiabatic);
EchoLastTimes(nEcho+1)  =  EchoFirstTimes(nEcho + 1) +tEcho;
```

After this code has been run, like the pulse times sequences, the echo times sequences can contain values smaller than zero implying the signal (either FID or echo) was not completely recorded. If this is the case, the signal is removed.

Appendix D: Receiver Dead Time

After current in the polarization coil is removed, there is a receiver dead-time during which no measurements can be performed. Using oscilloscope readouts this effect and its origin is illustrated here. First, in figure D.1 an image is shown where the measurement coil has not yet been connected to the amplifier. For all oscilloscope images shown in this section, version 2 of the input amplifier was used. Moreover, these measurements use the unipolar coil, and not the two coils of the bucking coils used in the setup as described in chapter 5. In green,

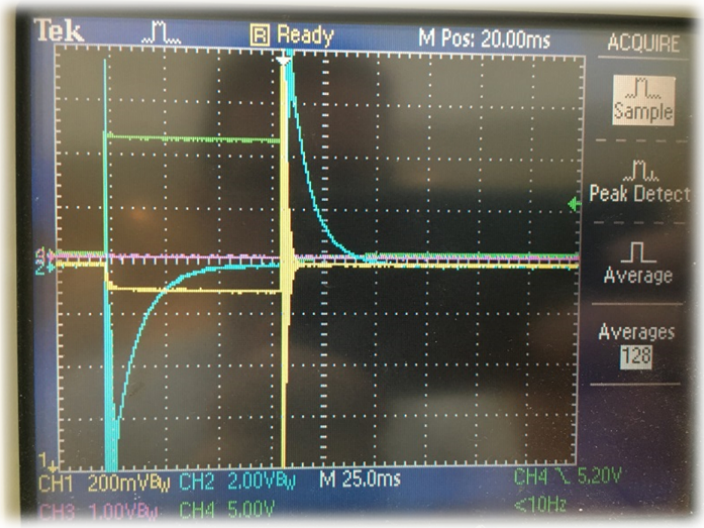

Figure D.1: Oscilloscope image showing the ring-down behavior of the sample coil. In green the voltage across the polarization coil, in blue the voltage across the measurement coil and in yellow the output of the amplifier without coil connected.

voltage across the polarization coil can be seen. It is switched on for $80ms$ before its switched off again. In blue the voltage across the measurement coil is displayed. After the current in the polarization coil is changed, either switched on or off, the measurement coil will try to maintain the magnetic field inside of it. When doing so, as described in section 2.6, a back EMF is induced. This causes a sudden increase in voltage, after which voltage across the measurement coil decays slowly. In yellow, the voltage on the output of the amplifier can be seen. It is strange that despite no input is present at the amplifier's input, output can be seen. This is probably due to a parasitic signal entering the input amplifier through ground, which is coupled to the input of the op-amps.

Next, the measurement coil is connected to the amplifier. The result of a similar sequence of polarization coil voltage is now shown in figure D.2. We now see the same traces with in pink, the voltage across the relay that enables the measurement coil to the amplifier. When it is high, the amplifier operates and amplifies the measurement signal. A distinct difference can be seen in the blue trace. The high peak that was present before is now damped to an almost perfect DC. This is due to input protection diodes parallel to the measurement coil preventing damage to the op-amps. As can be seen, it chops the blue line at roughly $0.7V$, which is the voltage drop across the diode. However, following this, the amplifier's output (yellow line), remains zero, during a period we call dead-time.

To find out why this occurs, output of the amplifier's first stage is inspected. In figure D.3 this is depicted by the pink trace.

The pink line shows clearly the input, which is a near perfect DC being amplified upto the voltage rails. The result of this is of course a DC. Since the amplifier's first and second stage,

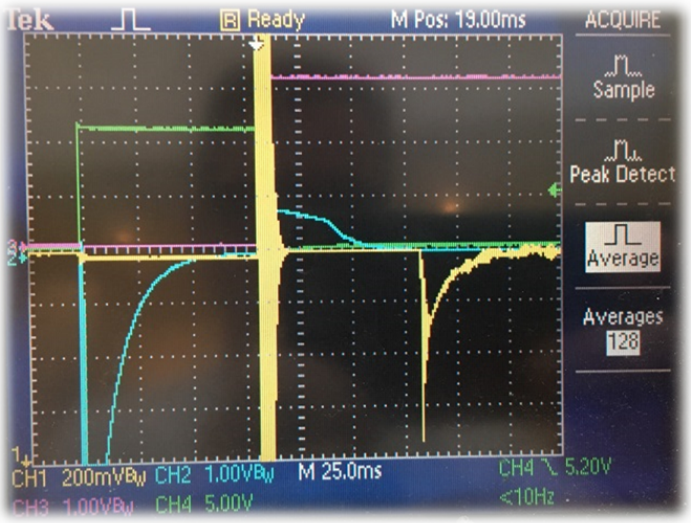

Figure D.2: Ring-down behavior of the coil when connected to the amplifier. In yellow the output of the amplifier which shows a dead time during which no signal can be measured.

the bandpass filter, are AC coupled by the feedback capacitors, no signal enters the second stage when its input is constantly high. When the first stage's output drops, the second stage starts filtering and a decay at equal rate as the pink trace but bandpass filtered, is observed. Only after this decay period, a measurement can actually be started.

Total dead time using the V2 amplifier and unipolar coil, equals roughly $80ms$ meaning that in the first 80ms after the current in the polarization coil has been shut off, no EFNMR signal can be measured. Especially when trying to measure an FID, this makes it difficult if not impossible when field inhomogeneities cause T_2^* to decrease below the dead-time.

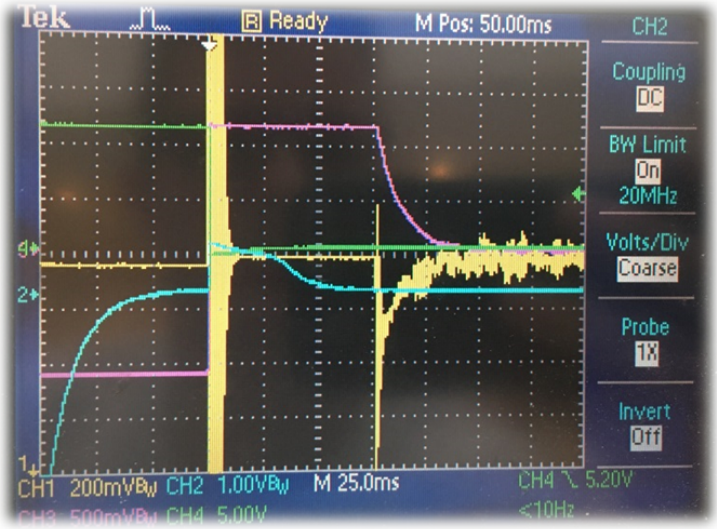

Figure D.3: Receiver dead-time measured at the output of the amplifier's first stage (pink). In yellow again the signal at the amplifier's output is shown, in blue voltage across the measurement coils and in green the voltage across the polarization coil.

Appendix E: Experimental Setup Cost

The final hardware consists of several components. The electronics; main board and polarizer circuit are assembled separately into two different housings, both required for the experimental setup to function. Cost analysis for the electronics is made for a single piece. Component prices are based on the assumption of a production quantity of 100 units and assembly cost is estimated to be roughly 25 % of the total cost of the components.

The coil system required consists of the sample coils and the polarization coils. For both coils, a quotation was obtained from a single supplier who also provided some tips to make the product production ready. Below in table E.1, a cost analysis is made of all the components and the total cost of the setup.

Table E.1: Cost price of the setup.

Main board				
	Main board PCB	€9.50		
	Electrical components	€57.00		
	Teensy 3.6	€28.00		
	Assembly Cost	€34.33		
Polarizer			+	€128.83
	Polarizer PCB and electrical components	€69.50		
	Housing and assembly	€35.08		
Sample coils			+	€104.58
	Formers	€15.00		
	Winding (incl. Copper wire)	€30.00		
	Assembly	€30.00		
Polarization coil			+	€75.00
	Former	€10.00		
	Winding (incl. Copper wire)	€20.00		
	Assembly	€30.00		
Cables			+	€60.00
	XLR Cable 5m	€7.50		
	Micro USB cable 1m	€5.00		
	Dsub 9p cable 1m	€5.00		
	BNC cable 5m	€10.00		
			+	€27.50
Power supplies				
	+12V supply	€25.00		
	-12V supply	€25.00		
			+	€50.00
	Total			+ €445.51

Appendix F: Experimental Setup Images

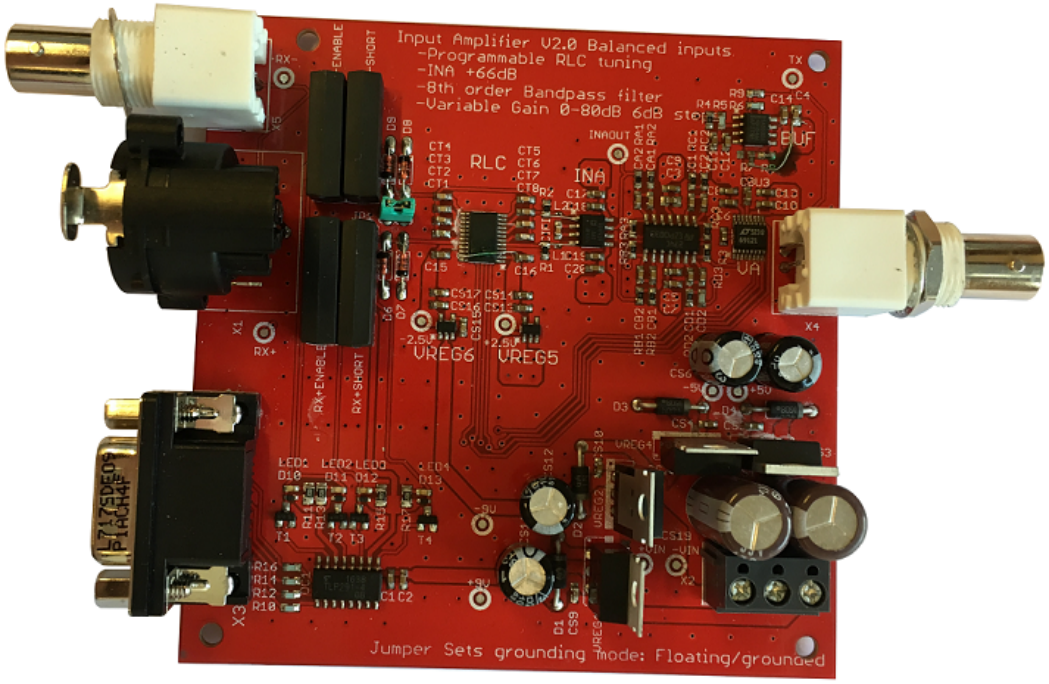

Figure F.1: Picture of the prototype Amplifier V3

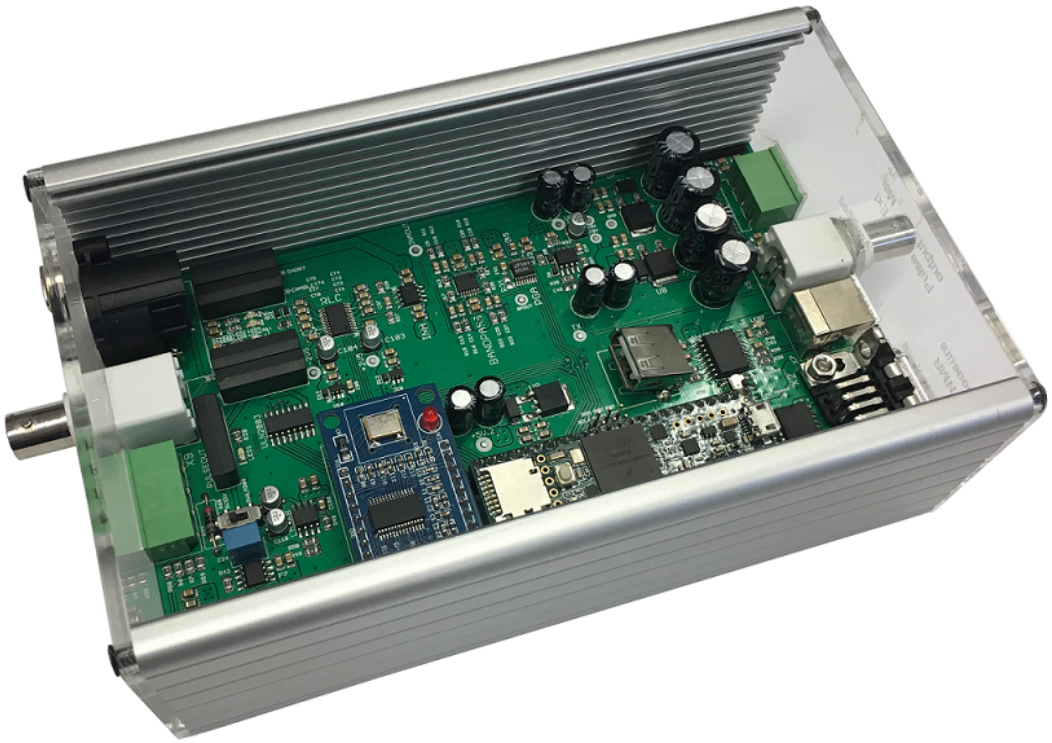

Figure F.2: Picture of the main board.

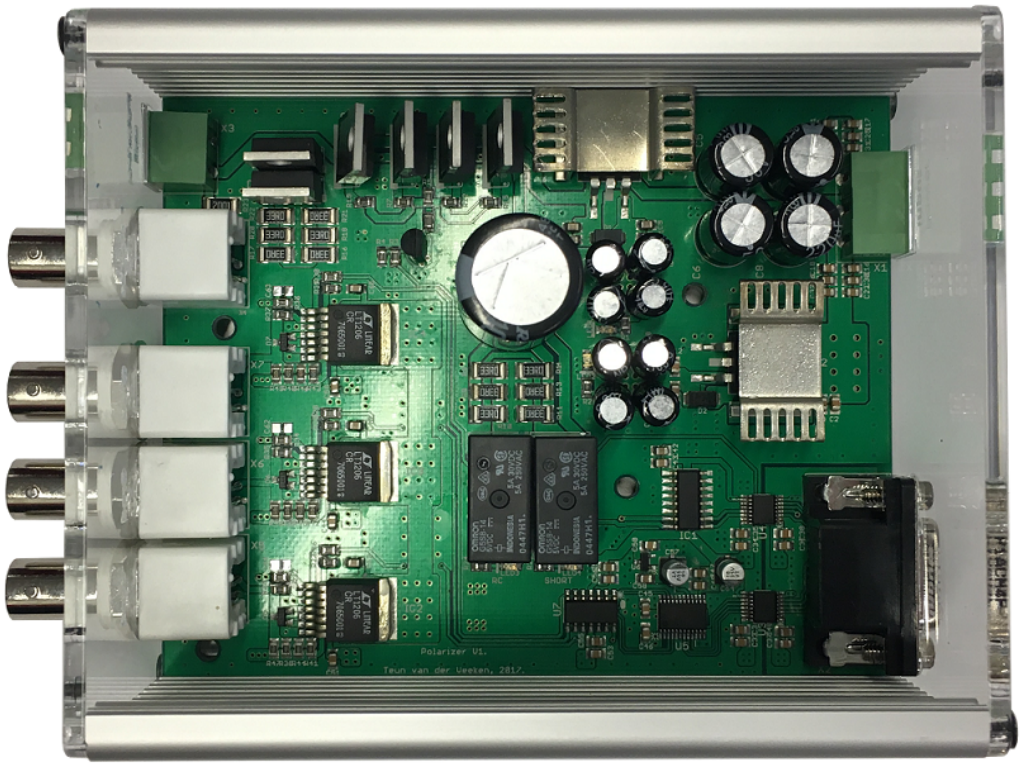

Figure F.3: Picture of the polarizer

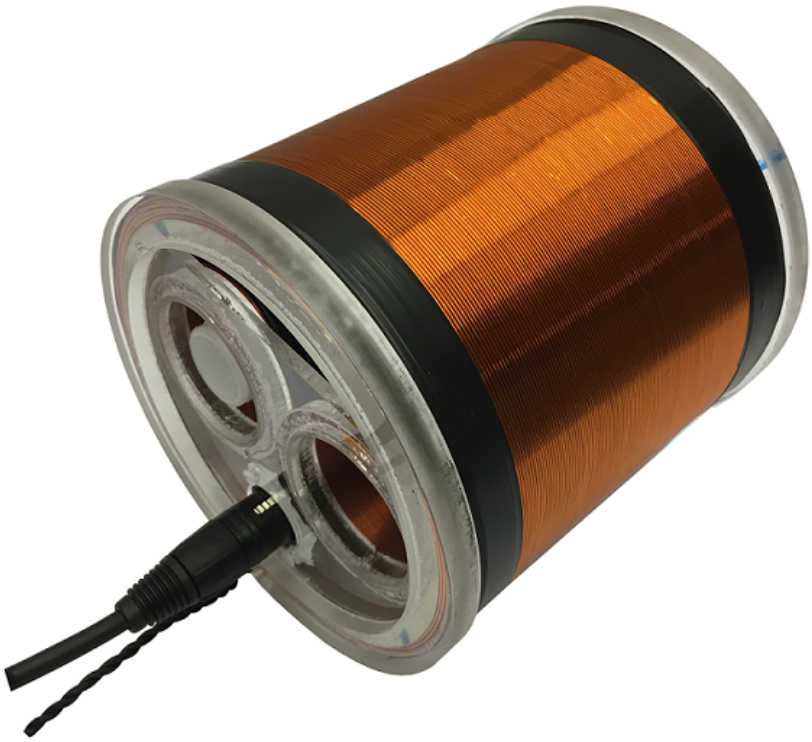

Figure F.4: Assembly of the polarization and sample coils.

Appendix G: Physical Constants

Symbol	Name	Value	First use on page
$\hbar$	Reduced Planck's constant	6.626070×10^{-24}	1
k_B	Boltzmann's constant	1.380649×10^{-23}	6
μ_0	Magnetic permeability of vacuum	1.256637×10^{-6}	6
N_A	Avogadro constant	6.022141×10^{-23}	25
q	Electron charge	1.602177×10^{-19}	27

Values obtained from [2] and rounded to six decimals.

Bibliography

[1] Magritek terranova. x, x, 14, 16, 18

[2] The nist reference on constants, units, and uncertainty, 08 2014. 102

[3] E Baudin, K Safiullin, S W Morgan, and P J Nacher. An active feedback scheme for low field nmr experiments. *Journal of Physics: Conference Series*, 294(1):012009, 2011. 49

[4] G.-J. Bene, B. Borcard, E. Hiltbrand, and P. Magnin. In situ identification of human physiological fluids by nuclear magnetism in the earth's field. *Philosophical Transactions of the Royal Society B: Biological Sciences*, 289(1037):501–502, jun 1980. 14

[5] Georges J. Béné. Nuclear magnetism of liquid systems in the earth field range. *Physics Reports*, 58(4):213–267, feb 1980. 14

[6] F. Bloch. Nuclear induction. *Physical Review*, 70(7-8):460–474, oct 1946. 8

[7] E. C. Bullard, C. S. Mason, and J. D. Mudie. Curious behaviour of a proton magnetometer. *Mathematical Proceedings of the Cambridge Philosophical Society*, 60(02):287, apr 1964. 14, 41

[8] Callaghan T. P. Eccles D. C. Nmr studies of antarctic sea ice. 18:62–64, 1996. 14

[9] Mason S. C. A proton precession magnetometer switching circuit, 1964. 41

[10] P. T. Callaghan, C. D. Eccles, and J. D. Seymour. An earth field nuclear magnetic resonance apparatus suitable for pulsed gradient spin echo measurements of self-diffusion under antarctic conditions. *Review of Scientific Instruments*, 68(11):4263–4270, nov 1997. 14

[11] P. T. Callaghan and M. Le Gros. Nuclear spins in the earth magnetic field. *American Journal of Physics*, 50(8):709–713, aug 1982. 15

[12] Paul T. Callaghan and Janez Stepišnik. Generalized analysis of motion using magnetic field gradients. In *Advances in Magnetic and Optical Resonance*, pages 325–388. Elsevier, 1996. 14

[13] H. Y. Carr and E. M. Purcell. Effects of diffusion on free precession in nuclear magnetic resonance experiments. *Physical Review*, 94(3):630–638, may 1954. 10

[14] Seevers D. A nuclear magnetic method for determining the permeability of sandstones doi. *Society of Professional Well Log Analysts Transactions*, pages 1–14, 1966. 8

[15] G C do Nascimento, R E de Souza, and M Engelsberg. A simple, ultralow magnetic field NMR imaging system. *Journal of Physics E: Scientific Instruments*, 22(9):774–779, sep 1989. 13

[16] M Espy, M Flynn, J Gomez, C Hanson, R Kraus, P Magnelind, K Maskaly, A Matlashov, S Newman, T Owens, M Peters, H Sandin, I Savukov, L Schultz, A Urbaitis, P Volegov, and V Zotev. Ultra-low-field MRI for the detection of liquid explosives. *Superconductor Science and Technology*, 23(3):034023, feb 2010. 14

[17] National Centers for Environmental Information. World magnetic model, 08. iii, x, 13, 25, 26

[18] Bruker GmbH. Nmr magnets, October 2017. iii

[19] David Griffiths David J. Griffiths. *Introduction to Electrodynamics*. Pearson Educacion, 2012. 2, 7, 19, 77

[20] E. L. Hahn. Spin echoes. *Physical Review*, 80(4):580–594, nov 1950. 9

[21] Meghan E. Halse, Andrew Coy, Robin Dykstra, Craig Eccles, Mark Hunter, Rob Ward, and Paul T. Callaghan. A practical and flexible implementation of 3d MRI in the earth magnetic field. *Journal of Magnetic Resonance*, 182(1):75–83, sep 2006. 14, 37, 71

[22] Michael T. Heath. *Scientific Computing*. McGraw-Hill Europe, 2001. 78

[23] D.I Hoult and R.E Richards. The signal-to-noise ratio of the nuclear magnetic resonance experiment. *Journal of Magnetic Resonance (1969)*, 24(1):71–85, oct 1976. iii, 7, 12

[24] Griffths David J. *Introduction to Quantum Mechanics*. Pearson, 2005. 15

[25] Koehler A.R. James. Proton precession magnetometers, revision 03., 2012. x, 30

[26] Fourier Jean-Baptiste-Joseph. *Thorie analytique de la chaleur*. F. Didot, 1822. 78

[27] Charles Kittel. *Introduction to Solid State Physics 8E*. John Wiley and Sons Ltd, 2004. 6

[28] R.L Kleinberg and M.A Horsfield. Transverse relaxation processes in porous sedimentary rock. *Journal of Magnetic Resonance (1969)*, 88(1):9–19, jun 1990. 8, 10

[29] Robert L. Kleinberg. Nuclear magnetic resonance. In *Experimental Methods in the Physical Sciences*, pages 337–385. Elsevier, 1999. 8

[30] Herbert L. Krauss. *Solid State Radio Engineering*. John Wiley & Sons Inc, 1980. 31

[31] Aleks labuda. wikipedia.org, 08 2017. generated in matlab, CC BY-SA 3.0. xii, 80

[32] Qiu Long-Qing, Liu Chao, Dong Hui, Xu Lu, Zhang Yi, Hans-Joachim Krause, Xie Xiao-Ming, and Andreas Offenhusser. Time-domain frequency correction method for averaging low-field nmr signals acquired in urban laboratory environment. *Chinese Physics Letters*, 29(10):107601, 2012. 74

[33] Veevaete Maarten. *Applications of Earth Field NMR to porous systems and polymer gels*. PhD thesis, 2008. x, 13, 14, 15

[34] Matlab. Mathworks.com, September 2017. 69

[35] H. Mehier, E. Hiltbrand, B. Borcard, P. Magnin, G. Béné, and J.O. Peyrin. Low field topical nuclear magnetism apparatus in a hospital area. *Magnetic Resonance Imaging*, 1(3):143–147, jan 1982. 14

[36] B.F. Melton and V.L. Pollak. Optimizing sudden passage in the earth's-field NMR technique. *Journal of Magnetic Resonance, Series A*, 122(1):42–49, sep 1996. 15

[37] B.F. Melton and V.L. Pollak. Condition for adiabatic passage in the earth-field NMR technique. *Journal of Magnetic Resonance*, 158(1-2):15–22, sep 2002. 15

[38] B.F. Melton, V.L. Pollak, T.W. Mayes, and Barton L. Willis. Condition for sudden passage in the earth's-field NMR technique. *Journal of Magnetic Resonance, Series A*, 117(2):164–170, dec 1995. 15

[39] O. Ripeka Mercier, M.W. Hunter, and P.T. Callaghan. Brine diffusion in first-year sea ice measured by earth's field PGSE-NMR. *Cold Regions Science and Technology*, 42(2):96–105, jul 2005. 14

[40] Carl A Michal. A low-cost spectrometer for nmr measurements in the earth magnetic field. *Measurement Science and Technology*, 21(10):105902, 2010. xiv, 82, 83

[41] Aleš Mohorič, Janez Stepišnik, Miha Kos, and Gorazd Planinšič. Self-diffusion imaging by spin echo in earth's magnetic field. *Journal of Magnetic Resonance*, 136(1):22–26, jan 1999. 14

[42] P.N. Murgatroyd. Calculation of proximity losses in multistranded conductor bunches. *IEE Proceedings A (Physical Science, Measurement and Instrumentation, Management and Education)*, 136(3):115–120, may 1989. 32

[43] Varian R. Packard M. Free nuclear induction in the earth magnetic field. *Physical Review*, 93(941), 1954. 13, 14

[44] Teodor Parella. Nmr periodic table. Technical report, Bruker Analytik GmbH., 2000. xiv, 2, 72

[45] A.S. Peshkovsky, J. Forguez, L. Cerioni, and D.J. Pusiol. RF probe recovery time reduction with a novel active ringing suppression circuit. *Journal of Magnetic Resonance*, 177(1):67–73, nov 2005. 49, 73

[46] J. G. Powles and D. Cutler. Audio-frequency nuclear-resonance echoes. *Nature*, 180(4598):1344–1345, dec 1957. 14

[47] G. L. M. SCHEEPERS. Noise-cancelling sensor for proton magnetometer. *Journal of geomagnetism and geoelectricity*, 19(2):155–155, 1967. 34

[48] C.E. Shannon. Communication in the presence of noise. *Proceedings of the IRE*, 37(1):10–21, jan 1949. 79

[49] E.C. Snelling. *Soft Ferrites: Properties and Applications*. Newnes-Butterworth, 1969. 32

[50] Y.-Q Song. Categories of coherence pathways for the CPMG sequence. *Journal of Magnetic Resonance*, 157(1):82–91, jul 2002. 10

[51] J. Stepisnik, M. Kos, G. Planinsic, and V. Erzen. Strong nonuniform magnetic field for self-diffusion measurement by NMR in the earth/s magnetic-field. *Journal of Magnetic Resonance, Series A*, 107(2):167–172, apr 1994. 14

[52] Neil Storey. *Electronics: A Systems Approach (4th Edition)*. Pearson Education Canada, 2009. 27, 28

[53] Ligon Richard Thomas. Coil design for low field nmr experiments and nmr measurements of the arm. Master's thesis, 1964. 14, 34

[54] Daniel D. Traficante. Relaxation. can t2, be longer than t1? *Concepts in Magnetic Resonance*, 3(3):171–177, jul 1991. 8, 72

[55] Morley Gavin W. Wikipedia, 08 2011. x, 9

[56] H.A. Wheeler. Inductance formulas for circular and square coils. *Proceedings of the IEEE*, 70(12):1449–1450, 1982. 20

[57] R.P. Wojda and M.K. Kazimierczuk. Winding resistance of litz-wire and multi-strand inductors. *IET Power Electronics*, 5(2):257, 2012. 32